Theoretical Investigations of Atom Tunneling in the Interstellar Medium

Von der Fakultät Chemie der Universität Stuttgart
zur Erlangung der Würde eines
Doktors der Naturwissenschaften (Dr. rer. nat.)
genehmigte Abhandlung

Vorgelegt von

Jan Meisner

aus Waiblingen

Hauptberichter	Prof. Dr. Johannes Kästner
Mitberichter	Prof. Dr. Reinhold Fink
Prüfungsvorsitzender	Prof. Dr. Joris van Slageren
Tag der Mündlichen Prüfung:	8. Dezember 2017

Institut für Theoretische Chemie
Universität Stuttgart

2018

Danksagung

Ohne die Unterstützung vieler Leute hätte meine Arbeit in dieser Form nicht zustande kommen können. Daher möchte ich hier versuchen, den meisten davon zu danken, auch wenn diese Aufzählung nicht vollständig ist.

Als allererstes möchte ich Johannes Kästner für das interessante Thema und die gute Betreuung danken, insbesondere für die großen Freiheiten, die er mir in vielerlei Hinsichten gewährt hat. Einen besonderen Dank möchte ich Reinhold Fink für das Übernehmen der Stelle des Zweitgutachters und Joris Van Slageren für den Prüfungsvorsitz aussprechen. Bei Thanja Lamberts möchte ich mich für das viele Hintergrundwissen bedanken, und dafür, mir bei astrochemischen Fragen beiseite zu stehen. Gerade in der Zeit, als ich diese Arbeit schrieb, hatte sie immer ein offenes Ohr. Des weiteren danke ich der ganzen Arbeitsgruppe für die Unterstützung, vor allem Sean McConnell, der mit mir als Bürokollege auskam und mir bei LaTeXProblemen half, sowie Andreas Löhle für das Erklären periodisch wiederkehrender Fragen zur Instantontheorie. Meinen Studenten, insbesondere Max Markmeyer, Robin Giereth, Marie-Sophie Ruß, Florian Peter und Johannes Karwounopolous, danke ich für die motivierte Arbeit an den Projekten, die zu erfolgreichen Abschlussarbeiten geführt haben. Patrick Meier möchte ich für viele hilfreiche Ratschläge beim gemeinsamen Spaghettiessen und bei einem Bier danken, Stefan Jagiella für die Unterstützung bei technischen Problemen und Guntram Rauhut für das offene Ohr für und Klären von verschiedensten Fragen.

I want to also thank my friends I met in London. First, I thank Mike Bearpark and Mike Robb for accepting me as a visitor. I'm very glad that I got the opportunity to work closely with Morgane Vacher and want also to thank João Malhado, Will Vigor, Clyde Fare, Valentina Santolini, Andrew Jenkins, and Iakov Polyak. I had a great time and felt very welcome in the group.

Der Besuch am Kapteyn Institut in Groningen hat mir geholfen, mehr über die Chemie in protoplanetaren Scheiben zu verstehen, wofür ich Inga Kamp sehr danke möchte. In diesem Zusammenhand ist dem COST-Netzwerk für finanzielle Unterstützung meines Aufenthaltes gedankt.

Dem Arbeitskreis von Herrn Gießelmann möchte ich für die Adoption danken und insbesondere Marc Harjung, mit dem ich doch die ein oder andere Kaffee- oder Mittagspause verbrachte. Nico Kreß sei für die Unterstützung bei der Aufreinigung von Cellulose gedankt und Isabella Waldner, Barbara Teutsch und Klaus Dirnberger sei vor allem, aber nicht ausschließlich, für die organisatorische Unterstützung während meiner Zeit in Stuttgart. Für abwechslungsreiche Mittagspausen möchte ich Tanja Walter, und Maren Bechthold danken. Dem Exzellenzcluster Simtech möchte ich für die Finanzierung meiner Arbeit danken und dafür, mich mit Markus Köppel, Patrick Schröder, Antje Jensch, Daniela Stöhr und vielen anderen Leuten in Verbindung zu bringen. Mit ihnen zusammen habe ich eine schöne Zeit verbracht, die ich nicht missen möchte.

Meiner Schmiedegruppe und allen, mit denen ich zusammen am Amboss stand, möchte ich hierfür danken, insbesondere Nico John, Daniel Föster und Benjamin Ziegler. Ebenso danke ich Adrian Komainda für abwechslungsreiche Treffen in Heidelberg und die gute Zeit dort. Für schöne Abende außerhalb der Uni danke ich allen, mit denen ich sie verbracht habe. Stellvertretend möchte ich Nico Winter, Marie-Sophie Ruß und Tobias Roth erwähnen.

Abschließend danke ich meinen Eltern, ohne die die Anfertigung der Arbeit und das gesamte Studium in dieser Form nicht möglich gewesen wäre.

Abstract

Chemical kinetics, *i.e.,* the investigation of chemical reactivity, reaction rates, and conditions, is a traditional field of physical chemistry. In the last decades the determination of kinetic parameters, in particular reaction rate constants, is increasingly being carried out with the aid of quantum chemical computations. These data, often complementary to experimentally determined values, provide new insights into physical chemical phenomena.

IRC Algorithm

The minimum energy path between two structures at the minimum of the electronic potential is crucial for the elucidation of chemical reaction mechanisms. In this thesis, the background and implementation of a Hessian-based predictor-corrector algorithm to optimize intrinsic reaction coordinates (IRCs) are described. For that, an established algorithm was modified in order to avoid matrix diagonalizations, which improves the scaling with respect to the system size.

Atom Tunneling

The quantum mechanical tunneling effect enables particles to pass a potential energy barrier, even when the total energy is lower than the height of the barrier. As the tunnel effect is of quantum nature and depends on the mass of the particle, it is particularly pronounced for the time-evolution of very light particles such as electrons or hydrogen atoms.

The tunnel effect emerges in chemistry because in particular the light hydrogen atoms behave as quantum objects. Atom tunneling enables chemical reactivity at cryogenic temperatures where classically there is not enough energy available to overcome a barrier. This is manifested in a curvature of the Arrhenius plot.

Eventually, the rate constant becomes even temperature-independent at very low temperatures. Because of the mass-dependence, the reaction rate decreases when the atom of interest is substituted by a heavier isotope, for example deuterium in case of hydrogen atoms. This is called kinetic isotope effect (KIE).

Dual-Level Instanton Method

A broad variety of computational methods exists to calculate reaction rate constants that include atom tunneling. Instanton theory has become an established method as it is a suitable compromise between computational efficiency and accuracy. In instanton theory, the most likely tunneling path is optimized for each temperature and the quantum fluctuations around the path are approximated harmonically. The computationally most demanding steps are the path optimization and the calculation of Hessian matrices along the tunneling path. This restricts the applicability of electronic structure methods. In this thesis, a dual-level instanton method is presented, where the optimization of the tunneling path and the evaluation of the 2^{nd} derivatives are carried out using a fast, but computationally less precise method. Subsequently, a more sophisticated electronic structure method is used to recalculate the potential energy along the tunneling path. It is shown that the rate constants obtained by the dual-level approach agree well with those obtained by exclusively using the more accurate potential. This can significantly save amounts of computational time and may even enable the use of some electronic structure methods because neither gradients nor 2^{nd} derivatives of the more accurate potential are necessary.

Water Formation in the Interstellar Medium

One of the most important molecules in the universe is water. It is assumed to be crucial for the development of life. Since water molecules have been detected in the interstellar medium, different possible routes of water formation have been discussed starting from oxygen atoms, molecular oxygen, or ozone molecules.

One key reaction starting from the successive hydrogenation of oxygen atoms is the reaction

$$\mathrm{H_2 + OH \rightarrow H + H_2O}.$$

This reaction can occur in the gas phase or on surfaces, which are often coated with water ice. In this thesis, quantum mechanical calculations are used in order to quantify the impact of atom tunneling on the reaction rate constants at temperatures below 200 K. For that, the instanton method was used on a fitted potential hypersurface of UCCSD(T)-F12/AVTZ quality. Kinetic isotope effects for all possible H/D substitution patterns were calculated. These values can be used in combination with interstellar H/D abundance ratios to make statements about the history or origin of astronomical objects.

Furthermore, the impact of a water ice surface on this reaction was studied. Reaction rate constants for two relevant surface mechanisms, the Eley–Rideal mechanism and the Langmuir–Hinshelwood mechanism, have been calculated. For that, a multiscale QM/MM framework based on rigorously benchmarked density functional theory and the TIP3P force field was used. For this particular reaction, the surrounding water molecules barely have any influence on the potential energy along the reaction coordinate. Therefore, the surface effects can be described implicitly by taking into account that rotation is restricted on a surface in the calculation of kinetic isotope effects.

Zusammenfassung

Chemische Kinetik, die Untersuchung von chemischer Reaktivität beziehungsweise den dazugehörigen Geschwidigkeitskonstanten und Reaktionsbedingungen, gehört zu den fundamentalen Gebieten der physikalischen Chemie. Das Feld ist von zentraler Bedeutung und Gegenstand aktueller Forschung. Die Bestimmung von kinetischen Parametern, vor allem Geschwindigkeitskonstanten, wird in den letzten Jahrzehnten zunehmend computergestützt durchgeführt. Die dabei gewonnenen Ergebnisse ermöglichen neue Einsichten in physikalisch-chemische Prozesse und die Optimierung bestehender chemischer Reaktionen.

IRC-Algorithmus

Um eine Aussage über chemische Reaktionsmechanismen zu treffen, ist der Pfad kleinster potentieller Energie zwischen zwei Potentialminima sowie die dazugehörige Übergangsstruktur entscheidend. Im Rahmen dieser Arbeit wurde ein hessematrixbasierter Predictor-Corrector-Algorithmus zur Optimierung von intrinsischen Reaktionskoordinaten (IRCs) implementiert. Hierbei wurde ein literaturbekannter Algorithmus modifiziert, so dass Matrixdiagonalisierungen vermieden werden, was die Skalierung des Algorithmus' verbessert.

Der Tunneleffekt

Der quantenmechanische Tunneleffekt ermöglicht es Teilchen, eine Potentialbarriere zu überwinden, obwohl sie nicht über ausreichend Energie verfügen. Da der Tunneleffekt von quantenmechanischer Natur ist und von der Masse des tunnelnden Teilchens abhängt, spielt er vor allem für die Bewegung kleinster Teilchen wie Elektronen eine bedeutende Rolle.

Der Tunneleffekt tritt jedoch auch bei chemischen Reaktionen auf, da sich Atome, insbesondere die leichten Wasserstoffatome, ebenfalls quantenmechanisch verhalten. Dies ermöglicht Reaktivität auch bei tiefsten Temperaturen, wie sie beispielsweise im interstellaren Raum vorkommen, was sich in einer Krümmung des Arrheniusplots äußert. Bei sehr tiefen Temperaturen kann die Reaktionsgeschwindigkeitskonstante sogar temperaturunabhängig sein. Durch die Massenabhängigkeit des Tunneleffekts führt eine Substitution von Wasserstoff durch Deuterium oft zu einer signifikanten Abnahme der Reaktionsgeschwindigkeit. Dies wird als kinetischer Isotopeneffekt (KIE) bezeichnet.

Duallevel-Instantonmethode

Es gibt eine große Auswahl an Methoden zur Berechnung von Reaktionsgeschwindigkeitskonstanten unter Berücksichtigung des Tunnelns von Atomen. Die in den letzten Jahren zunehmend verwendete Instantonmethode stellt einen hervorragenden Kompromiss von Genauigkeit und Rechenzeit dar. Hierbei wird für jede Temperatur der statistisch wichtigeste Tunnelpfad optimiert und die Quantenfluktuationen um diesen Pfad werden harmonisch genähert. Die rechentechnisch aufwendigen Schritte sind zum einen die Optimierung des Pfades, zum anderen die Berechnung der zweiten Ableitung des Potentials entlang des Pfades. Hierdurch ist die Auswahl der zur Verfügung stehenden Elektronenstrukturmethoden eingeschränkt. In dieser Arbeit wird eine Duallevel-Instantonmethode präsentiert, bei der die Pfadoptimierung und die Berechnung der Hessematrizen mit einer effizienten Methode durchgeführt wird. Anschließend wird mit einer genaueren, rechenzeitintensiveren Elektronenstrukturmethode die potentielle Energie entlang des Tunnelpfades neu berechnet. Es wird gezeigt, dass die mit diesem Duallevel-Ansatz erhaltenen Geschwindigkeitskonstanten gut mit den Werten übereinstimmen, die man durch ausschließliche Verwendung des genaueren Potentials erhält. Dadurch wird erheblich an Rechenzeit eingespart und die Verwendung mancher Elektronenstrukturmethoden erst ermöglicht, da für das genauere elektronische Potential keine Gradienten oder gar zweiten Ableitungen nötig sind.

Wasserbildung im Interstellaren Medium

Eines der bedeutendsten Moleküle des Universums ist Wasser, da es nach heutiger Auffassung essenziell für die Entstehung von Leben ist. Seit Wasser durch teleskopische Beobachtungen im interstellaren Medium gefunden wurde, stellt sich die Frage nach der Wasserentstehung bei den im Weltall vorherrschenden Bedingungen.

Ein möglicher Syntheseweg beinhaltet die Schlüsselreaktion

$$\mathrm{H_2 + OH \rightarrow H + H_2O}.$$

Diese Reaktion kann in der Gasphase oder auf mit Wassereis beschichteten Oberflächen ablaufen. In dieser Arbeit wird durch quantenmechanische Berechnungen gezeigt, dass der Tunneleffekt die Reaktionsgeschwindigkeit unterhalb von 200 K signifikant erhöht und damit maßgeblich zur Reaktivität beiträgt. Hierfür wurde die Instantonmethode und eine gefittete Potentialhyperfläche auf UCCSD(T)-F12a-Level verwendet. Kinetische Isotopeneffekte für alle möglichen H/D-Kombinationen wurden berechnet, mit welchen unter Berücksichtigung des HDO/H_2O-Verhältnisses Aussagen über den Aufbau von astronomischen Objekten treffen zu können.

Weiterhin wurde der Einfluss einer Wassereisoberfläche auf diese Reaktion untersucht und Reaktionsgeschwindigkeitskonstanten für zwei relevante Oberflächenprozesse, den Eley–Rideal- und den Langmuir–Hinshelwood-Reaktionsmechanismus, berechnet. Hierfür wurde ein QM/MM-Multiskalenansatz basierend auf der Kombination von einem mit hochgenauen Korrelationsmethoden sorgfältig geprüften Dichtefunktional und einem TIP3P-Kraftfeld verwendet. Im speziellen Fall dieser Reaktion haben die umgebenden Wassermoleküle einen verschwindenden Einfluss auf den Verlauf der potentiellen Energie entlang der Reaktionskoordinate. Daher konnten Oberflächeneffekte in einer neu entwickelten Methode implizit beschrieben werden, um die bei beiden Reaktionsmechanismen auftauchenden kinetischen Isotopeneffekte zu berechnen.

Peer-Reviewed Publications

Articles included in this Thesis

- **Jan Meisner**, Thanja Lamberts, and Johannes Kästner
  "Atom Tunneling in the Water Formation Reaction $H_2 + OH \rightarrow H_2O + H$ *on an Ice Surface"*, *ACS Earth Space Chem. ASAP* **1**, 399–410 (2017)

- **Jan Meisner**, Max N. Markmeyer, Matthias U. Bohner, and Johannes Kästner
  "Comparison of Classical Reaction Paths and Tunneling Paths studied with the Semiclassical Instanton Theory", *Phys. Chem. Chem. Phys.,* **19**, 23085–23094 (2017)

- **Jan Meisner** and Johannes Kästner
  "Reaction rates and kinetic isotope effects of $H_2 + OH \rightarrow H_2O + H$*"*, *J. Chem. Phys.*, **144**, 174303 (2016)

- **Jan Meisner** and Johannes Kästner
  "Atom Tunneling in Chemistry", *Angew. Chem. Int. Ed.*, **55**, 5400–5413 (2016)
  German version:
  "Der Tunneleffekt von Atomen in der Chemie", *Angew. Chem. Int. Ed.*, **128**, 5488–5502 (2016)

Articles published during the PhD Studies not included in this Thesis

- Maximilian Koy, Iris Elser, **Jan Meisner**, Wolfgang Frey, Klaus Wurst, Johannes Kästner, Michael. R. Buchmeiser, *"High Oxidation State Molybdenum N-Heterocyclic Carbene Alkylidyne Complexes: Synthesis, Mechanistic Studies and Reactivity"*, *Chem. Eur. J.*, **23**, 15484–15490 (2018)

- Daniel Brodbeck, Florian Broghammer, **Jan Meisner**, Julian Klepp, Delphine Garnier, Wolfgang Frey, Johannes Kästner, René Peters
  "An Aluminum Fluoride Complex with an Appended Ammonium Salt as an Exceptionally Active Cooperative Catalyst for the Asymmetric Carboxycyanation of Aldehydes", *Angew. Chem. Int. Ed.*, **56**, 4056–4060 (2017)
  German verison:
  "Ein Aluminium-Fluorid-Komplex mit gekoppelter Ammonium-Einheit als außergewöhnlich aktiver kooperativer Katalysator in der asymmetrischen Carboxycyanierung von Aldehyden", *Angew. Chem.*, **129**, 4115–4119 (2017)

- Maike Lenz, **Jan Meisner**, Leann Quertinmont, Stefan Lutz, Johannes Kästner and Bettina Nestl
  "Asymmetric Ketone Reduction by Imine Reductases", *ChemBioChem*, **18**, 253–256 (2017)

- Sonia Álvarez-Barcia, Marie-Sophie Russ, **Jan Meisner** and Johannes Kästner
  "Atom tunnelling in the reaction $NH_3^+ + H_2 \rightarrow NH_4^+ + H$ *and its astrochemical relevance"*, *Faraday Discuss.*, **195**, 69–80 (2016)

- **Jan Meisner**, Morgane Vacher, Michael J. Bearpark, and Michael A. Robb
  "Geometric Rotation of the Nuclear Gradient at a Conical Intersection: Extension to Complex Rotation of Diabatic States", *J. Chem. Theory Comput.*, **11**, 3115 (2015)

- Morgane Vacher, **Jan Meisner**, David Mendive-Tapia, Michael J. Bearpark, and Michael A. Robb,
  "Electronic Control of Initial Nuclear Dynamics Adjacent to a Conical Intersection", *J. Phys. Chem.*, **140**, 20 (2015)
- Suman Sen, Wolfgang Frey, **Jan Meisner**, Johannes Kästner, Micheal R. Buchmeiser
  "An Anionic Molybdenum Amidato Bisalkyl Alkylidyne Complex", *J. Organomet. Chem.*, **799**, 223 (2015)

Contents

Part I

Introduction

1 Introduction

The aim of theoretical chemistry is to rationalize or predict properties of molecules and chemical phenomena. In its early years analytical concepts based on symmetry and elementary simplifications of the electronic structure, such as the Hückel approximation or Hund's rules, were developed. After the Schrödinger equation was proposed in 1926 the Born–Oppenheimer[3] and Hartree–Fock[4] approximations followed soon in 1927 and 1930, respectively. The foundation of modern quantum chemistry was layed with the Valence-bond and molecular orbital theories.

Computational chemistry utilizes computer simulations to solve or assist in solving chemical problems. The first computer program packages have been written in the 1960's and 1970's using punch cards. Some of them are even still in use today – after conversion to modern programming languages. With the increase of computational performance and the first commercially available quantum chemistry program packages, computational chemistry reached its adulthood

The current research in both theoretical and computational chemistry deals with the development of methods with a better accuracy-to-cost ratio, *i.e.,* either reducing the necessary computational effort or improving the quality of the calculations. In this respect, one example that has been used in this thesis is the development of multiscale models the Nobel prize in 2013 was awarded to Martin Karplus, Michael Lewitt, and Arieh Warshel *for the development of multiscale models for complex*

Parts of this Chapter have been used in:
Atom Tunneling in Chemistry Jan Meisner and Johannes Kästner *Angew. Chem. Int. Ed.* **55**, 5400–5413 (2016), see reference 1, Copyright 2016 WILEY-VCH Verlag GmbH & Co. KGaA, Weinheim.
Comparison of Classical Reaction Paths and Tunneling Paths studied with the Semiclassical Instanton Theory Jan Meisner, Max N. Markmeyer, Matthias U. Bohner, and Johannes Kästner *Phys. Chem. Chem. Phys.* **19**, 23085–23094 (2017), reproduced from Ref. 2 with permission from the PCCP Owner Societies, and
Quantum Chemical Simulations for Astrochemistry Jan Meisner in *Proceedings of the 3rd bwHPC-Symposium* Sabine Richling, Martin Baumann, Vincent Heuveline (Eds.) (2017)

chemical systems, multiscale simulations were honored just recently. The application of established quantum chemical methods to relevant questions in chemistry and related fields, or prediction of other chemical phenomena are nowadays a helpful complement to experiments.

1.1 Atom Tunneling

In physical and theoretical chemistry, several nuclear quantum effects can be found. While the discretization of the energy levels leads to line spectra, the zero-point energy and the tunnel effect can influence chemical reactivity.

In classical physics, the total energy of a particle needs to be at least as high as the potential energy to overcome a potential energy barrier. In chemistry, this barrier might stem from the energy necessary to break a chemical bond. In quantum mechanics, however, quantum objects can be described by wave functions Ψ and the squared modulus $|\Psi|^2$ is the probability of finding the particle. Approaching a region where the potential energy is higher than the total energy, the amplitude of the particle wave decays exponentially. Quantum objects can penetrate and pass areas which would classically be forbidden. The wave function – and thus the probability of finding a particle – on the other side of a barrier is not zero.

While phenomenological descriptions appeared earlier, the effect was discovered and understood in 1927 by Hund.[5] Subsequently, Gamow[6] and Gurney & Condon[7] used the tunnel effect independently of each other to explain the α decay of atomic nuclei. It was understood early on that the process of tunneling can contribute to chemical reaction rates in addition or as an alternative to the thermal barrier crossing.

For a rectangular barrier, as shown in figure 1.1, the wave function can be easily analyzed. In the classically forbidden region, the amplitude of the wave function decays exponentially. The analytical solution shows that the exponential decay of the wave amplitude depends on m, the mass of the quantum object, E_A, the height of the barrier, but stronger on x, the penetration depth, *i.e.,* the width of the barrier. For classical reactions, the height of the energy barrier, E_A, is the most dominant parameter when calculating the probability of a particle to overcome the barrier. When atom tunneling plays a role, the barrier width Δx is at least equally

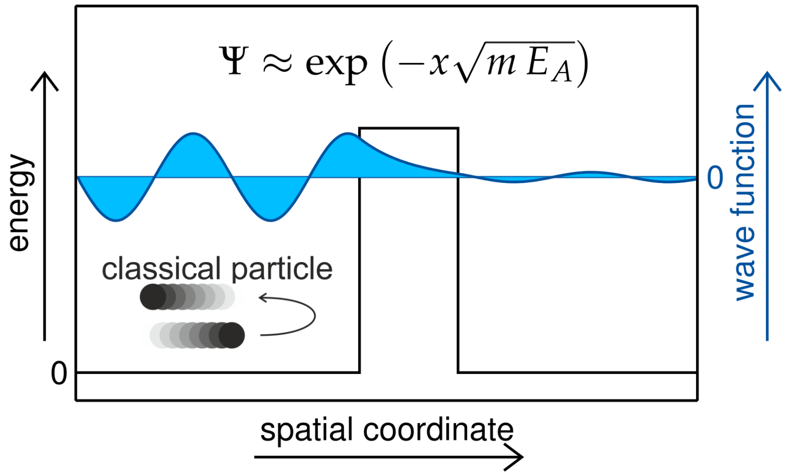

Figure 1.1 Wave function tunneling through a rectangular barrier. The equation above the barrier shows the analytical behavior of the wave function within a rectangular barrier. Adapted from Ref. 1 with permission from *Angew. Chem. Int. Ed.* **55**, 5400–5413 (2016). Copyright 2016 WILEY-VCH Verlag GmbH & Co. KGaA, Weinheim.

important: As can be intuitively seen in Fig. 1.1, a thinner barrier would lead to a smaller decay of the wave function and thus to a larger probability to find the particle on the right hand side of the barrier. This leads to the effect of corner cutting,[8] *i.e.*, the tunneling particle travels through a region of higher potential energy at the expense of a reduced barrier width. This effect is shown in Fig. 1.2 for the reaction of HCl and Cl atoms.[2]

At room temperature atom tunneling is mostly restricted to hydrogen atoms. However, in principle, many atoms of a molecule can tunnel during a chemical reaction:[1] A typical reaction path involves the movement of multiple atoms and, thus, even the effective mass can change during a chemical reaction.

This makes it nearly impossible to assign a specific mass to a certain reaction. At lower temperatures atom tunneling enables chemical reactions that would otherwise be impossible.

The mass-dependence of the tunneling rate leads to large kinetic isotope effects (KIEs), when *e.g.* substituting a ^{1}H atom by a deuterium atom (heavy hydrogen; ^{2}D). A KIE is defined as the ratio of the reaction rate constant of two

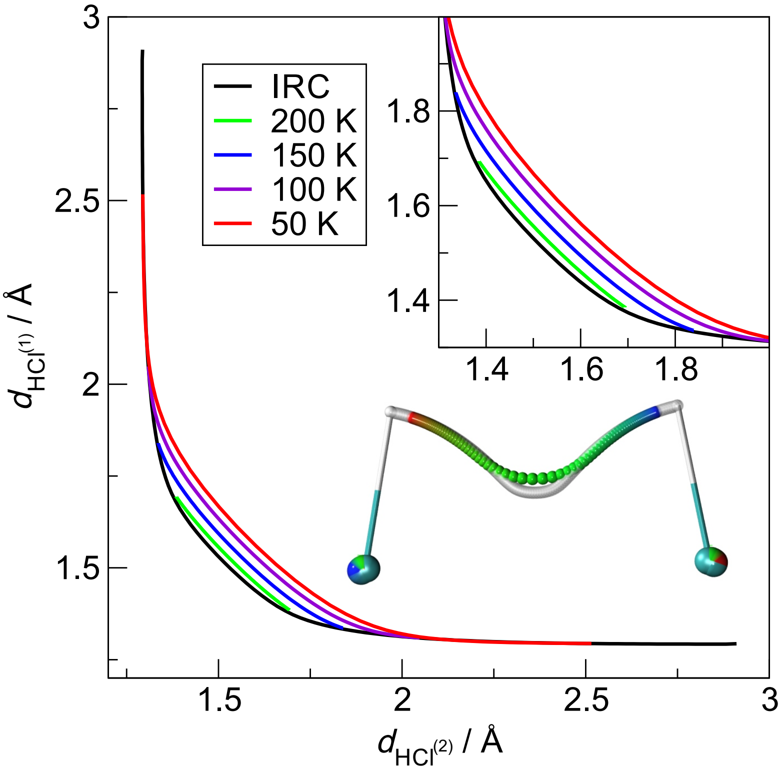

Figure 1.2 Corner cutting in the reaction of HCl + Cl: At low temperature the corner cutting leads to a significant reduction of the total path length. The picture of the molecular system shows the classical reaction path (white path) and the tunneling path (calculated with the instanton method) at 50 K (from red to green to blue). Reproduced from Ref. 2 with permission from the PCCP Owner Societies.

isotopologues (or isotopomers) of a reaction where the rate constant of the lighter isotopologue, k_H, is divided by the rate constant of the heavier one, k_D:

$$KIE = \frac{k_\mathrm{H}}{k_\mathrm{D}} \tag{1.1}$$

This even without tunneling leads to KIEs larger than one. Values < 1 are called inverse isotope effects and can occur when the vibrational adiabatic barrier is higher for the molecular system containing *e.g.* protium than for the deuterated case.[1,9] In the case of chemical reactions where one single atom – mostly a hydrogen atom – is transferred, *e.g.* in sigmatropic [1,5] H-shifts or hydrogen abstraction reactions, one can distinguish between a primary KIE and secondary KIEs: The

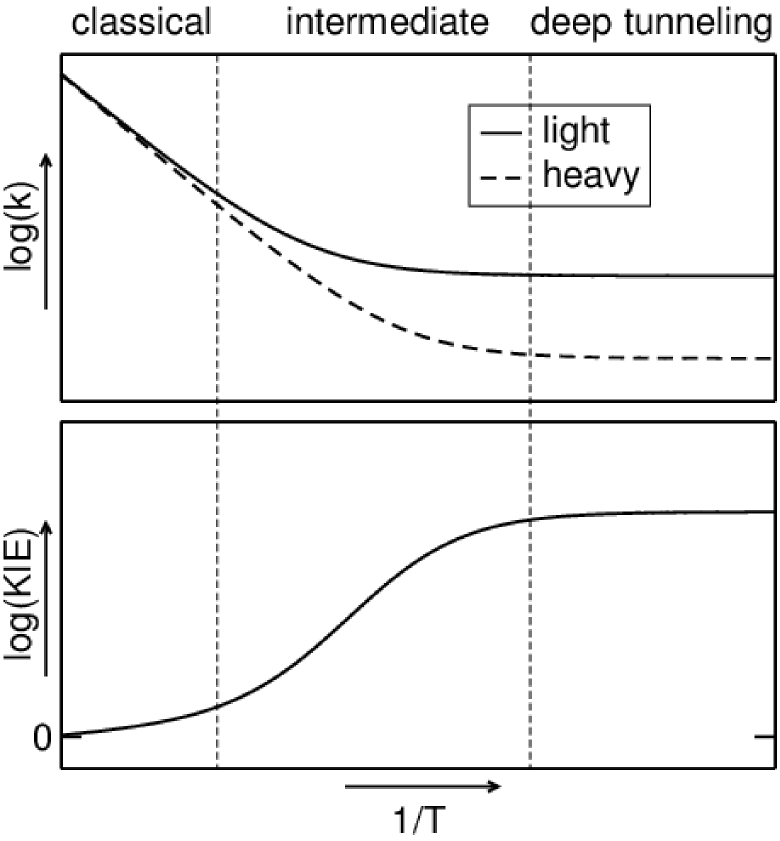

Figure 1.3 Typical temperature regimes of a chemical reaction where atom tunneling plays a role for two isotopologues. Upper part: the logarithm of the rate constant is plotted against the inverse temperature, called Arrhenius plot. Lower part: The resulting logarithmic KIE as a function of inverse temperature. Adapted from Ref. 1 with permission from *Angew. Chem. Int. Ed.* **55**, 5400–5413 (2016). Copyright 2016 WILEY-VCH Verlag GmbH & Co. KGaA, Weinheim.

primary KIE is defined as arising from the substitution of the transferred atom by the heavier isotope. Secondary KIEs are defined as arising from substitution of other atoms than the transferred one by the heavier isotope. Enhanced KIEs are the main experimental indicator that atom tunneling is happening. The KIE is a suitable probe to examine atom tunneling experimentally because it can be measured directly. A typical example of the temperature dependence of reaction rate constants and (primary) KIEs is shown in Fig. 4.1.

Since the discovery of this quantum effect, atom tunneling and its relevance for chemistry has been covered in many reviews and even textbooks. The textbook by Bell is one of the most cited references[10] and other books and review articles followed.[1,11–16] More recent review articles deal with special aspects like atom-tunneling in enzymes[17–19] or methods to calculate tunneling rates.[20–23] It has to be noted that quantum effects like tunneling also occur in areas other than chemistry. For instance, electrons tunnel much more readily than atoms due to their lower mass. This enables scanning tunneling microscopy, tunnel junctions, and tunnel diodes. These manifestations are not discussed in this thesis, as it is focused on the atom tunneling in chemistry, in particular astrochemical reactions.

1.2 Astrochemistry

Astrochemistry describes the formation, distribution, and destruction of chemical substances in space. Large-scale astrochemical models, for instance, help to explain where to expect high abundances of a particular molecule. Noteworthy features when considering reactions and reaction rates in the interstellar medium (ISM) are the low particle density, the strong radiation fields, and generally the large range of temperatures. Even so, there are nearly 200 different molecular species detected in the interstellar medium (not including atoms and isotopologues).[24]

During the different stages of star formation, the chemical reaction conditions vary. An overview of some interstellar objects occurring in the course of star formation and the chemical conditions therein is given in table 1.1. The process of star formation is quite well understood for low-mass stars.

Star formation is assumed to start with diffuse clouds. In these nebula, the density is not high enough to effectively shield the molecules from radiation and therefore, ionized species are predominant. Diffuse clouds can condense due to the gravitational force. As a result of gravitation, diffuse clouds can evolve and result into so-called dense clouds. The name is derived from the fact that they are so dense that visible light from objects behind it is absorbed thus making these objects appear dark in the sky. The temperature in dense clouds is lower because the interstellar radiation can not pervade the cloud and many molecules freeze out on the dust grain surface. Interstellar clouds can collapse, resulting in prestellar cores. Because of the higher density and the low temperature, the relevance of surface reactions increases. Eventually, a core evolves into a protostar, a young star with a high temperature that is still accreting mass from the surrounding molecules in the remaining molecular cloud. While the outer part of the protostellar envelope remains cold, the center heats up. Subsequently, a protoplanetary disk can form which is an accretion disk for the young star. It is assumed that ice and dust grains accrete to planetesimals due to electrostatic and gravitational forces, hence forming a planetary system as we know it from our own solar system.

In general, the particle density in the interstellar medium is rather low. Hydrogen is by far the most abundant atom. In diffuse clouds, temperatures are around 100 K and can be as low as 10 K in dark clouds.[25] Thus, chemical reactions can occur only if they are either barrierless, for instance, radical-radical reactions or if the barrier is tunneled through.

Many bimolecular reactions can take place via a pre-reactive minimum, a van-der-Waals complex in the entrance channel before the barrier. The encounter complex can directly decay because of excess energy released when the complex is formed or the energy dissipates to other particles if the pressure is high enough or the particles are adsorbed on a surface. In the latter case, the life time of the encounter complex increases with decreasing temperature, because thermal energy is required in order to break the complex. Therefore, more attempts to react can

Table 1.1 Types of interstellar and circumstellar molecular clouds and their particle densities and temperatures. The table is modified from Dishoeck *et al.* (reference 25).

Name	typ. density (cm^{-3})	typ. temp. (K)
Diffuse cloud	10^2	30–100
Dense dark cloud	10^3	10–20
Prestellar core	$\geq 10^5$	8–15
Protostar		
(inner)	10^7–10^9	> 100
(outer)	10^4–10^7	8–100
Protopl. disk		
(inner)	10^9–10^{15}	100–3000
(outer)	10^6–10^{10}	10–500

be made. In combination with atom tunneling, the increased lifetime can even lead to increasing rate constants at decreasing temperature. Experimental evidence for this counter intuitive effect exists in several cases, for example for the gas-phase reactions

$$H_2 + NH_3^+ \rightarrow NH_4^+ + H^{[26]}$$

and

$$CH_3OH + OH \rightarrow CH_3O + H_2O.^{[27]}$$

Besides interstellar gas-phase chemistry, reactions can also take place on the surface of dust grains.[28,29] These can consist of silicaceous or carbonaceous compounds and are usually coated by frozen water, methane, carbon monoxide, and other small molecules.[28] The coated dust grains have three main effects on chemical reactivity. Reactive species are adsorbed by the dust grains and the local concentration increases. The grains can work as an energy sink and stabilize products of exothermic reactions, which would otherwise decay directly due to the excess energy. Finally, surfaces can work as catalysts by changing the reaction mechanism or the potential energy along the reaction path.

An example set of tunneling enhanced reactions is the sequential hydrogen addition to CO, a key route for the formation of methanol in space, for which strong H/D-KIEs have been found.[30–32] For the hydrogenation of formaldehyde leading to methoxy radicals, tunneling is also important.[33,34]

In space, the amount of D atoms incorporated in molecules is enhanced with respect to a statistical distribution based on the D/H atom fraction.[35–37] For both methanol[38] and formaldehyde,[34] this can partially be explained by tunneling: the lighter protium can be abstracted by a hydrogen atom to form H_2, while deuterium remains bound to the CH_xO fragment. Subsequent barrierless recombination with another protium or deuterium atom leads to deuterium enrichment, see Fig. 1.4.

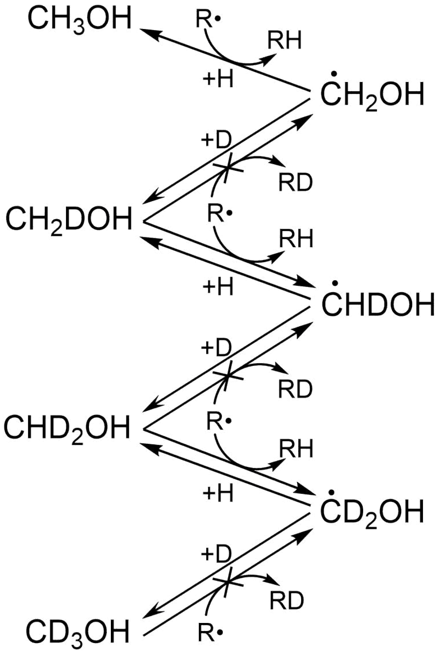

Figure 1.4 Reaction network for the deuteration of methanol. The abstraction of protium is facilitated via a tunneling mechanism, the abstraction of deuterium is much slower. Adapted from Ref. 1 with permission from *Angew. Chem. Int. Ed.* **55**, 5400–5413 (2016). Copyright 2016 WILEY-VCH Verlag GmbH & Co. KGaA, Weinheim.

1.2.1 Interstellar Water Formation

Since the discovery of interstellar water in 1969 in the orion nebula,[39] there has been an ongoing debate about water formation under the prevalent conditions in space. Meanwhile it is known that water is the main component of interstellar ices.[29,40,41] The typical abundances of molecular species in dense regions of the ISM can only be explained with considering the surface formation of water. The formation of water in the interstellar medium was studied extensively experimentally,[42–52] by means of modeling with different varieties of kinetic Monte Carlo,[53–58] and using different rate equation models.[59–61] In principle, water can be formed in the gas phase and on the surface of dust grains. For surface reactions, the grain can act as a third body absorbing the excess energy of exothermic reactions.[62] An O–H-reaction subnetwork proposed by Tielens and Hagen,[28] and updated by Cuppen *et al.*[47] and Lamberts *et al.*,[50,58](Fig. 1.5) shows that three main routes for the water formation under interstellar conditions exist: subsequent hydrogenation starting from oxygen atoms, molecular oxygen (O_2), or ozone (O_3). Different routes can dominate water formation, depending on the chemical conditions of the interstellar object of interest.

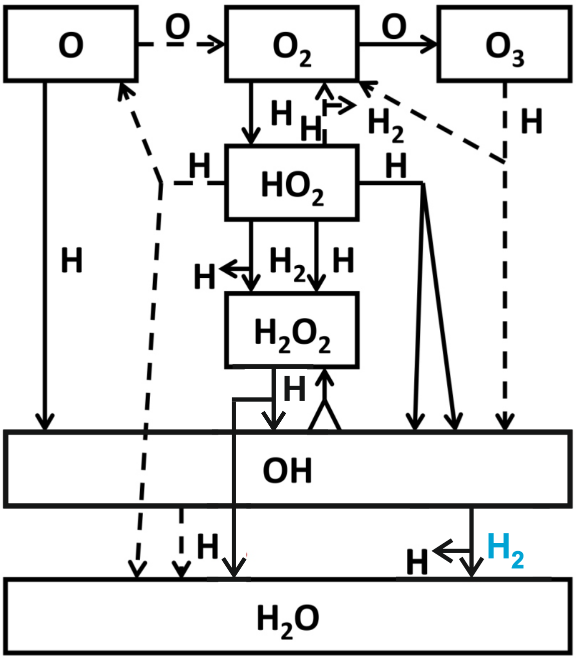

Figure 1.5 Schematic representation reaction network as obtained in reference 47.

The direct hydrogenation of O atoms by H atoms[42,63,64],

$$O + H \rightarrow OH \tag{R 1}$$

is barrierless and assumed to occur in regions where surfaces can remove the excess reaction energy and where H atoms are more abundant than H_2 molecules.[53] The reaction of O atoms with molecular hydrogen, H_2, is assumed to be of minor importance due to the endothermicity of the reaction.[50,60,65]

O_2 molecules can be hydrogenated twice to form HO_2 radicals and subsequently H_2O_2:

$$O_2 + H \rightarrow HO_2 \tag{R 2}$$

$$HO_2 + H \rightarrow H_2O_2 \tag{R 3}$$

In the gas phase, again, these reactions are not possible because of the excess heat of reaction and instead of reaction (R 3), two OH radicals are produced via the decomposition of activated H_2O_2:[66,67]

$$H_2O_2^* \rightarrow 2\,OH \tag{R 4}$$

In principle, this can also take place in the solid state. The two OH radicals can then re-form H_2O_2 or react to H_2O + O. It was shown experimentally[49] and by means of instanton theory[68] that hydrogen peroxide can react with hydrogen atoms under interstellar conditions and thanks to atom tunneling forms water and an OH radical:

$$H_2O_2 + H \rightarrow H_2O + OH \tag{R 5}$$

The third route starts from ozone, O_3, which can be hydrogenated to form O_2 molecules and OH radicals,

$$O_3 + H \rightarrow O_2 + OH. \tag{R 6}$$

This reaction was experimentally shown to take place at 10 K under interstellar ice analog conditions.[48]

Reaction (R 1), reaction (R 4), reaction (R 5), and reaction (R 6) all produced OH radicals. These can recombine with H atoms,

$$H + OH \rightarrow H_2O, \tag{R 7}$$

which is an exothermic, barrierless process, or react with molecular hydrogen,

$$H_2 + OH \rightarrow H_2O + H\;. \tag{R 8}$$

Reaction (R 8) is exothermic with a high energy barrier of 17.5 kJ mol^{-1} (experimentally determined[69,70]) to 24 kJ mol^{-1} (computationally determined[71,72]). However, it was found experimentally that reaction (R 8) takes place on water surfaces even at 10 K.[65] The relative abundances of H atoms, H_2 molecules, and O atoms in the gas phase and on surfaces determine which reaction produces OH and subsequently, whether reaction (R 7) or reaction (R 8) is predominant. Cuppen and Herbst[53] compared the reaction with other routes of water formation under various different conditions. Reactions (R 1) and (R 7), the reaction of atomic oxygen with atomic hydrogen, dominate under the conditions in diffuse and translucent cloud with rather low particle density. Reaction (R 8) seems to become important under the conditions of cold dense cores.

For further background information on interstellar water chemistry and chemical processes on interstellar amorphous solid water, the reader is referred to references 25 and 73.

1.3 Outline of the Thesis

In part II, the theory and methodology behind the calculation of reaction rate constants used in this thesis is introduced. Mostly, existing methodology has been used, but the following improvements and developments are introduced in this work:

- A modified Bulirsch–Stoer Hessian predictor-corrector algorithm to calculate intrinsic reaction coordinates (IRCs) of chemical reactions based on the algorithm by Hratchian *et al.*[74] The algorithm introduced here avoids matrix diagonalization and therefore scales with lower than third power of the system size. The implementation into the DL-FIND optimization library[75] is described in chapter 3. The algorithm is used for all IRC calculations described here and was published in reference 2.

- An implicit surface model to mimic the influence of a surface on chemical reactions is introduced in section 5.2. The implicit surface model was used in chapter 10 to calculate reaction rate constants and kinetic isotope effects. The work is published in reference 76.

- A novel dual-level ansatz of instanton theory is presented and the performance demonstrated by three different test cases in chapter 8.

Part III focuses on the chemical reaction $H_2 + OH \rightarrow H_2O + H$:

- The reaction was studied in the gas phase rigorously in chapter 9 and rate constants are provided down to 50 K. Kinetic isotope effects are calculated for all possible H/D combinations.
- In chapter 10, the reaction is investigated on an ice surface. The catalytic effect of the surface and the impact of atom tunneling are discussed. Reaction rate constants for two surface mechanisms are presented for all possible isotope patterns.

In chapter 11, the content of the thesis is discussed and concluded.

Part II

Methods

2 Basic Theory

On the microscopic scale of quantum mechanics, objects can be described by wave functions Ψ which follow the time-dependent Schrödinger equation

$$\mathrm{i}\hbar \frac{\partial}{\partial t} \Psi = \hat{H}\, \Psi. \tag{2.1}$$

Here, $\hbar$ is the so-called reduced Planck's constant and $\hat{H}$ is the Hamilton operator corresponding to the kinetic and potential energies of all particles of the system. In the time-independent form of the Schrödinger equation, Ψ^k is an eigenstate of the Hamilton operator and the corresponding eigenvalue is the total energy $\mathcal{E}_k$ of the state:

$$\Bigg[\overbrace{\hat{T}_{\text{nuc}} + \underbrace{\hat{T}_{\text{el}} + \hat{V}_{\text{nuc,nuc}} + \hat{V}_{\text{el,el}} + \hat{V}_{\text{nuc,el}}}_{\hat{H}_{\text{el}}}}^{\hat{H}} \Bigg] \Psi^k = \mathcal{E}_k \Psi^k. \tag{2.2}$$

The subscripts *el* and *nuc* stand for terms involving electrons or nuclei and $\hat{T}$ and $\hat{V}$ denote the operators of the kinetic and potential energy, respectively.

The wave function Ψ describes the physical quantum state of a system and the square of its absolute value can be interpreted as the probability density $\rho(x,t)$ of finding the quantum object at a position x at a time t.

$$\rho(x,t) = |\Psi(x,t)|^2 \tag{2.3}$$

The Born-Oppenheimer approximation is perhaps the most prominent approximation commonly made in quantum mechanics: Due to the lower mass of electrons, they possess a significantly higher kinetic energy and are therefore assumed to follow the motion of the atomic nuclei instantaneously. That means, figuratively, that the motion of the electrons and the nuclei are decoupled. The Born-Oppenheimer approximation leads to the separability of the electronic wave function ψ_{el}^{k} and the nuclear wave function χ_{nuc}^{k}:

$$\Psi^{k} = \psi_{\mathrm{el}}^{k}\ \chi_{\mathrm{nuc}}^{k} \tag{2.4}$$

The electronic wave function ψ_{el}^{k} is the solution of the *electronic Schrödinger equation*,

$$\hat{H}_{\mathrm{el}}\ \psi_{\mathrm{el}} = V_{\mathrm{el}}\ \psi_{\mathrm{el}}, \tag{2.5}$$

which depends on the nuclear coordinates only parametrically. The eigenvalues of the electronic Schrödinger equation V_{el}, for a given set of nuclear coordinates, serve as potential for the nuclear Schrödinger equation

$$\left(\hat{T}_{\mathrm{nuc}} + V_{\mathrm{el}}\right) \chi_{\mathrm{nuc}}^{k} = \mathcal{E}_{k} \chi^{k}. \tag{2.6}$$

From here on, the index *el* will be omitted for the eigenvalues of the electronic Schrödinger equation.

An analytical solution of equation (2.5) is only possible for a few very simple cases. For all other systems, further approximations have to be made, which are more or less accurate. The field of *electronic structure theory*, which is concerned with improving the approximative methods in solving equation (2.5), has a long tradition and is a vital topic. As this thesis is not concerned with electronic structure theory itself but rather with applying efficient state-of-the-art methods in order to obtain the electronic potential $V_{\mathrm{el}}(\mathbf{x})$, the reader is referred to reviews which have recently been published.[77–80]

Every one of the N nuclei has three degrees of freedom. After subtraction of three degrees of freedom for each translation and rotation of the whole molecular system, the electronic potential $V_{\mathrm{el}}(\mathbf{x})$ is a multidimensional surface of $3N-6$ dimensions, $3N-5$ dimensions for linear systems. Minima of the hypersurface correspond to stable structures and metastable intermediates. A connection between two minimum structures can be interpreted as a possible reaction pathway belonging to a chemical reaction. In the following section, the determination of accurate reaction paths by means of a modified Hessian based predictor-corrector is presented.

3 Intrinsic Reaction Coordinates

One of the most appropriate ways to determine the reaction path is to follow the *intrinsic reaction coordinate* (IRC),[81] which is the minimum-energy path in mass-weighted Cartesian coordinates. The calculation of IRCs is crucial in theoretical and computational chemistry to understand the chemical mechanism of a reaction. It has become a standard procedure during the computational investigation of chemical reactions. The geometry corresponding to the highest potential energy along the IRC is a first order saddle point of $V(\boldsymbol{x})$, called transition structure (TS). The IRC can be used to determine if the transition structure actually connects two minima. Usually, the IRC is calculated by first optimizing the transition structure and then following the steepest-descent minimum energy path in both directions. For this purpose, a broad variety of different methods has become available since its original definition in 1970.[82–87] Alternatively, the calculation can be carried out by using different formulations of the nudged elastic band method[88–90] or the string method.[91,92] Both of these methods can in principle calculate the whole IRC including the transition structure simultaneously but are computationally very demanding. For a complete overview of the literature, the reader is referred to a recent review article.[93] Here, an implementation of a modified version of Hratchian's Hessian predictor-corrector,[74] details thereof and improvements on the implementation are presented.

Parts of this Chapter have been used in:

Comparison of Classical Reaction Paths and Tunneling Paths studied with the Semiclassical Instanton Theory Jan Meisner, Max N. Markmeyer, Matthias U. Bohner, and Johannes Kästner *Phys. Chem. Chem. Phys.* **19**, 23085–23094 (2017). The content is adapted from Ref. 2 with permission from the PCCP Owner Societies.

3.1 Hessian-Predictor-Corrector Algorithm

The evaluation of the IRC begins at a saddle point of first order, the transition structure (TS), and follows the negative gradient, $-\boldsymbol{g(x)}$, of the potential energy surface (PES):

$$\frac{\mathrm{d}\boldsymbol{x}}{\mathrm{d}s} = -\frac{\boldsymbol{g(x)}}{|\boldsymbol{g(x)}|} \tag{3.1}$$

Here ds is an infinitesimally small element of the arc along the minimum-energy path in mass-weighted Cartesian coordinates.

The algorithm reported here is a modified version of the Hessian predictor-corrector scheme (HPC) by Hratchian *et al.*.[74] In summary, a comparably fast integration method (here, the explicit Euler integration) is applied as a first estimation, the so-called predictor step. After that, a more sophisticated method is used to improve this first estimation, called corrector step. The latter is determined by means of a modified Bulirsch–Stoer (mBS) integrator as described by Hratchian *et al.*,[74] which was further modified here. The original Bulirsch–Stoer algorithm is described well elsewhere,[94] but the implemented modifications will be sketched out below. Analogously to the Euler-predictor-corrector (EulerPC) presented by Hratchian *et al.*,[95] matrix diagonalization is avoided. Additionally, quadratic information is already included in the predictor step.

3.1.1 Predictor Step

The original HPC algorithm proposed by Hratchian *et al.*[74] uses the Local Quadratic Approximation (LQA),[83,84] which is a Taylor series of the PES truncated after the quadratic term:

$$\boldsymbol{g(x)} = \boldsymbol{g}_i + \mathbf{H}_i \boldsymbol{\Delta x}_i, \tag{3.2}$$

where $\boldsymbol{g}_i = \boldsymbol{g(x_i)}$ and $\mathbf{H}_i = \mathbf{H}(\boldsymbol{x_i})$ are the gradient and Hessian matrix at the geometry $\boldsymbol{x}_i$ of the i^{th} step of the IRC calculation and

$$\boldsymbol{\Delta x}_i = \boldsymbol{x} - \boldsymbol{x}_i. \tag{3.3}$$

In this case, a substitution scheme can be used to solve equation (3.1) analytically by the introduction of an independent parameter: $\frac{\mathrm{d}\boldsymbol{x}}{\mathrm{d}t} = -\boldsymbol{g}(t)$ using

$\frac{\mathrm{d}t}{\mathrm{d}s} = |\boldsymbol{g_0} + \mathbf{H_0}\boldsymbol{\Delta x}|$ as suggested by Page and McIver.[83,84] For this purpose, the Hessian matrix has to be diagonalized to obtain the eigenvalues and corresponding eigenvectors. To avoid the diagonalization, the predictor step of the HPC was changed to a plain explicit Euler integration as in the EulerPC algorithm.[95,96] This leads to a predictor step of

$$\boldsymbol{x}_{i+1}^{[P]} = \boldsymbol{x}_i - \Delta s \frac{\boldsymbol{g}(\boldsymbol{x}_i)}{|\boldsymbol{g}(\boldsymbol{x}_i)|} \tag{3.4}$$

where Δs is the step size of the IRC calculation.

In the implementation reported here, the Hessian matrix $\mathbf{H}_i$ is used to include quadratic information for the predictor step. Instead of the analytical solution as proposed in the original Hessian predictor-corrector scheme,[74] which would include the diagonalization of the Hessian matrix, the simple explicit Euler method using the energy expression

$$V(\boldsymbol{x}) = V(\boldsymbol{x}_i) + \boldsymbol{\Delta x}_i^T \boldsymbol{g}(\boldsymbol{x}_i) + \frac{1}{2}\boldsymbol{\Delta x}_i^T \mathbf{H}(\boldsymbol{x}_i)\boldsymbol{\Delta x}_i \tag{3.5}$$

is applied. This was already suggested in the work on LQA by Page and McIver[84] as an alternative for the analytic solution of equation (3.1) using the substitution described above.

The Euler integration for the predictor step is done until

$$|\boldsymbol{\Delta x}_i| \geq \Delta s. \tag{3.6}$$

The obtained geometry defines the next predictor point $\boldsymbol{x}_{i+1}^{[P]}$. The steps in the Euler integration are chosen sufficiently small:

$$\Delta_{\text{Euler}} = \frac{\Delta s}{250} \tag{3.7}$$

Once equation (3.6) is still not fulfilled after 500 Euler steps, it can be assumed that the minimum is reached. In that case, the IRC search algorithm is considered to be completed. The potential energy $V(\boldsymbol{x}_i^{[P]})$ and the gradient $\boldsymbol{g}(\boldsymbol{x}_{i+1}^{[P]})$ are computed at the predictor geometry $\boldsymbol{x}_{i+1}^{[P]}$. Hessian updates are done to get an estimation of the Hessian $\mathbf{H}(\boldsymbol{x}_{i+1}^{[P]})$.[97]

This new implementation into DL-FIND[75] avoids matrix diagonalization and therefore scales lower than $\mathcal{O}(N^3)$.

3.1.2 Corrector Step

For the corrector step, the modified Bulirsch–Stoer algorithm (mBS) is used.[98–100] The basic principle of the mBS algorithm is to use a locally fitted surface and apply an explicit integration method on it, which is repeated with a smaller step size. In the original Bulirsch–Stoer algorithm the modified midpoint method was applied.[98,99] The explicit Euler integration was shown to perform significantly better[74] and is therefore chosen in this work.

The Euler integration uses the quadratic information at the current predictor step $\boldsymbol{x}_{i+1}^{[P]}$ and at the last predictor step $\boldsymbol{x}_i^{[P]}$. For this purpose, a distance weighted interpolant surface (DWI) of the form

$$V_{\mathrm{DWI}}(\boldsymbol{x}) = \sum_{j \in \{i,i+1\}} T_j(\boldsymbol{x})\ w_j(\boldsymbol{x}) \tag{3.8}$$

is constructed. The derivation of the DWI-gradients is shown in the appendix in chapter 12. Here, $T_j(\boldsymbol{x})$ are the Taylor expansions of quadratic order around $\boldsymbol{x}_j$ and $w_j(\boldsymbol{x})$ are the weights of the respective Taylor expansion. The weights are coordinate-dependent and decay with the nth power of $\boldsymbol{\Delta x}_j$:[74]

$$w_i(\boldsymbol{x}) = \frac{|\boldsymbol{\Delta x}_{i+1}|^n}{|\boldsymbol{\Delta x}_i|^n + |\boldsymbol{\Delta x}_{i+1}|^n} \tag{3.9}$$

$$w_{i+1}(\boldsymbol{x}) = \frac{|\boldsymbol{\Delta x}_i|^n}{|\boldsymbol{\Delta x}_i|^n + |\boldsymbol{\Delta x}_{i+1}|^n}. \tag{3.10}$$

In recent literature it was argued that the energy function has to decay with a higher order than quadratic.[101] Therefore, the implementation presented here follows the proposed $n = 4$ value. The energy and gradient of the corrector step $\boldsymbol{x}_{i+1}$ is given using the DWI-energy expression in equation (3.8), because it can be assumed that the DWI describes the region around the predictor reasonably well.

Once completed, the Euler integration is repeated using a smaller step size. Both integration results are used to extrapolate the coordinates to an infinitely small step size. For this purpose the Richardson extrapolation scheme is used.[94,98] The idea of the Richardson extrapolation is outlined in the appendix in chapter 13. If the error of the extrapolated coordinates is smaller than the threshold of 10^{-6} a.u. the extrapolated integration result, *i.e.,* the thus obtained coordinates, will be used as the corrector step. If the error is still larger than the threshold, the Euler integration is repeated with an even smaller step size and the integration is done again. This is done using Neville's scheme[94,96] obtaining k different integration results (coordinates) $\mathrm{T}_{1,i}$ after performing k different integrations with different step sizes Δs_i. The Richardson extrapolation of $\mathrm{T}_{i,j}$ and $\mathrm{T}_{i,j+1}$ leads to the result $\mathrm{T}_{i+1,j}$, as can be seen in Fig. 3.1. For the first Euler integration a step size of $\frac{\Delta s}{50}$ is used. For the succeeding Euler integrations, the step size is halved in each following iteration of the mBS algorithm.

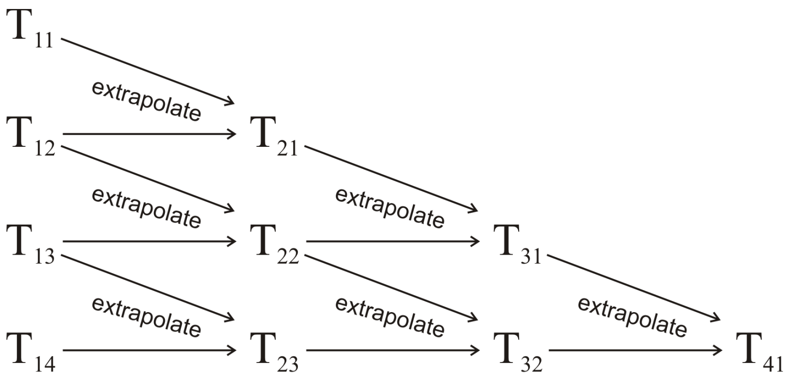

Figure 3.1 Neville's scheme used for the Richardson extrapolation. The T_{ij} represent the integration result of step size Δs_j after extrapolation to $(j-1)^{th}$ order. Reproduced from Ref. 2 with permission from the PCCP Owner Societies.

The same criterion as in the predictor step is used: if after an Euler-integration length of $2 \cdot \Delta s$ the coordinates do not differ by more than Δs it is assumed that the minimum is found. Because of oscillations around the minimum, the Bulirsch–Stoer algorithm will not be successful in this case. Thus, the Euler integration is simply repeated using a step size smaller by a factor of 10. As the mBS integrator is performed on a fitted DWI surface, this approach is feasible.

3.1.3 First Step

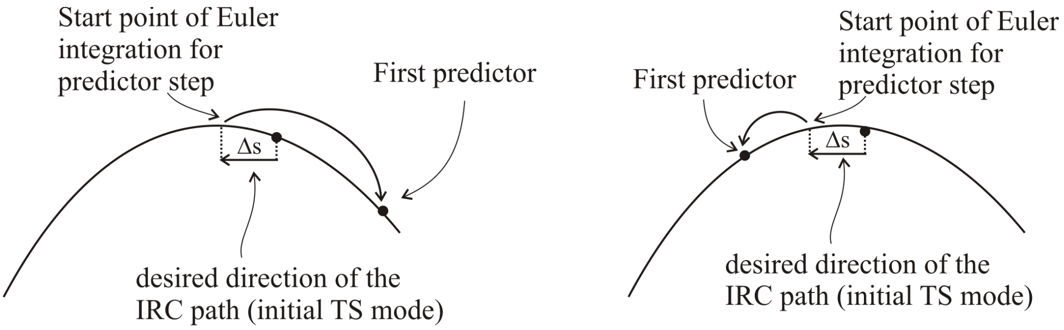

Figure 3.2 Left: consequence of an inaccurate TS location and a comparably small step size: the initial displacement Δs should lead to descent to the left, but the Euler integration in the LQA will proceed downhill to the right. Right: a more accurately optimized TS structure avoids that problem. Reproduced from Ref. 2 with permission from the PCCP Owner Societies.

At the TS geometry $\boldsymbol{x}_{\mathrm{TS}}$, the gradient vanishes and the tangent of the IRC is given by the transition mode $\boldsymbol{x}_{\mathrm{TSmode}}$. The sign of $\boldsymbol{x}_{\mathrm{TSmode}}$ decides if the IRC towards the reactants or the products is to be computed. The starting point of the IRC search algorithm is chosen as

$$\boldsymbol{x}_{\mathbf{0}} = \boldsymbol{x}_{\mathrm{TS}} + \frac{\Delta s}{2} \cdot \boldsymbol{x}_{\mathrm{TSmode}} \tag{3.11}$$

If the TS is not perfectly optimized and the error in the location of $\boldsymbol{x}_{\mathrm{TS}}$ is larger than $\Delta s/2$, the starting point $\boldsymbol{x}_{\mathbf{0}}$ ends up on the wrong side of the barrier, see Fig. 3.2.

To be able to pre-determine the IRC direction by the sign in equation (3.11) an additional numerical trick is introduced: the scalar product of the IRC step, $\boldsymbol{x}_{\mathrm{step}}$, and the transition mode at the TS geometry, $\boldsymbol{x}_{\mathrm{TSmode}}$, is calculated. If $\boldsymbol{x}^T_{\mathrm{TSmode}} \cdot \boldsymbol{x}_{\mathrm{step}}$ is negative, the angle between $\boldsymbol{x}_{\mathrm{TSmode}}$ and $\boldsymbol{x}_{\mathrm{step}}$ is larger than 90°, which implies that the direction of this step is opposite to the desired direction $\boldsymbol{x}_{\mathrm{TSmode}}$. In this case the projection of the initial transition mode vector onto the actual step is added twice:

$$\boldsymbol{x}_{\text{corrected step}} = \boldsymbol{x}_{\mathrm{step}} - 2\left(\boldsymbol{x}^T_{\mathrm{TSmode}} \cdot \boldsymbol{x}_{\mathrm{step}}\right) \boldsymbol{x}_{\mathrm{TSmode}} \tag{3.12}$$

This trick is a simple step in the direction of the transition structure and corresponds to one step of standard TS-optimizers after finding the correct eigenmode. Here, the transition vector of the approximate transition structure is used. This is a reasonable choice as the previously found transition structure can be assumed to be close to the true saddle point.

This chapter focused on the calculation of IRCs, which are necessary for the determination *which* chemical elementary reactions proceed. In the next chapter, reaction kinetics are discussed, *i.e.,* the question *how fast* these elementary reactions take place.

4 Chemical Kinetics

Chemical kinetics is the study of rates of chemical reactions. This includes the investigations of how different conditions affect the reaction rates and the time-dependence of the concentrations of the different species involved in a chemical reaction network, which is the topic of this section. Different theoretical and computational methods to obtain rate constants are outlined, leading to the explanation of semiclassical instanton theory. Finally, a new dual-level approach to instanton theory is proposed.

The reaction rate R of the chemical reaction in equation (4.1), in this case a bimolecular reaction, can be described by the ordinary differential equation (4.2).

$$\mathrm{A} + \mathrm{B} \rightarrow \mathrm{C} + \mathrm{D} \tag{4.1}$$

$$R = -\frac{\mathrm{d[A]}}{\mathrm{d}t} = -\frac{\mathrm{d[B]}}{\mathrm{d}t} = \frac{\mathrm{d[C]}}{\mathrm{d}t} = \frac{\mathrm{d[D]}}{\mathrm{d}t} = k\,[A][B] = \dots \tag{4.2}$$

Here, A and B are the reactants and C and D are the products. Brackets stand for the respective concentrations. The proportionality constant k is called the *reaction rate constant* and has the units of s^{-1} for unimolecular reactions, $\frac{l}{\mathrm{mol}}\,\mathrm{s}^{-1}$ or $\mathrm{cm}^3\ \mathrm{s}^{-1}$ for bimolecular reactions.

In most cases one is not simply faced with a single reaction, but several different reactions that form reaction cascades including side- and back reactions, pre-reactive equilibria, and other features. All of them together can form a reaction network with several thousands or tens of thousands of ordinary differential equations like equation (4.2). In astrochemistry for instance, the largest reaction networks are listed in databases and contain at least all observed species,[102,103] *i.e.,* additional hypothetical species which are assumed to exist and their deuterated counterparts are used with a large variety of possible reactions between them.

The time-dependence of the atomic and molecular concentrations lead to a large ordinary differential equation system to be solved.[25,104] This can be done by either explicit integration or by assuming the steady-state conditions to be fulfilled. In recent years, a few reviews about this topic emerged to which the reader is referred.[61,104,105]

The reaction rate constant k is independent of the concentrations of the reactants, however, it depends on the temperature T. Phenomenologically, the temperature dependence of the rate constant often follows the Arrhenius law[106,107]

$$k(T) = A \exp\left(-\frac{E_A}{RT}\right) \tag{4.3}$$

with A being an attempt frequency and R the ideal gas constant. A plot of $\ln(k)$ against $1/T$ is called an Arrhenius plot and the negative slope of an Arrhenius plot times R defines the activation energy:

$$E_A = -R\left(\frac{\partial \ln(k)}{\partial(1/T)}\right) \tag{4.4}$$

For high temperatures, the activation energy is nearly temperature independent and the Arrhenius plot is normally linear. Using statistical thermodynamics, Eyring's equation can be derived:

$$k(T) = \frac{k_\mathrm{B}T}{h} \exp\left(-\frac{\Delta G^\ddagger}{RT}\right) \tag{4.5}$$

where k_B is Boltzmann's constant, h is Planck's constant, and $\Delta G^\ddagger$ is the Gibb's free activation enthalpy, *i.e.* the difference in free enthalpy between the transition state and the reactant state, which is itself temperature dependent.

For lower temperatures, when atom tunneling plays an increasingly important role, the Arrhenius plot shows deviations from linearity and E_A changes depending on the temperature. For exothermic temperatures, the activation energy is supposed to vanish, *i.e.*

$$\lim_{T\to 0}\left(\frac{\partial \ln(k)}{\partial 1/T}\right) = 0 \tag{4.6}$$

because at $T = 0$ K all particles on the reactant's side of the barrier tunnel from the ground state, a process which is temperature independent.[108,109] In the course of this thesis, exothermic means a negative potential reaction energy $\Delta V < 0$, without any zero-point vibrational or thermal corrections. For endothermic reactions, *i.e.,* $\Delta V > 0$, the reactant's ground state has lower energy than the product state, therefore only thermally activated tunneling can occur.[108] Here, the Arrhenius plot is also not linear when tunneling is important, see Fig. 4.1. However, the activation energy tends to the endothermicity ΔV at low temperatures,

$$\lim_{T \to 0} \left(\frac{\partial \ln(k)}{\partial 1/T} \right) = \Delta V \tag{4.7}$$

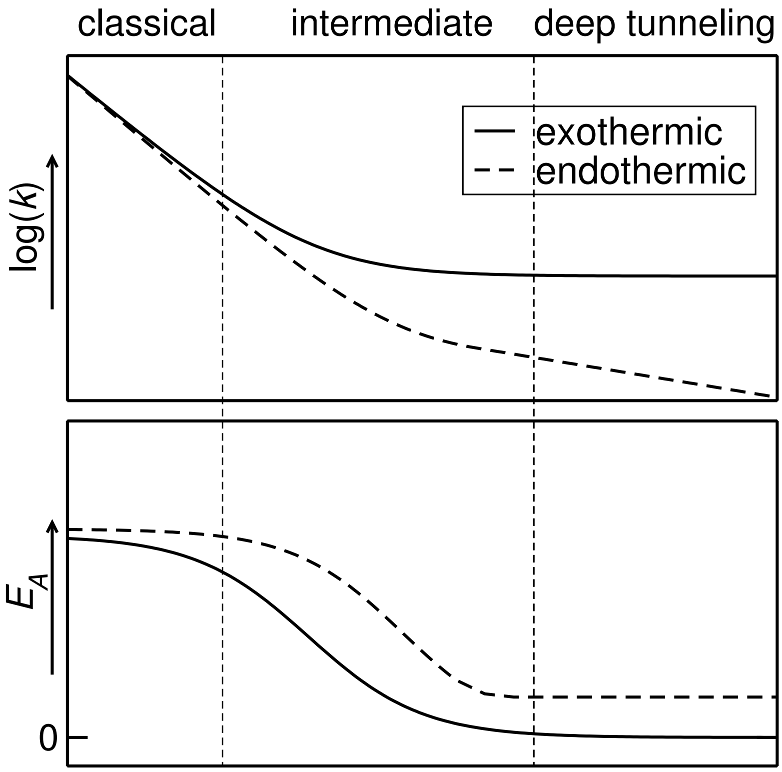

Figure 4.1 Arrhenius plot (above) and corresponding activation energy (below) for an exothermic and an endothermic reaction.

To fit $k(T)$ to a broad temperature region, other expressions are often used, where the parameters are merely fit parameters. Kooij's equation,[110]

$$k(T) = \alpha \left(\frac{T}{300\ \mathrm{K}}\right)^{\beta} \exp\left(-\frac{\gamma}{T}\right) \tag{4.8}$$

is often used in astrochemical and atmospherical models, (*e.g.* UMIST Database for Astrochemistry[102]) but does not give the correct low-temperature value for E_A.[111] Zheng *et al.* suggested a new analytical form[112]

$$k = A \left(\frac{T}{300\ \mathrm{K}}\right)^{n} \exp\left(-\frac{E}{R}\frac{(T+T_0)}{(T^2+T_0^2)}\right) \tag{4.9}$$

with four fitting parameters A, n, E, and T_0. Although Equation (4.9) leads to the correct behavior of the activation energy for $T \rightarrow 0$, the low temperature limit for the reaction rate itself goes to zero. This is not valid for exothermic reactions where the temperature independent ground state[108,109] tunneling leads to

$$\lim_{T\rightarrow 0} (k(T)) = const. \tag{4.10}$$

It was therefore suggested[113,114] to extend equation (4.9) for exothermic reactions to obtain

$$k = A \left(\frac{T+T_0}{300\ \mathrm{K}}\right)^{n} \exp\left(-\frac{E}{R}\frac{(T+T_0)}{(T^2+T_0^2)}\right) \tag{4.11}$$

and an activation energy of

$$E_A = E\frac{T^4 + 2TT^3 - T_0^2T^2}{\left(T_0^2+T^2\right)^2} + nR\frac{T^2}{T_0+T} \tag{4.12}$$

This thesis focuses on the determination of the reaction rate constants $k(T)$ and their temperature dependence. The rate constants can be obtained by means of computational chemistry using different assumptions, which will be explained in section 5. Before that, different reaction mechanisms will be outlined in the next section.

4.1 Reaction Mechanisms

4.1.1 Gas Phase Reactions

Before discussing the reaction mechanisms that involve a surface, the reactivity in the gas phase has to be considered in the example of a bimolecular reaction,

$$A_{(g)} + B_{(g)} \xrightarrow{k_{\text{gas,bi}}} \text{Products} \tag{4.13}$$

Here, the reaction rate constant $k_{\text{gas,bi}}$ is bimolecular and has the units l mol^{-1} s^{-1} or cm^3 s^{-1}. Similar expressions result for unimolecular or termolecular reactions.

The reaction rate, *i.e.,* the rate of product formation, is

$$R_{\text{gas,bi}} = k_{\text{gas,bi}}[A][B] \tag{4.14}$$

with $[A]$ and $[B]$ being the concentrations of the respective species.

In exothermic reactions, the bond formation releases kinetic energy, which is most probably concentrated in the stretching mode involving the newly formed bond. It might also be possible that the newly formed products are in an electronically excited state. In this case, the energy is partially stored as excitation energy and partially as vibrational energy. This energy can be transformed into molecular vibrations or, if the reaction results in two particles, in kinetic energy. Without any energy redistribution, the excess energy will lead to destruction of the products and the reactants will be re-formed. There are different possibilities of how to stabilize the products of exothermic reactions:

- The newly formed species is big and has enough internal degrees of freedom which are anharmonically coupled to the modes where the excess energy is located. Then, the product(s) can thermalize internally and dissociation is less likely. The molecules detected in the interstellar medium and studied hereinafter are typically rather small and are comprised of just a few atoms, which makes this mechanism rather unfavorable.

- The product can lose the excess energy by colliding with another particle M in a three-body reaction,[115]

  $$A + B + M \rightarrow \text{Products} + M^*, \tag{R 9}$$

  where the collision partner M^* is vibrationally excited after the reaction. This mechanism is only efficient when the total particle density is high enough as the reaction rate is of third order. For this purpose, the collision partner M can be any particle, as the excess energy is transformed into translational (kinetic) energy.

- On a surface, the excess energy can dissipate to the surface atoms.[116] This mechanism is similar to the three-body interaction. The released energy is transformed into substrate phonons.[117]

- When the product lives long enough, there is also the chance of a radiative emission via a photon.[118]

For gas-phase reactions it has to be noted that, in general, A and B form a distinct pre-reactive complex (PRC) on a minimum of the potential energy hypersurface. In the PRC, A and B are in close vicinity to each other, but have not yet overcome the barrier to form any products, see Fig. 4.2.

The lower energy of the PRC compared to the separated reactants can stem from hydrogen bonds, dipole-dipole interactions, Van-der-Waals forces, or other attractive interactions. In the context of this thesis the formation of the PRC is always assumed to be barrierless.

$$A_{(g)} + B_{(g)} \rightleftharpoons \text{PRC} \xrightarrow{k_{\text{gas,uni}}} \text{Products} \tag{R 10}$$

Here, the last reaction step stands for the conversion of the PRC to the products and is formally unimolecular:

$$R_{\text{gas,uni}} = k_{\text{gas,uni}}[\text{PRC}] \tag{4.15}$$

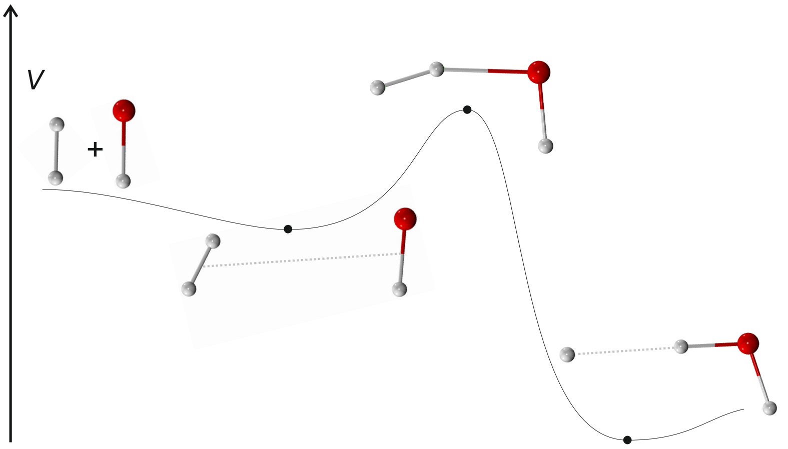

Figure 4.2 Schematic potential energy along the reaction coordinate of an exothermic reaction. The separated reactants form a slightly stabilized pre-reactive complex (PRC) and the transition structure is the highest point in potential energy. In the case of an exothermic reaction, the product complex is lower in energy than the reactants. Here, the hydrogen atom transfer in the reaction of H_2 and OH radicals is used as an example.[72]

In equilibrium, the concentration of the PRC can be expressed by the difference in free enthalpy, $\Delta G = G(\mathrm{PRC}) - G(\mathrm{A}) - G(\mathrm{B})$,

$$\frac{[\mathrm{PRC}]}{[\mathrm{A}][\mathrm{B}]} \propto K_{\mathrm{eq}} = \exp\left(-\frac{\Delta G}{RT}\right) \tag{4.16}$$

with K_{eq} being the equilibrium constant, K_{eq} has to be unitless. Therefore, $\frac{[\mathrm{PRC}]}{[\mathrm{A}][\mathrm{B}]}$ is multiplied by the standard concentration with the numerical value of 1. The reaction rate reads

$$R_{\mathrm{gas,uni}} = k_{\mathrm{gas,uni}}[A][B] \exp\left(-\frac{\Delta G}{RT}\right). \tag{4.17}$$

Depending on the energy relative to the separated products, the PRC can be interpreted as an intermediate. The lifespan of the PRC is dominated by different factors, as it may also decay back to the separated reactants A and B due to the excess interaction energy. The stabilization mechanisms rely on energy dissipation.

There are different reaction mechanisms possible in surface chemistry.[119] Two of them, the Eley–Rideal mechanism and the Langmuir–Hinshelwood mechanism, will be introduced in this section.

4.1.2 The Eley–Rideal Mechanism

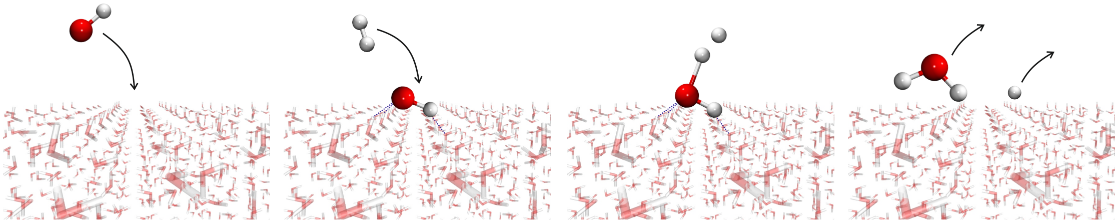

Figure 4.3 Eley–Rideal reaction mechanism. One particle is first adsorbed on a surface. A second one impinges from the gas phase and the products are directly formed.

The Eley–Rideal (ER) mechanism was proposed by D.D. Eley and E. Rideal in 1938[120,121], see Fig. 4.3. It is supposed that one particle A is adsorbed on the surface and thermalizes:

$$A_{(g)} \rightarrow A_{(ads)} \tag{R 11}$$

After that, another molecule comes directly from the gas phase and reacts with the adsorbed molecules forming the products:

$$A_{(ads)} + B_{(g)} \xrightarrow{k_{\mathrm{ER}}} \text{Products} \tag{R 12}$$

The products may either stay adsorbed on the surface or desorb if enough kinetic energy is available. In this thesis, the processes after the formation of the chemical bonds, such as desorption or heat dissipation, are not considered because they do not alter the potential energy barrier and thus, do not influence the reaction rate. It is assumed that the adsorption is barrierless or at least very fast and that the step of chemical bond breaking is rate-determining. Reaction (R 12) can formally be seen as a bimolecular reaction between the molecules B in the gas phase and the molecule adsorbed on the surface.

4.1.3 The Langmuir–Hinshelwood Mechanism

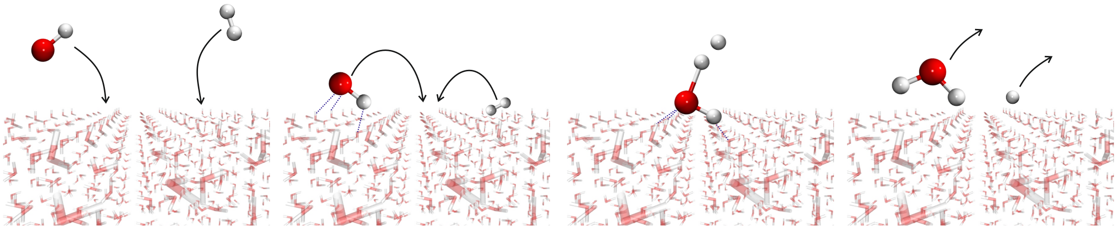

Figure 4.4 Langmuir–Hinshelwood reaction mechanism. Both particles are adsorbed on a surface. They remain adsorbed, meet by diffusion and react to the products.

The Langmuir–Hinshelwood mechanism (LH, see Fig. 4.4) was suggested by I. Langmuir in 1921[122] and further developed by C. Hinshelwood in 1926.[123] The first step of the LH mechanism is the adsorption of both species A and B separately:

$$A_{(g)} \rightarrow A_{(ads)} \tag{R 13}$$

$$B_{(g)} \rightarrow B_{(ads)} \tag{R 14}$$

The two reactant molecules thermalize, can diffuse on the surface until they meet and then form a pre-reactive complex (PRC). As described above, the PRC can decay to form the reaction products:

$$A_{(ads)} + B_{(ads)} \rightarrow [A \cdots B]_{(ads)} \xrightarrow{k_{\text{react}}} \text{Products} \tag{R 15}$$

The reaction rate of the Langmuir–Hinshelwood mechanism, R_{LH}, can thus be described as the product of the rate with which they meet each other and the probability that they react *when* they have met:

$$R_{\text{LH}} = R_{\text{diff}} \cdot P_{\text{react}} \tag{4.18}$$

The former is directly related to the diffusion constants of both species on the surface, $k_{\text{diff,A}}$ and the concentration of binding sites, [sites]:

$$R_{\text{diff}} = (k_{\text{diff},A} + k_{\text{diff},B}) \frac{[A][B]}{[\text{sites}]} \tag{4.19}$$

When the two particles meet, there is a wide range of different possible physical processes which can happen. The molecules can react to the products, diffuse without further interaction, or even desorb from the surface. The reaction probability, P_{react}, describes this competition of processes and is the ratio of the actual reaction rate constant and all possible processes of the particles:

$$P_{\text{react}} = \frac{k_{\text{react}}}{\sum\limits_i k_i} \approx \frac{k_{\text{react}}}{k_{\text{react}} + k_{\text{diff},A} + k_{\text{diff},B} + k_{\text{des},A} + k_{\text{des},B}} \tag{4.20}$$

Here, the diffusion and desorption constants, as well as the reaction rate constants, k_{react}, are formally unimolecular. The values of $k_{\text{diff},I}$ and $k_{\text{des},I}$, depend on the interaction of the particle I and the surface. When neglecting the process of desorption, which is typically much slower than diffusion,[119] the LH-reaction rate is

$$R_{\text{LH}} = (k_{\text{diff},A} + k_{\text{diff},B}) \frac{k_{\text{react}}}{k_{\text{react}} + k_{\text{diff},A} + k_{\text{diff},B}} \frac{[A][B]}{[\text{sites}]}. \tag{4.21}$$

The reaction rate constants k_{ER} and k_{react} can be provided by *ab initio* calculations. In chapter 5 different methods to calculate the actual values of the reaction rate constants are discussed.

5 Calculating Reaction Rate Constants

This section focuses on the different rate theories used in this thesis. Starting from one of the most basic rate theories, transition state theory, the calculation of thermal reaction rate constants is explained. Different tunneling correction schemes are introduced, ending with the description of instanton theory, the presentation of a new dual-level ansatz of instanton theory, and the performance of this approach.

In this thesis, canonical rate theories are used throughout. In principle, the Rice–Ramsperger–Kassel–Marcus theory (RRKM theory)[124–126] or other approaches can be used to calculate cumulative reaction probabilities $P(E)$ and obtain the corresponding canonical rate constants by the Laplace transformation[127–129]

$$k(T) = \frac{1}{2\pi\hbar Q_{\mathrm{RS}}} \int_{-\infty}^{\infty} P(E) e^{-\beta E} \mathrm{d}E, \tag{5.1}$$

where $\beta = \frac{1}{k_{\mathrm{B}}T}$ is the reciprocal temperature and Q_{RS} is the partition function of the reactant state, see section 5.1.1. A microcanonical approach can be used, in principle, to calculate reaction rate constants at very low temperatures. This is helpful when the PRC is assumed to be out of thermal equilibrium, *e.g.* because of the low-pressure environment in the interstellar medium.

5.1 Transition State Theory

One of the simplest techniques to calculate reaction rates is transition state theory (TST). Transition state theory, formerly also referred to as activated-complex theory, was mainly developed by Eyring, Evans, and Polanyi.[130,131] In TST, the configuration space is divided into a reactant region and a product region separated by a closed dividing (hyper-)surface, the transition state (TS). An example for a projection into a two-dimensional configuration space can be seen in Fig. 5.1. There, the TS is a one dimensional hypersurface, *i.e.,* a one dimensional line dividing the two-dimensional configuration space in the reactants and the products. Transition state theory is based on various different approximations and assumptions:

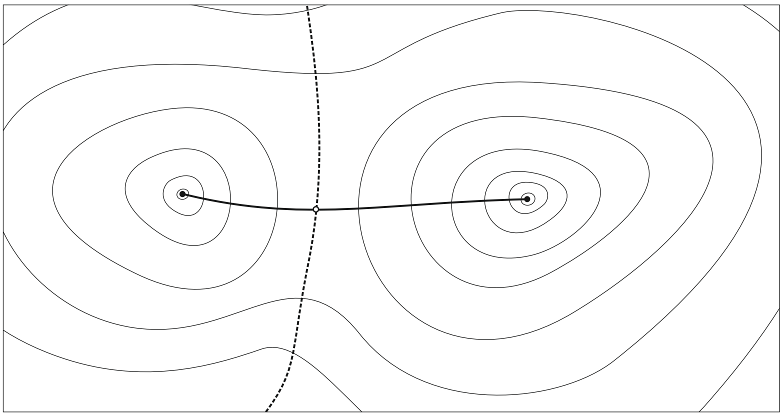

Figure 5.1 Projection of a potential hyper surface. Thin solid lines show isoenergetic configurations. Solid points stand for (meta) stable structures and the thick solid line connecting them is the minimum-energy path. The dashed line represents the dividing surface, the transition state. The hollow point on the MEP is the 1^{st} order saddle point.

- The Born-Oppenheimer approximation and the separability of the electronic motion from the nuclear motion leads to a potential energy hyper surface. The nuclei can propagate from one minimum structure to another, which represents a chemical reaction, see section 4. It follows that the reaction has to be electronically adiabatic in the vicinity of the transition state, which is the dynamical bottleneck, although versions of *non-adiabatic transition state theory* exist.[132–134]

- It is assumed that the reactant molecules are thermally equilibrated. The energies of the reactant molecules can be described by a Boltzmann distribution. It is also assumed that the transition state is in equilibrium with the reactant state.

- If a molecule crosses the TS region, it will react to the products and not recross the TS again.

- In classical TST the motion along the reaction coordinate is furthermore treated classically and is assumed to be separated from the motions perpendicular to it.

As the nuclear motion is treated classically in most TST formulations, neither atom tunneling nor non-classical reflections are included. The quantization of *e.g.* the vibrational and rotational energy levels is taken into account by means of the corresponding quantum mechanical partition functions. The TST rate expression can be derived by means of thermodynamical equilibrium between the transition state and the reactants:[130,131]

$$k_{\mathrm{TST}} = \frac{k_{\mathrm{B}}T}{h}\frac{Q_{\mathrm{TS}}}{Q_{\mathrm{RS}}} \tag{5.2}$$

where Q denotes the canonical partition function.

Different formulations of TST exist, which are based on further assumptions of *e.g.* how to calculate the partition function of the reactant and transition state. One of the most prominent versions is harmonic transition state theory (HTST). In HTST the transition state is assumed to be centered on the first order saddle point, *i.e.*, the transition structure.* For the calculation of the partition functions for the HTST rate constants, the rigid-rotor-harmonic-oscillator approximation is used. In variational transition state theory (VTST) the position of the dividing surface is varied to minimize the reaction rate and the recrossing which is neglected in TST.[135,136] Transition state theory and the different versions have been extensively reviewed in the last decades.[137–139]

Semiclassical instanton theory can also be understood as a transition state theory as explained in section 6. In the following, the calculation of the partition function of reactant state and transition state within HTST are explained.

---

*Unfortunately, *transition state* and *transition structure* share the same acronym, TS.

5.1.1 Partition Function of the Reactants and Transition State

The HTST reaction rate constant is proportional to the ratio of the partition functions of transition state and reactant state, see equation (5.2). Therefore, it is crucial to calculate both Q_{TS} and Q_{RS} accurately and also with the same level of precision to benefit from error cancellation.

In the canonical ensemble, *i.e.,* when the system is in thermal equilibrium and the temperature T, volume V, and the particle number N are conserved, the partition function is the sum over all quantum states weighted by the Boltzmann factor:

$$Q = \sum_{i=0}^{\text{states}} e^{-\frac{\mathcal{E}_i}{k_{\mathrm{B}}T}} \tag{5.3}$$

Here, degenerate states have to be summed up explicitly. The probability of finding a particle in state i with corresponding energy $\mathcal{E}_i$ is

$$p_i = \frac{e^{-\frac{\mathcal{E}_i}{k_B T}}}{Q}. \tag{5.4}$$

In HTST it is assumed that the electronic, translational, rotational, and vibrational contributions to the total energy are decoupled from each other. Based on this, it directly follows that the different contributions of the partition function are separable and the total partition function can be written as

$$Q = Q_{\mathrm{el}} \cdot Q_{\mathrm{trans}} \cdot Q_{\mathrm{rot}} \cdot Q_{\mathrm{vib}} \tag{5.5}$$

For unimolecular reactions, the reactant state is the PRC. In the case of bimolecular reactions, it is assumed that the two separated reactants do not interact with each other before the course of reaction and thus, the product of the partition functions of both reactants is used:

$$Q_{\mathrm{RS}} = Q_{\mathrm{A}} \cdot Q_{\mathrm{B}} \tag{5.6}$$

For the first-order saddle point, the same expressions for the individual contributions are valid except for the vibrational partition function: As there is one negative eigenvalue of the Hessian matrix corresponding to the negative curvature of the potential in the direction of the transition mode, there is one mode less to sum over.

In the following the different assumptions and approximations are shown.

5.1.2 Electronic Partition Function

The Born-Oppenheimer approximation leads to the separability of the electronic and the nuclear wave functions. The electronic partition function is determined by the number of electronic eigenstates accessible at the respective temperature, *i.e.,* when the first excited state is energetically far away, the electronic partition function is simply the level of degeneracy of the electronic ground state. If there are low lying electronically excited states, one has to take them into account by weighting them with the Boltzmann factor,

$$Q_{\mathrm{el}} = \sum_{n} g_n \exp\left(-\frac{V_{\mathrm{el},n}}{k_{\mathrm{B}}T}\right), \tag{5.7}$$

where $V_{\mathrm{el},n}$ is the electronic energy of the n^{th} state and g_n is the corresponding level of degeneracy which may be the spin degeneracy of $2S+1$ or stem from molecular symmetry.

5.1.3 Translational Partition Function

The partition function for molecules in the gas phase is usually approximated using the three-dimensional particle-in-a-box model. For large box sizes, the energy levels are closer and the summation over all energy levels n can be replaced by an integral:

$$Q_{\mathrm{trans}} \approx \int_0^{\infty} \exp\left(-\frac{(n_x^2+n_y^2+n_z^2)\,h^2}{8mL^2k_{\mathrm{B}}T}\right) \mathrm{d}n_x \mathrm{d}n_y \mathrm{d}n_z = \left(\frac{mk_{\mathrm{B}}T}{2\pi\hbar^2}\right)^{\frac{3}{2}} \cdot V \tag{5.8}$$

where m is the mass of the particle and $V = L^3$ is the volume of the box.

5.1.4 Rotational Partition Function

In principle there is a coupling between rotational and vibrational motion caused *e.g.* by centrifugal expansion of the molecules. Such rotational-vibrational couplings can be accounted for by calculation of the vibrational energy levels using an effective potential depending on the rotational quantum number J.[140] A cost-effective alternative for this rigorous approach is J-shifting introduced by Bowman in 1991.[141] In this approach, the potential energy for $J = 0$ is used throughout and the approximation of a rigid rotor is then used to calculate the impact of molecular rotation explicitly, *i.e.,* the rotational partition function.

In most cases, the rotational partition function is treated like the translational partition function the energy levels of the rotational states are assumed to lie close together and the sum is replaced by an integral. For diatomic molecules this leads to

$$Q_{\mathrm{rot,cl}} = \frac{1}{\sigma} \int_0^\infty g_J \exp\left(-\frac{BJ(J+1)}{k_\mathrm{B}T}\right) \mathrm{d}J \tag{5.9}$$

leading to

$$Q_{\mathrm{rot,cl}} = \frac{1}{\sigma} \frac{k_\mathrm{B}T}{B} \tag{5.10}$$

Here, $g_J = 2J + 1$ is the degeneracy of the rotational energy level J and $B = \frac{\hbar^2}{2\mu r_e^2}$ is the so-called rotational constant. μ and r_e are the reduced mass and the equilibrium distance between the two atoms, respectively. The formula can be extended for polyatomic molecules although there is no closed form available for asymmetric tops.[142] To account for symmetry, the result of the integral is divided by the symmetry factor, σ, which is the product of the orders of the rotational subgroups of the molecular point group.[143] It follows $\sigma(C_{2v}) = 2$ for *e.g.* water, $\sigma(C_{\infty v}) = 1$, for hetero–diatomics, $\sigma(D_{\infty h}) = 2$, for homo–diatomics, and $\sigma(C_1) = 1$ for molecules without any rotational symmetry. For bigger molecules, the moments of inertia become larger and therefore the energy levels lie closer together. The same value for the diatomic rotational partition function is also obtained by the phase space integral of a rigidly rotating rod, *i.e.,* the classical rotational partition function.

For most molecules and temperatures the integral approximation is justified. Nevertheless, if the moment of inertia, I is small, and the rotational temperature

$\theta_r = \frac{B}{k_\mathrm{B}}$ is small compared to the temperature of the system, the rotational energy levels are no longer close enough and the integral approximation is not valid.

Furthermore, for homo-diatomics the correct symmetry of the nuclear spin wave function has to be considered accordingly to the spin-statistics theorem:

$$\Psi(1,2) = \pm\Psi(2,1) \tag{5.11}$$

The wave function has to be antisymmetric for an exchange of two fermions (such as protons with half-integer spin $S_\mathrm{H} = \frac{1}{2}$) and symmetric for an exchange of two bosons (such as deuterons with an integer spin of $S_\mathrm{D} = 1$). The electronic and vibrational wave functions are always symmetric with respect to an interchange of two identical nuclei and the translational wave function is independent of the nuclei. Therefore the rotational and nuclear spin wave functions determine the symmetry of the total wave function. For a diatomic molecule, the rotational wave function, ψ_{rot} is antisymmetric for odd values of J and is symmetric for even values of J.

For H_2 the two nuclear spins can either couple to a symmetric triplet state or to an antisymmetric singlet state. The former spin isomer is called *ortho*-hydrogen (o-H_2) and possesses three possible nuclear spin states. The singlet spin isomer is called *para*-hydrogen (p-H_2) and possesses one possible spin state. As the *ortho*-*para* transition is forbidden without external spin-lattice relaxation, one can regard H_2 to be a mixture of *ortho*- and *para*- molecules.[144]

To ensure the correct symmetry of the total wave function, *ortho*-hydrogen can only have rotational wave functions with an odd value of J and *para*-hydrogen can only have rotational wave functions with an even value. When accounting for the right nuclear spin symmetry, the symmetry number σ is not to be included as this was just introduced *ad hoc* to account for the nuclear spin symmetry implicitly. To make the values obtained by this summation comparable to the ones obtained by the classical rotational partition function, $Q_{rot,cl}$ (which includes the factor $\frac{1}{\sigma}$), the summation over all states has to be divided by the total number of nuclear spin states which is four in the case of H_2 molecules. It follows for the rotational partition function of an H_2 molecule

$$Q_{\mathrm{rot,H_2}} = \frac{1}{4}\sum_{J=0}^{\mathit{even}} g_J \exp\left(-\frac{BJ(J+1)}{k_\mathrm{B}T}\right) + \frac{3}{4}\sum_{J=1}^{\mathit{odd}} g_J \exp\left(-\frac{BJ(J+1)}{k_\mathrm{B}T}\right). \qquad (5.12)$$

For D_2 molecules (both nuclei being bosons) the wave function has to be symmetric with respect to the exchange of both nuclei, which leads to the rotation partition function of

$$Q_{\mathrm{rot,D_2}} = \frac{6}{9}\sum_{J=0}^{\mathit{even}} g_J \exp\left(-\frac{BJ(J+1)}{k_\mathrm{B}T}\right) + \frac{3}{9}\sum_{J=1}^{\mathit{odd}} g_J \exp\left(-\frac{BJ(J+1)}{k_\mathrm{B}T}\right). \qquad (5.13)$$

The factors $\frac{1}{4}$ and $\frac{3}{4}$ of para- and ortho-H_2 as well as $\frac{6}{9}$ and $\frac{3}{9}$ of para- and ortho-D_2 alternate. The high-temperature limit averaging over all J-states results in a prefactor of $\frac{1}{2} = \frac{1}{\sigma}$ due to nuclear spin symmetry.

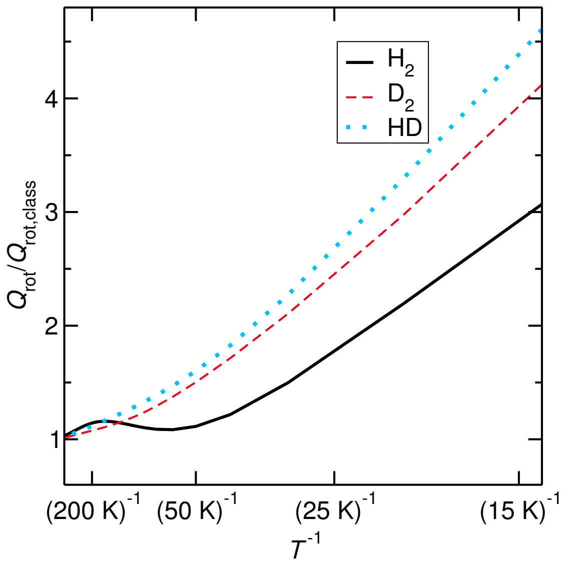

Figure 5.2 Ratio of the quantum mechanical rotational partition functions of H_2, D_2, and HD and the rotational partition functions of the corresponding classical rotors. For the quantum mechanical rotors, the J states are summed up explicitly and *ortho-/para-*nuclear spin symmetry is included. For the calculation of the partition function of the classical rotors, equation (5.10) was used.

In Fig. 5.2 the temperature dependence of $\frac{Q_{rot}}{Q_{rot,cl}}$ for H_2, HD, and D_2 is shown. It can be seen that for these three molecules the classical-rotor approximation is valid down to a temperature of 100 K. For lower temperatures the quality of the classical-rotor approximation becomes poorer. At 100 K the induced error is around 10-15 % but increases to a factor of 3.3 for HD at 20 K.

5.1.5 Vibrational Partition Function

Molecular vibrations are approximated by harmonic oscillators leading to the vibrational energy of

$$E_{\text{vib}} = \sum_{i=1}^{N_{\text{modes}}} \left(v_i + \frac{1}{2} \right) \hbar\omega_i \tag{5.14}$$

which includes the zero-point energy. For non-linear molecules the number of modes is $N_{\text{modes}} = 3N - 6$, and for linear molecules, $N_{\text{modes}} = 3N - 5$, where N is the number of atoms. Due to the harmonic approximation the vibrational modes are uncoupled. The partition function can be expressed in closed form:

$$Q_{\text{vib}} = \prod_{i=1}^{N_{\text{modes}}} \frac{\exp\left(-\frac{\hbar\omega_i}{2k_{\text{B}}T}\right)}{1 - \exp\left(-\frac{\hbar\omega_i}{k_{\text{B}}T}\right)} \tag{5.15}$$

The harmonic approximation can be assumed to perform well enough for most chemical reactions although anharmonicity have been shown to affect rate constants slightly.[145,146] For example, the mode related to the motion of the two reactants against each other in the PRC is expected to be affected by anharmonicity.

5.2 An Implicit Surface Model

In section 4.1 the ER and LH mechanisms of surface chemistry are discussed and expressions for the reaction rates have been given. For astrochemical surface chemistry, several effects of the surface on chemical reactivity have to be considered:[68,76]

1. For strongly exothermic reactions, the excess heat of reaction can dissipate into an ice bulk when the reaction proceeds on a surface. As TST assumes

thermal equilibrium during the whole reaction, the excess heat of reaction is assumed to be removed instantly.

2. Due to the low-pressure environment in the interstellar medium, the local concentration of reactive species is higher on the surface. The expression for the reaction rates depending on the concentration of reacting species is discussed in 4.1.

3. The reaction path can be altered due to the interactions of the adsorbed molecular system and the surface. When the effective energy barrier is reduced, *e.g.* by splitting up into several elementary reaction steps, a classical catalytic effect occurs. For some chemical reactions, atomistic *ab initio* calculations reveal that the potential energy along the reaction path hardly changes when the surface is involved, *i.e.,* there is just a negligible classical catalytic effect.

4. The mobility of the adsorbed molecules is restricted, in particular translation and rotation.

The restrained mobility on the surface can be taken care of by mimicking the effect of the ice surfaces on the partition function.[68,76] For unimolecular reactions the surface system under study is assumed to not perform any rotational motion as the surface has a high total mass and moment of inertia. The rotational partition function can then assumed to be constant during the reaction:

$$\frac{Q_{\mathrm{rot}}^{\mathrm{TS}}}{Q_{\mathrm{rot}}^{\mathrm{RS}}} = 1 \tag{5.16}$$

This approach is labeled *implicit surface model.* For a unimolecular reaction, it can be assumed that the moments of inertia stay rather constant during the reaction, because the whole system consisting of the surface atoms and the ad-atoms, is accounted for in molecular simulations. The translational partition function does not change for unimolecular reactions, see equation (5.8).

For bimolecular reactions following the ER mechanism, the rotational and translational partition functions of the adsorbed molecule and the transition state are assumed to be equal in the *implicit surface model.* Only the rotation and translation of the incoming particle are considered in the reactant state, see reaction (R 12).

The *implicit surface model* can be used by performing calculations on a gas-phase structural model and mimicking a surface reaction when the potential energy during the chemical reaction is not affected by the surface environment. This is only valid when there is no classical catalytic effect involved. This can be checked using small molecular clusters in the vicinity of the reactants.

5.3 Tunneling Corrections

In principle, the rigorous solution of the time-dependent Schrödinger equation, *e.g.* in the form of wave packet dynamics,[147] the multi-configuration time-dependent Hartree (MCTDH) approach[148–151] or other approaches[152,153] are the most accurate way of handling nuclear quantum effects such as atom tunneling. Nevertheless, these methods can only be applied for small model systems and a strongly restricted number of degrees of freedom. For this reason, HTST or VTST reaction rates are often calculated and the nuclear quantum effects are accounted for by multiplication of the TST rate constant with a tunneling correction factor κ.[1]

One of the the simplest correction schemes is to assume a particular shape of the potential energy barrier for which κ can be calculated analytically. These forms of the potential energy barrier are rather simple, such as rectangular or parabolic barriers.[154] The latter is sometimes referred to as Bell's tunneling correction. Somewhat more realistic models for potential energy barriers are the Eckart barrier[155] and Zero-curvature-tunneling.[156,157]. They are designated as one-dimensional tunneling corrections as they assume the tunneling path to be identical to the minimum-energy path.[1,21]

When atom tunneling is more pronounced, the tunneling path tends to be shortened at the expense of a slightly higher potential energy, which is called the corner cutting effect.[2,8] This is taken into account in so-called multidimensional tunneling methods.[1,136,158] One of the most popular and successful methods to calculate approximative tunneling rate constants is the small-curvature tunneling correction (SCT).[159] In SCT the tunneling path is approximated by the path of the concave-side turning points for the stretch vibration of the vibrational ground state orthogonal to the reaction coordinate. The shortening of the tunneling path is pushed to extremes in the large-curvature tunneling correction (LCT),[160,161] which approximates the tunneling path by a linear path from reactants' potential well to products' potential well. The microcanonically optimized multidimensional tunneling method, μOMT, takes into account that the optimal tunneling path is somewhere between the two extreme cases, the minimum-energy path and a straight line between reactants and products. This is achieved by calculating the energy-dependent transmission probabilities evaluated by the SCT and LCT method at a given energy, taking the larger one and Boltzmann averaging to obtain the tunneling correction factor κ.[136,162,163]

6 Instanton Theory

The accurate description of atom tunneling is crucial for the calculation of precise reaction rate constants. An efficient yet accurate method to incorporate atom tunneling in calculations is semiclassical instanton theory.[127,164–167] Instanton theory can be understood as a quantum mechanical analog to (semi-) classical TST, thus, referred to as harmonic quantum transition state theory.[23,168–170] The applicability of instanton theory to the quantification of atom tunneling in molecular systems has been frequently demonstrated in the past decade.[1,38,128,171–182] The idea of instanton theory is to optimize the most likely tunneling path, the so-called instanton, and calculate the quantum mechanical partition function within the harmonic approximation. It does not require the full potential energy hypersurface, but can be used with so called *on-the-fly direct dynamics* calculations, this means, the energies, 1st and 2nd derivatives of the electronic potential are evaluated when necessary. The theoretical background is outlined in the following section.

Following the *Imaginary F* premise[165,166,183,184] the decay rate of a system can be calculated to be

$$k = -\frac{2}{\hbar}\,\mathrm{Im}(F) \tag{6.1}$$

with the free energy F depending on the (complex) partition function Q:

$$F = -\frac{1}{\beta}\ln(Q) \approx -\frac{1}{\beta}\frac{\mathrm{Im}(Q)}{\mathrm{Re}(Q)} \tag{6.2}$$

Here, the dominating real part of the partition function is related to the reactant and the imaginary part of the partition function belongs to the instanton.[184,185] This leads to an expression similar, but not equivalent, to the TST rate equation, see equation (5.2):[185]

$$k = \frac{2}{\beta\hbar}\frac{Q_{\mathrm{inst}}}{Q_{\mathrm{RS}}} \tag{6.3}$$

with $Q_{\mathrm{RS}} = \mathrm{Re}(Q)$ and $Q_{\mathrm{inst}} = \mathrm{Im}(Q)$ being the partition function of the reactant state and the instanton, respectively.[186]

6.1 Representation of the Partition Function as Path Integral

In classical mechanics there is only one possible path for the propagation of a particle. In Feynman's interpretation of quantum mechanics, all possible paths contribute to the probability of an event.[187]

The contributions of all paths have to be summed up, even unlikely ones, which are obviously classically forbidden, have to be considered. The propagation of a particle from $\boldsymbol{x}_i$ to $\boldsymbol{x}_f$, can be expressed by the path integral representation of the Schrödinger propagator

$$\langle \boldsymbol{x}_f | e^{-\frac{\mathrm{i}}{\hbar}\hat{H}T} | \boldsymbol{x}_i \rangle = \int_{\boldsymbol{x}_i}^{\boldsymbol{x}_f} \mathcal{D}\mathbf{x}(t) e^{-\frac{\mathrm{i}}{\hbar}S[\mathbf{x}(t)]}. \tag{6.4}$$

Here, $\int \mathcal{D}\mathbf{x}$ has the meaning of integration over all paths and $S[\mathbf{x}(t)]$ is the action of the respective path $\mathbf{x}(t)$. Note, that $\boldsymbol{x}$ (bold italic), as used before, stands for positions of a molecular system, *i.e.,* a point on the potential hypersurface, and $\mathbf{x}$ (bold upright) stands for paths on the potential energy hypersurface.

In general, the canonical partition function of a quantum mechanical ensemble is given by the trace of the Boltzmann operator,

$$Q = \mathrm{tr}\left[e^{-\beta\hat{H}}\right] = \int_{-\infty}^{+\infty} \mathrm{d}\boldsymbol{x} \, \langle \boldsymbol{x} | e^{-\beta\hat{H}} | \boldsymbol{x} \rangle \,. \tag{6.5}$$

The position representation is similar to equation (6.4) and the partition function can be expressed as a path integral:

$$Q = \int_{-\infty}^{+\infty} \mathrm{d}\boldsymbol{x} \int_{\boldsymbol{x}(\tau=0)=\boldsymbol{x}_i}^{\boldsymbol{x}(\tau=\beta\hbar)=\boldsymbol{x}_f\equiv\boldsymbol{x}_i} \mathcal{D}\mathbf{x} \; e^{-\frac{1}{\hbar}S_{\mathrm{E}}[\mathbf{x}]} \tag{6.6}$$

Because the trace in equation (6.5) only operates on the diagonal elements of the density matrix, only closed paths have to be taken into account. Here, S_E is the Euclidean action functional given by

$$S_\mathrm{E}[\mathbf{x}(\tau)] = \int \mathrm{d}\tau \left(\frac{m}{2} \left(\frac{\mathrm{d}\boldsymbol{x}(\tau)}{\mathrm{d}\tau} \right)^2 + V(\boldsymbol{x}(\tau)) \right), \tag{6.7}$$

after a Wick rotation[188] from the real time to the imaginary time, $\mathrm{i}t \rightarrow \tau = \beta\hbar$.

The paths $\mathbf{x}(\tau)$ can therefore also be interpreted as classical motion in the inverted potential $-V(\boldsymbol{x})$ where the start and end points have to be identical. In order to evaluate

$$Q = \int \mathrm{d}\boldsymbol{x} \int \mathcal{D}\mathbf{x} \, \exp\left(-\frac{1}{\hbar} \int_0^{\beta\hbar} \mathrm{d}\tau \left(\frac{m}{2} \left(\frac{\mathrm{d}\mathbf{x}(\tau)}{\mathrm{d}\tau} \right)^2 + V(\mathbf{x}(\tau)) \right) \right), \tag{6.8}$$

the path has to be discretized and the integration approximated. Here, the path $\mathbf{x}$ is discretized first. After that, the integration of equation (6.7) is approximated harmonically to calculate the partition function, equation (6.8).

6.2 Discretization of the Feynman Path

The discretization is performed by finite differences. The path $\mathbf{x}$ is split into P segments of equal distance in imaginary time, $\Delta\tau = \frac{\beta\hbar}{P}$. In its discretized form, the path consists of P images on the N-dimensional hypersurface. The derivative $\frac{\mathrm{d}\boldsymbol{x}(\tau)}{\mathrm{d}\tau}$ was discretized by finite differences. For $P \rightarrow \infty$ the path integral and the expression of the action are exact. The functional $S_\mathrm{E}[\mathbf{x}(\tau)]$ transforms into a function of all $(N \cdot P)$ coordinates of the P different images of the path:

$$S_\mathrm{E} = \sum_{k=1}^{P} \left(\frac{P}{2\beta\hbar} (\boldsymbol{y}_k - \boldsymbol{y}_{k-1})^2 + \frac{\beta\hbar}{P} V(\boldsymbol{y}_k) \right) = \frac{S_0}{2} + S_\mathrm{pot} \tag{6.9}$$

where the cyclic constraint $\boldsymbol{y}_0 = \boldsymbol{y}_P$, mass-weighted coordinates $y_k = \sqrt{m} x_k$ and the abbreviations

$$S_0 = \frac{P}{\beta\hbar} \sum_{k=1}^{P} (\boldsymbol{y}_k - \boldsymbol{y}_{k-1})^2, \tag{6.10}$$

and

$$S_{\mathrm{pot}} = \frac{\beta\hbar}{P} \sum_{k=1}^{P} V(\boldsymbol{y}_k). \tag{6.11}$$

have been used.

6.3 Partition Function of the Instanton

After the discretization, the partition function reads

$$Q = \int_{-\infty}^{\infty} \mathrm{d}^{N\cdot P} y \exp\left(\frac{-S_{\mathrm{E}}(\boldsymbol{y}_1, \boldsymbol{y}_2, \ldots, \boldsymbol{y}_P)}{\hbar}\right) \tag{6.12}$$

The resulting $(N \cdot P)$-dimensional integral can be solved using Laplace's method. For that, $S_{\mathrm{E}}(\mathbf{y})$ is expanded into a Taylor series around a stationary point of Euclidean action:

$$S_{\mathrm{E}}(\mathbf{y}) = S_{\mathrm{E}}(\mathbf{y}_{\mathrm{stat}}) + \frac{\mathrm{d}S_{\mathrm{E}}}{\mathrm{d}\mathbf{y}}\Delta\mathbf{y} + \frac{1}{2}\Delta\mathbf{y}^T\mathbf{S}''\Delta\mathbf{y} + \mathcal{O}(\Delta\mathbf{y}^3) \tag{6.13}$$

where $\Delta\mathbf{y} = \mathbf{y} - \mathbf{y}_{\mathrm{stat}}$ is the deviation of a path $\mathbf{y}$ from the path with stationary Euclidean action and $\mathbf{S}'' = \frac{\mathrm{d}^2 S_{\mathrm{E}}}{\mathrm{d}\mathbf{y}^2}$ is the Hessian matrix of the Euclidean action. The steepest descent method requires a path with stationary Euclidean action with respect to the position of the path $\mathbf{y}$, *i.e.,* $\frac{\mathrm{d}S_{\mathrm{E}}}{\mathrm{d}\mathbf{y}} = \mathbf{0}$.

The transition state in instanton theory is the instanton. This is the closed Feynman path which is a 1st order saddle point of the Euclidean action $S_{\mathrm{E}}[\mathbf{x}]$. Thus, the instanton optimization is reduced to a saddle point search in $N \cdot P$ dimensions.[23,189,190]

Equation (6.9) can be rewritten as

$$S_{\mathrm{E}} = \beta\hbar \sum_{k=1}^{P} \left(\frac{k_{\mathrm{spring}}}{2}\left(\boldsymbol{y}_k - \boldsymbol{y}_{k-1}\right)^2 + \frac{V(\boldsymbol{y}_k)}{P}\right) \tag{6.14}$$

by defining an artificial spring constant $k_{\mathrm{spring}}(\beta) = \frac{P}{(\beta\hbar)^2}$. The whole closed path can therefore be understood as a chain of P images which are connected by temperature dependent Hookean springs and move classically in the potential $\frac{V(\mathbf{y})}{P}$, often called ring-polymer. Instanton theory is applicable only for temperatures below the crossover temperature[191]

$$T_\mathrm{C} = \frac{\hbar\omega}{2\pi k_\mathrm{B}}, \tag{6.15}$$

where ω is the absolute value of the imaginary frequency at the transition structure. The crossover temperature is mass-dependent as ω is mass-dependent, too. In many cases, T_C can be used as a first indication at which temperature atom tunneling becomes important. If ω is larger than 1300 cm^{-1}, atom tunneling can be expected to be relevant at room temperature. At temperatures higher than T_C, the spring forces between the individual images are too strong and the ring-polymer collapses to the transition structure. For temperatures below T_C, the k_spring becomes weaker and the instanton spreads out. For exothermic reactions and $T \to 0$ K, the instanton reaches the reactant state coordinate.

In the discretized form, the instanton is a closed Feynman path with pairwise identical coordinates. The instanton, more precisely, the path between the turning points of the instanton, *i.e.,* the half of the instanton , can also be considered the most likely tunneling path, *i.e.,* the region in configuration space the molecule tunnels through. In general, instantons deviate from the IRC due to the corner cutting effect as explained in the previous section. The instanton and the steepest-descent paths on the potential energy hypersurface, starting from the instanton's turning points, can be considered as the most likely trajectory at a certain temperature, called *tunneling reaction path.* For temperatures above T_C, when the instanton collapses to the transition structure, the IRC, is also the tunneling reaction path. At lower temperatures, the instanton, and therefore the tunneling reaction path, deviate qualitatively from the IRC, see Fig. 6.1.

As $\mathbf{y}_\mathrm{stat}$ is a stationary point of Euclidean action, the first derivative, $\frac{\mathrm{d}S_\mathrm{E}}{\mathrm{d}\mathbf{y}}$, vanishes. Equation (6.12) turns into a multidimensional Gaussian integral and results in

$$Q = I_1 \cdot I_2 \cdot \sqrt{\frac{(\pi\hbar)^{NP-2}}{\prod_{l=3}^{NP} \lambda_l}}\; e^{-S_\mathrm{E}(\mathbf{y}_\mathrm{stat})/\hbar} \tag{6.16}$$

where λ_l are the eigenvalues of $\mathbf{S}''$. The terms I_1 and I_2 stand for the integration over the first and second modes of the instanton, respectively, since the Gaussian

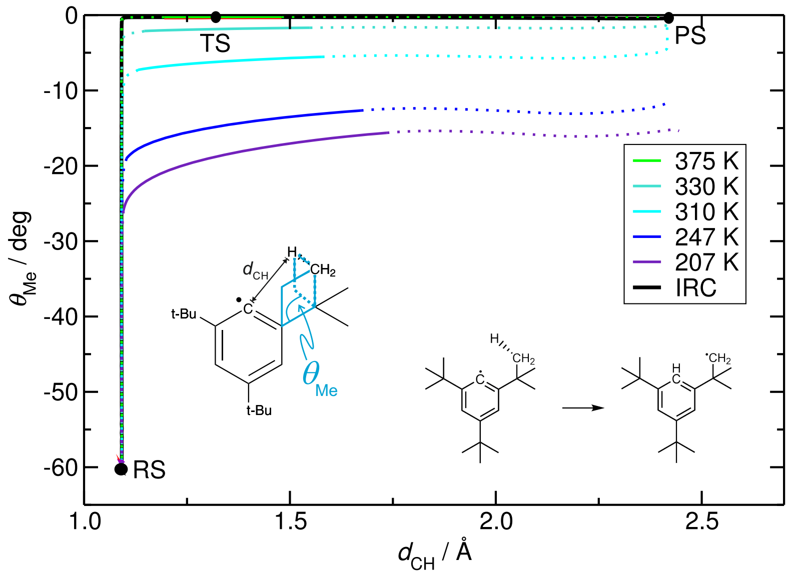

Figure 6.1 Projection of instanton paths and the classical path on two coordinates for a hydrogen transfer reaction with $T_C = 414$ K, see reference 2. The black solid line represents the minimum-energy path, the IRC. Colored lines represent instantons at different temperatures. The instantons spread out at lower temperatures. The dotted lines correspond to steepest-descent paths starting from the instantons' turning points. Adapted from Ref. 2 with permission from the PCCP Owner Societies.

integration only holds for $\lambda_l > 0$. Therefore, the two eigenvalues λ_1 and λ_2 need special attention: Since the instanton is a 1^{st} order saddle point of the Euclidean action, one eigenvalue λ_1 is negative. This integral can be solved using analytical continuation. Another eigenvalue $\lambda_2 = 0$ is related to a cyclic permutation of the P images, *i.e.*, $\boldsymbol{y_k} \rightarrow \boldsymbol{y_{k+i}}$, The integration of these two modes is shown in the literature in detail[164,192,193] and leads to

$$I_1 = \frac{\mathrm{i}}{2}\sqrt{\frac{\pi\hbar}{|\lambda_1|}} \tag{6.17}$$

and:

$$I_2 = \frac{P}{\sqrt{2}}\sqrt{\sum_{k=1}^{P}\left(\mathbf{y}_k - \mathbf{y}_{k-1}\right)^2} \tag{6.18}$$

6.4 Partition Function of the Reactant State

The closed Feynman paths of the reactant state are simply collapsed to the minimum geometry of the potential energy hypersurface $V(\boldsymbol{x})$ for all temperatures. This path is also a minimum of the action surface S_E and all $N \cdot P$ eigenvalues λ_l^RS are positive. This makes the steepest-descent integration applicable to all degrees of freedom and it follows for the reactant state's partition function

$$Q_\mathrm{RS} = \sqrt{\frac{(\pi\hbar)^{NP}}{\prod_{l=1}^{NP} \lambda_l^\mathrm{RS}}}\, e^{-S_\mathrm{E}[\mathbf{y}^\mathrm{RS}]/\hbar} \tag{6.19}$$

with

$$S_\mathrm{E}[\mathbf{y}^\mathrm{RS}] = S_\mathrm{pot}[\mathbf{y}^\mathrm{RS}] = \beta\hbar\, V(\boldsymbol{y}^\mathrm{RS}). \tag{6.20}$$

6.5 Rate Expression of the Instanton

Inserting the partition functions of the instanton and the reactant state into the rate expression, equation (6.3), the reaction rate constant can be calculated to be

$$\tilde{k}_\mathrm{inst} = \sqrt{\frac{S_0 P}{2\pi\beta\hbar^2}}\, \sqrt{\frac{\prod_{l=1}^{NP} \lambda_l^\mathrm{RS}}{\prod_{l=1}^{\prime NP} |\lambda_l^\mathrm{inst}|}}\, \exp\left(\frac{-\frac{S_0(\mathbf{y}_\mathrm{inst})}{2} - S_\mathrm{pot}(\mathbf{y}_\mathrm{inst}) + S_\mathrm{pot}(\mathbf{y}_\mathrm{RS}\ )}{\hbar}\right) \tag{6.21}$$

where the prime on the product sign of the instanton's eigenvalues stands for the exclusion of λ_2, which is the eigenvalue corresponding to the cyclic permutation of the images, see equation (6.18).

This rate expression does not account for molecular translation and rotation, yet. To achieve this, the rate has to be multiplied with the corresponding partition functions

$$k_\mathrm{inst} = \tilde{k}_\mathrm{inst} \cdot \frac{Q_\mathrm{trans,inst}}{Q_\mathrm{trans,RS}} \cdot \frac{Q_\mathrm{rot,inst}}{Q_\mathrm{rot,RS}} \tag{6.22}$$

For this purpose, the rotational and translational partition functions are calculated as described in section 5.1.1 and the instanton is assumed to be a super-molecule consisting of all atoms of all images with their mass divided by P.

7 Dual-Level Instanton Method

The calculation of the electronic potential is often the most time-consuming step in theoretical investigations. For this reason, a less demanding computational method is often used for geometry optimizations and Hessian calculations, while the energy is recalculated applying a more accurate electronic structure method. The underlying assumption is that the faster method is still able to produce the right molecular geometries for reactants, transition structure, and products. The harmonic frequencies and zero-point energies can be corrected by multiplication with scaling factors.[194] The results obtained in this way generally agree very well with results obtained with the more accurate electronic potential. Dual-level approaches or even multilevel approaches are also used for the calculation of potential energy hypersurfaces which can be used for *e.g.* computational vibrational spectroscopy.[195] Rate calculations using different tunneling corrections such as SCT and μOMT also utilized a dual-level ansatz successfully.[196–198]

The applicability of the instanton method increased in 2011 with the publication of the quadratically converging Newton-Raphson (NR) instanton optimizer by Rommel *et al.*.[189] Before that, instanton paths were often guessed or approximated using further assumptions to avoid the large amount of *ab initio* calculations necessary for the accurate determination of the instanton.[199–202] With the availability of the NR optimizer, instantons could be optimized for molecular systems with many degrees of freedom.[38,128,176–182,189,203]

Still, for calculations of reaction rate constants, Hessians along the whole instanton path have to be calculated in order to calculate the quantum fluctuations around the instanton path, $\mathbf{y}_{\text{inst}}$. Therefore, most computational applications were limited in the accuracy of the underlying electronic potential due to the high computational demand of the Hessian calculation.[38,176,177,181,182]

In this thesis, a dual-level instanton approach is proposed. First the instanton is optimized for one or several temperatures using a relatively efficient on-the-fly electronic structure method. The Hessians are provided along the instanton using the same potential. Then, single point energy calculations are performed for $V(\mathbf{y})$ using a more sophisticated electronic structure method. Here, the assumption is that the basic electronic potential is able to reproduce the shape of the instantons qualitatively well. The recalculated electronic energies correct the error caused by the inaccuracy of the electronic potential. This is shown by the blue coloring and emphasized with a box in equation (7.1):

$$k_{\text{inst}}^{\textbf{Dual}} = \sqrt{\frac{S_0 P}{2\pi\beta\hbar^2}} \sqrt{\frac{\prod_{l=1}^{NP} \lambda_l^{\text{RS}}}{\prod_{l=1}^{\prime NP} |\lambda_l^{\text{inst}}|}} \exp\left(\frac{-\frac{S_0(\mathbf{y}_{\text{inst}})}{2} - \boxed{\boldsymbol{S}_{\textbf{pot}}}(\mathbf{y}_{\text{inst}}\ ) + \boxed{\boldsymbol{S}_{\textbf{pot}}}(\mathbf{y}_{\text{RS}}\ )}{\hbar} \right) \tag{7.1}$$

Hitherto, different studies combined approximate instanton methods with dual-level approaches.[200,201,204] If an instanton is not optimized rigorously on the same potential the Hessians are calculated with, the reliability of the eigenvalues is questionable, because the Euclidean action is not stationary and the steepest-descent method is not applicable. Here, for the first time, instantons are optimized in all dimensions using a basic *ab initio* electronic potential $V(\boldsymbol{x})$ *i.e.,* being true 1st order saddle points of S_{E}. A more sophisticated method is then used to correct S_{pot}. This approach results in correct eigenvalues λ_l^{inst} ($\lambda_1^{\text{inst}} < 0$ and $\lambda_2^{\text{inst}} = 0$), as the Hessian of the action, S'', is evaluated around a true stationary point of S_{E}, This is valid for the instantons and the reactant state. At first glance, a remaining inaccuracy seems to persist, namely the erroneous vibrational frequencies of the basic, efficient potential. A correction factor applied to the frequencies is, however, not necessary, because the error in the 2nd derivatives of the electronic potential is approximately systematic and therefore cancels out nearly totally, see equation (7.1).

In section 8 the results of the dual-level instanton method are compared with conventional instanton calculations.

Part III

Results

8 Performance of the Dual-Level Instanton Method

This part demonstrates the applicability of the dual-level instanton method. Here, the focus lies on the comparison of the dual-level instanton theory with conventional instanton theory. As absolute values of the reaction rate constants are of less importance for this study, no comparison with literature values is done.

Three different molecular systems were used to illustrate the performance of the dual-level instanton approach: the isomerization of HNC to HCN, an intramolecular [1,5] hydride shift, and the bimolecular hydrogen atom transfer reaction of $NH_2 + H_2 \rightarrow NH_3 + H$. For each system, reaction rate constants were calculated using the dual-level approach and are compared to the results of the conventional instanton theory at both the basic and accurate electronic potential.

For dual-level approaches in quantum chemistry, the nomenclature

$$\text{Method}_A/\text{basis set}_A//\text{Method}_B/\text{basis set}_B$$

is used. Here, A labels the level of theory and basis set of the accurate electronic potential and B refers to the basic potential. For simplicity, the basis set declaration is omitted in the shorthand notation.

$$\text{Method}_A//\text{Method}_B$$

8.1 Computational Details

All geometry optimizations including IRCs and instantons as well as rate calculations were performed using the DL-FIND optimization library interfaced to Chemshell.[205,206] Instantons were optimized until the maximum component of the gradient is smaller than $1 \cdot 10^{-8}$ a.u. (scaled relative to the electron's mass) using the adapted, quadratically convergent Newton–Raphson algorithm.[189,190] The CCSD(T)-F12[207,208] calculations were performed using molpro[209] with default settings. In all cases, the cc-pVDZ-F12 basis set was used.[210] All DFT calculations were performed with Turbomole version 7.0.1[211]. SCF energies were converged to an accuracy of 10^{-9} Hartree on an *m5* multi grid.[212]

For the isomerization of HNC to HCN and for the [1,5] sigmatropic rearrangement, 200 and 100 images, respectively, were used for all temperatures. For the reaction of $NH_2 + H_2$, 154 images were used to discretize the whole paths when using DFT. For the instantons calculated on CCSD(T)-F12 level, 40 images were used down to 219 K, 78 images down to 131 K, and 154 and 306 images for 119 K and 109 K, respectively.

8.2 Isomerization Reaction HNC → HCN

The isomerization of HNC to HCN is a standard model system for *e.g.* testing optimization algorithms.[85,213–215] It is a unimolecular prototype reaction with well-defined reactant state structure (HNC) and product state structure (HCN). Furthermore, the three-atomic system is small enough to carry out full CCSD(T)-F12/cc-pVDZ-F12[207,210,216] instanton calculations. For the basic potential, B3LYP, one of the most frequently used density functionals[217–222] was used in combination with the def2-SVP basis set.[223]

The reaction energies of both electronic potentials, ΔV, deviate by approximately 5 kJ mol^{-1}, see table 8.1. The potential activation barrier V_A of B3LYP is higher than the CCSD(T)-F12 potential activation barrier by only 6.6 kJ mol^{-1}. The crossover temperatures, *i.e.,* the negative curvatures at the corresponding transition structures, are also quite similar and deviate by just 15.9 K, that is ≈ 6 %.

The potential energy along the IRC was calculated for both electronic potentials, see Fig. 8.1. Additionally, CCSD(T)-F12 single point calculations were performed on the IRC obtained with the B3LYP potential, shown as blue crosses. That potential energy curve overlaps with the potential energy along the IRC of the

CCSD(T)-F12 potential. This indicates that the IRC coordinates are geometrically close together.

Fig. 8.2 shows Arrhenius plots obtained by conventional instanton theory using both electronic potentials as well as the CCSD(T)-F12//B3LYP-dual-level method. For B3LYP and the dual-level method, reaction rate constants down to 60 K were calculated. Due to the high computational demand, conventional CCSD(T)-F12 instanton calculations for lower temperatures than 100 K could not be performed. Due to the higher potential energy barrier, the B3LYP reaction rate constants are lower than the CCSD(T)-F12 reaction rate constants by a factor 51.4 at 200 K and by a factor 961.1 at 100 K. The reaction rate constants obtained by the dual-level method are higher than the CCSD(T)-F12 rate constants only by a factor between 2.0 and 2.5, see Fig. 8.2. Thus, here the CCSD(T)-F12//B3LYP-dual-level method resembles the results obtained with conventional CCSD(T)-F12 instanton calculations.

8.3 Intramolecular 1,5-H-Shift

In sigmatropic rearrangements, tunneling was observed in many cases. Suprafacial [1,5] sigmatropic rearrangements were studied exhaustively, using derivatives of 1,3(Z)-pentadiene.[224,225] Although it was initially unclear whether or not atom tunneling plays a crucial role in these reactions,[226,227] various studies have con-

Table 8.1 Potential energy barriers V_A, potential reaction energies ΔV and the respective values corrected by zero-point energy, E_A, and ΔE for the reaction HNC → HCN. All energies are in kJ mol^{-1}. The crossover temperatures T_C are given in K.

	Basic Potential	Refined potential	Dual-level
Method	B3LYP	CCSD(T)-F12	
Basis set	def2-SVP	cc-pVDZ-F12	
V_A	142.8	136.2	136.2
ΔV	-57.2	-62.6	-62.4
E_A	128.9	123.5	122.4
ΔE	-60.8	-65.5	-66.0
T_C	257.0	272.9	

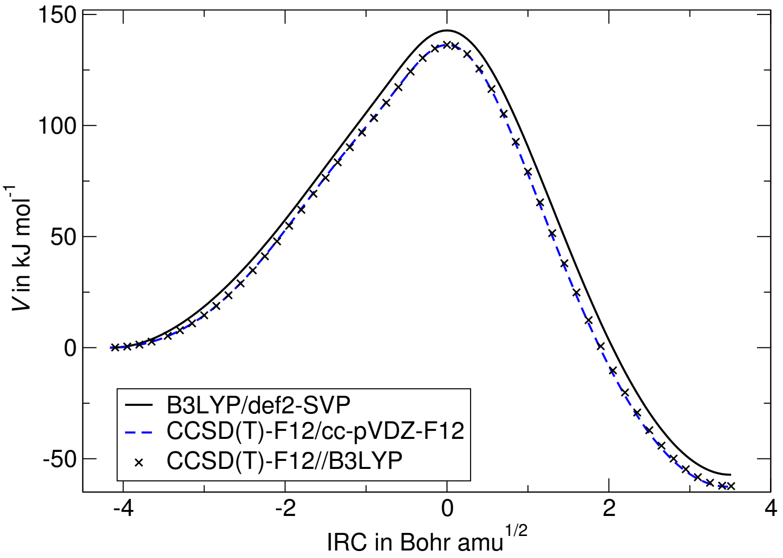

Figure 8.1 Potential energy along the IRCs of the B3LYP potential (black) and the CCSD(T) potential (blue). The black crosses indicate CCSD(T)-F12 single point energy calculations on the B3LYP IRC. The energy of the reactant (HNC) calculated on the respective potential was set to zero.

firmed its involvement.[1,178,225,228–232] The [1,5] sigmatropic rearrangement of 1,3(Z)-hexadiene to 2(E),4(Z)-hexadiene, Fig. 8.3, is therefore an appropriate test system for the dual-level instanton method.

Two distinct density functionals, the BP-86 GGA functional[217–220,233] and the BHLYP hybrid functional,[217–221,234] were applied to obtain different electronic potentials: both with the 6-31G* basis.[235]

The potential activation energy obtained by BHLYP is more than 56.8 kJ mol^{-1} higher than the one obtained by the BP86 functional. This is attributed to the high amount (50 %) of exact exchange in the BHLYP functional. Without further references it is difficult to judge which functional performs better for this particular reaction. However, the two functionals are eminently suitable to demonstrate the applicability of the dual-level method in cases where the reaction barrier is significantly underestimated by the basic potential. In this context, it has to be mentioned that, although the reaction barriers obtained by the two functionals disagree, the potential reaction energies agree within 2.8 kJ mol^{-1}, see table 8.2.

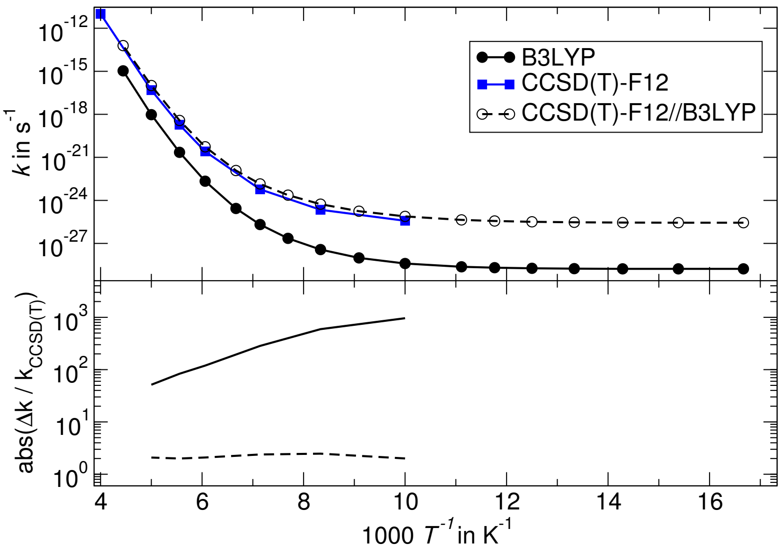

Figure 8.2 Above: Arrhenius plots calculated with the instanton method of the reaction HNC → HCN. Black: B3LYP potential. Blue: CCSD(T)-F12 potential. The dashed blue curve corresponds to the dual-level instanton results, *i.e.,* instantons optimized on the B3LYP electronic potential and the energies corrected by CCSD(T)-F12 single point calculations. Below: Absolute value of the relative error with respect to the conventional CCSD(T)-F12 results.

Using the dual-level approach (BHLYP//BP86) the potential energy along the IRC is successfully preserved, as can be seen in Fig. 8.4.

Instanton rate constants were calculated for a temperature range from 300 K to 100 K using the two density functionals as well as the BHLYP//BP86 dual-level combination. The lower energy barrier of the BP86 potential compared to the BHLYP potential leads to higher reaction rate constants by more than eight orders of magnitude throughout the whole temperature range. The curvatures of all Arrhenius plots in Fig. 8.3 are strikingly similar keeping in mind that the crossover

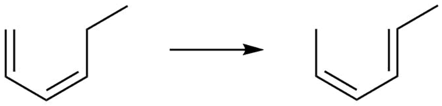

Figure 8.3 [1,5] H shift in the sigmatropic rearrangement reaction of 1,3-hexadiene to 2,4-hexadiene.

temperatures differ by more than 20 %. Despite the qualitative difference of both functionals, the BHLYP//BP86 dual-level approach reproduces the BHLYP rate

Table 8.2 Potential energy barriers V_A, potential reaction energies ΔV and the respective values corrected by zero-point energy, E_A and ΔE for the sigmatropic rearrangement reaction of 1,3-hexadiene to 2,4-hexadiene (Fig. 8.4). All energies are in kJ mol^{-1}. The crossover temperatures T_C are given in K.

	Basic Potential	Refined potential	Dual-level
Method	BP86	BHLYP	
Basis set	6-31G*	6-31G*	
V_A	110.6	167.4	166.3
ΔV	-18.0	-15.2	-15.3
E_A	100.3	156.4	155.9
ΔE	-18.9	-16.4	-16.3
T_C	308.8	394.7	

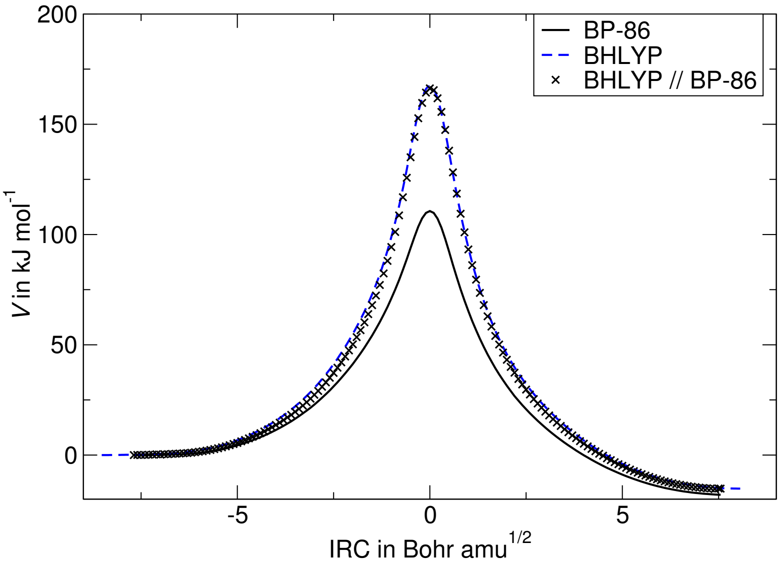

Figure 8.4 Potential energy along the IRCs of the BP86 potential (black) and the BHLYP potential (blue) for the sigmatropic [1,5] hydride shift in Fig. 8.4. The blue crosses indicate BHLYP single point energy calculations on the BP86-IRC. The energy of the reactant calculated on the respective potential was set to zero.

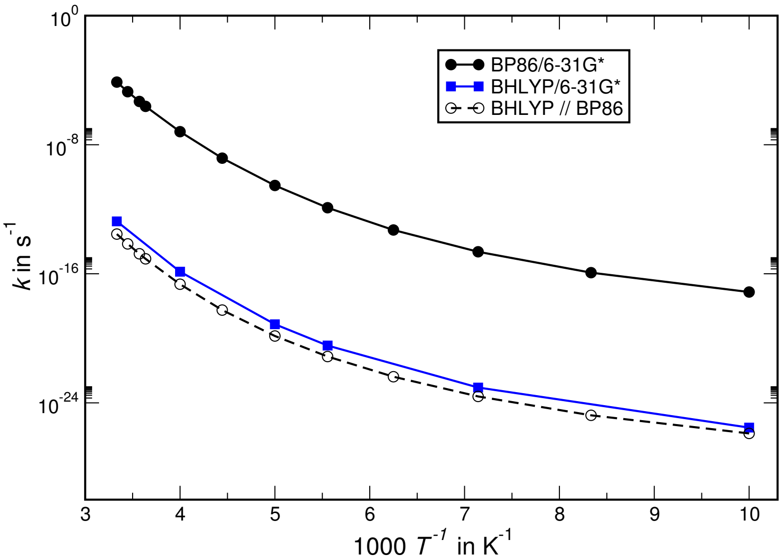

Figure 8.5 Arrhenius plots calculated with the instanton method of the reaction sigmatropic rearrangement reaction (Fig. 8.4). Black: BP86 potential. Blue: BHLYP potential. The dashed blue curve corresponds to the dual-level instanton results, *i.e.,* instantons optimized on the BP86 electronic potential and the energies corrected by BHLYP single point calculations.

constants successfully. with obtained values differing by less than one order of magnitude.

8.4 Bimolecular Reaction $NH_2 + H_2 \rightarrow NH_3 + H$

Finally, the dual-level ansatz is tested on the hydrogen atom transfer reaction $NH_2 + H_2 \rightarrow NH_3 + H$. This five-atomic test system with eleven electrons can also be handled fully on CCSD(T)-F12/cc-pVDZ-F12 level using conventional instanton theory.

Two basic electronic potentials of different quality are used: BHLYP/def2-SVP and BHLYP/6-31G*, see table 8.3. The crucial difference in the two basis sets is the absence of polarization functions for hydrogen atoms in the 6-31G* basis, which plays an important role when describing hydrogen atom transfer reactivity.[173] Besides that, the two basis sets differ also in the description of the nitrogen atom,

Table 8.3 Potential energy barriers V_A, potential reaction energies ΔV and the respective values corrected by zero-point energy, E_A and ΔE for the reaction $NH_2 + H_2 \rightarrow NH_3 + H$. All energies are in kJ mol^{-1}. The crossover temperatures T_C of the pure electronic potentials are given in K.

	Basic Pot I	Basic Pot. II	Refined Pot.	Dual I	Dual II
Method	BHLYP	BHLYP	CCSD(T)-F12		
Basis set	def2-SVP	6-31G*	cc-pVDZ-F12		
V_A	35.5	48.4	41.5	40.7	40.7
ΔV	−15.1	−2.8	−22.0	−23.2	−23.2
E_A	44.2	53.6	48.8	49.3	45.9
ΔE	−0.8	+8.7	−8.0	−9.0	−11.6
T_C	355.9	410.8	355.8		

but this is expected to be of minor importance. All three electronic potentials used here differ qualitatively in the reaction energetics, see table 8.3.

On CCSD(T)-F12 level, the electronic and vibrational adiabatic reaction energies are −22.0 kJ mol^{-1} and −8.0 kJ mol^{-1}, respectively. During the reaction, an N–H bond is formed and an H–H bond is broken, leading to a large difference in zero-point vibrational energy for the reactants and products. Both BHYLP potentials underestimate the exothermicity with and without zero-point energies. On BHLYP/6-31G* level, the vibrationally adiabatic reaction energy is even positive. Therefore, the functional is not able to describe the reaction qualitatively correctly.

The CCSD(T)-F12 single point energy calculations along the IRC calculated on BHLYP/def2-SVP level resembles the energy along the CCSD(T)-F12 IRC well enough in the region of the transition structure, see Fig. 8.6. It can therefore be assumed that BHLYP/def2-SVP is sufficiently accurate to serve as an underlying electronic potential. For the CCSD(T)-F12 single point energy calculations along the IRC calculated on BHLYP/6-31G* level, the highest point in energy is at IRC ≈ -0.2. This indicates that the 1st order saddle points of the electronic potential hypersurfaces deviate from each other. Indeed, the geometric parameters of the three potentials deviate, see table 8.4. The N–H and the H–H distances at the 1st order saddle points of the BHLYP/6-31G* potential deviate by more than

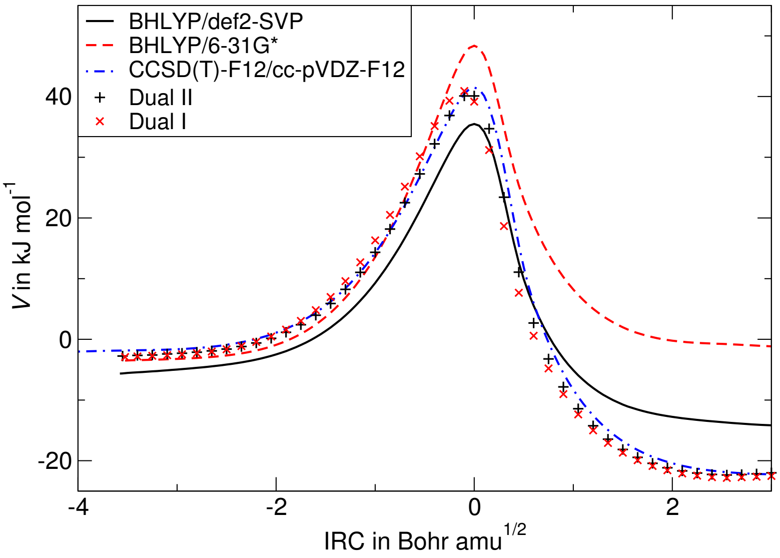

Figure 8.6 Potential energy along the IRCs of the different electronic potentials. The black crosses and red plus signs indicate CCSD(T)-F12 single point energy calculations on the geometries of the BHLYP/6-31G* and BHLYP/def2-SVP potential. The sum of the reactants' (NH_2+H_2) energies calculated on the respective potential was set to zero.

twice as much from the CCSD(T)-F12 potential than the corresponding values of the 1st order saddle points of the BHLYP/def2-SVP potential.

The reaction rate constants obtained with conventional instanton theory as well as the corresponding dual-level methods are shown in Fig. 8.7. The BHLYP/def2-SVP functional leads to higher reaction rate constants by a factor of 9–12 through-

Table 8.4 Geometric parameters of the transition structures. The values of $d_{\text{N–H}}$, the distance between the transferred hydrogen atom and the nitrogen atom and $d_{\text{H–H}}$, the distance between the two hydrogen atoms of the H_2 molecule, are given in Å. The values of $\measuredangle_{\text{H–N–H}}$ are in degrees.

	Basic Pot I	Basic Pot. II	Refined Pot.
$d_{\text{N–H}}$	1.30	1.27	1.33
$d_{\text{H–H}}$	0.90	0.91	0.88
$\measuredangle_{\text{H–N–H}}$	99.1	100.4	98.0

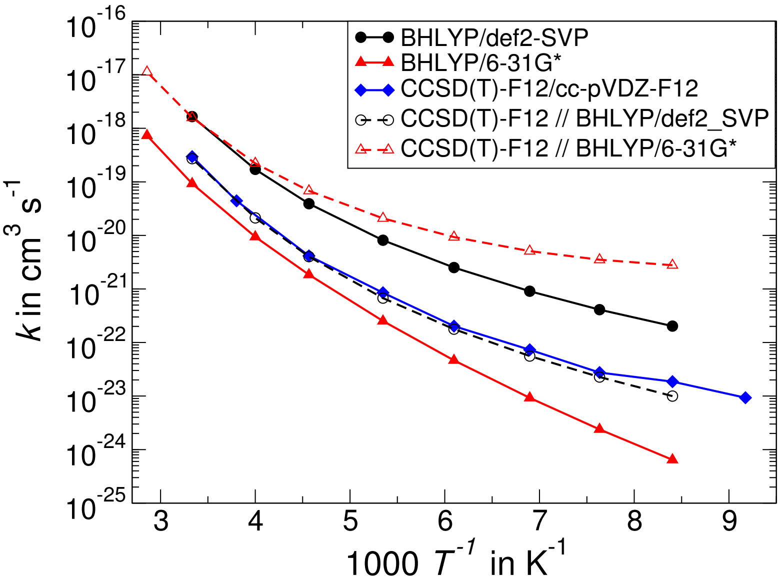

Figure 8.7 Reaction rate constants of the reaction $NH_2 + H_2 \rightarrow NH_3 + H$ calculated using the three different electronic potentials discussed in the text. Hollow points stand for the corresponding dual-level methods.

out the temperature range of 300–110 K, caused by the lower potential activation barrier. The CCSD(T)-F12//BHLYP/def2-SVP-Dual-level method successfully leads to reaction rate constants deviating only by a factor of less than 2 from the results obtained by conventional instanton theory using the CCSD(T)-F12 potential.

As the BHLYP/6-31G* potential overestimates the potential activation barrier, the reaction rate constants are too low compared to the CCSD(T)-F12 results. In this case, the dual-level methods fails and the resulting reaction rate constants are off by even more then the ones calculated using the pure BHLYP/6-31G* potential.

This error can be explained by the qualitatively wrong reaction profile of the BHLYP/6-31G* potential, which predicts the reaction to be nearly isoenergetic without considering zero-point energy and even endothermic when including zero-point energy. A qualitatively wrong potential energy hypersurface leads to an incorrect distribution of the images along the instanton path.

The image distributions of the CCSD(T)-F12 and BHLYP/def2-SVP instantons are comparable and most of the images are located on the side of the reactants.

For both potentials, the image with the highest potential energy is on the part of the instanton close to the product valley (the 59th image for for BHLYP/def2-SVP and the 64th image for CCSD(T)-F12 of 77 images for the half instanton). For the BHLYP/6-31G* instanton, the 42nd image has the highest potential energy, see Fig. 8.8.

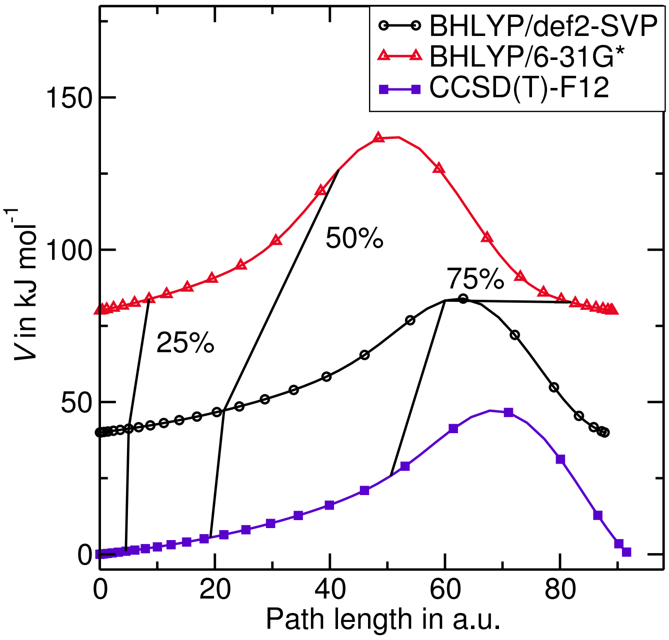

Figure 8.8 Potential energy and image distribution of the instantons optimized on the three different electronic potentials at $T = 119$ K. As the instanton is a closed Feynman path, *i.e.,* covers the same line in configuration space twice, only one half of the used images are shown. The energy of the BHLYP/def2-SVP and BHLYP/6-31G* curves is shifted by 40 and 80 kJ mol^{-1}, respectively. For clarity, just every third image is shown and lines connection 25%, 50%, and 75% of the corresponding instantons are drawn.

In this case, not only is the potential energy along the instanton path with respect to the reactant state described incorrectly, but the image distribution is also wrong. This error is not corrected by the dual-level approach.

8.5 Summary

The dual-level instanton approach can be used to calculate reaction rate constants which are nearly as accurate as the rate constants obtained by conventional instanton calculations performed on the refined potential. All optimizations and Hessian calculations are carried out using the basic, underlying potential. Additionally, only single point energy calculations of the refined potential along the instanton path are necessary. This evidently corrects for the largest part of the errors by improving the value of S_{pot} in equation (7.1). The instanton geometry $\mathbf{y}_{\text{inst}}$ and therefore the values of S_0 (see equation (6.10)) are not changed and assumed to be described well enough by the basic potential. The dual-level approach performs astonishingly well in the three cases examined above. The method still works well when the activation barrier of the basic potential, one of the most crucial parameters when considering reaction rate constants, differs by more than 40% from the one obtained with the refined potential. In cases where the geometry of the transition structure is described incorrectly, it can be assumed that the reaction and, hence, tunneling paths are also described wrongly. This could be demonstrated for the reaction of $NH_2 + H_2$ using the BHLYP/6-31G* electronic potential. In this case, the potential energy landscape is described wrongly leading to a failure of the dual-level instanton theory. Summarized, the dual-level approach should be used with care, but seems to be a legitimate correction as long as the basic potential describes the chemical reaction qualitatively correct.

9 The Reaction $H_2 + OH \rightarrow H_2O + H$

9.1 Introduction

The reaction contributes to fundamental processes in atmospheric chemistry, astrochemistry, and combustion.[236–238] The reaction on a surface is discussed in chapter 10 and this chapter focuses on the reaction in the gas phase. A number of studies on this reaction, theoretical[71,239–245] as well as experimental,[69,246–249] have been performed down to 200 K. For an overview of previous experimental and theoretical results, the reader is referred to reviews.[250,251]

As the reaction is one of the prototype reactions for four-atomic systems, a variety of potential energy surfaces (PES) have been published.[252–257] Recently, global potential energy surfaces fitted by a neural network to UCCSD(T)-F12a/AVTZ data were published [258]. One of these PES, labels NN1, was shown to give reliable results in, *e.g.,* the study of the mode specificity of the H + HOD reaction.[243] Therefore, the NN1 PES was applied here as well. Various studies on thermal reaction rate constants for the reaction have appeared.[71,245,259] One example are the semiclassical transition state theory (SCTST) calculations of Nguyen et al.[260] who even investigated reaction rate constants of all isotopologues.[71] However, it seems that this is the first study which provides rate calculations on the NN1 PES. Furthermore, no rate calculations for temperatures below 200 K have been performed before this study.

---

[*] **Parts of this Chapter have been used in:**
Reaction rates and kinetic isotope effects of $H_2 + OH \rightarrow H_2O + H$, Jan Meisner and Johannes Kästner, *J. Chem. Phys.* **144**, 174303 (2016), see reference 72 and the content is adapted with permissions. Copyright (2016) American Institute of Physics.

In this study the temperature dependence of the reaction rate constants is investigated and the tunneling effect is quantified. For that, canonical variational theory with microcanonical optimized multidimensional tunneling (CVT/μOMT)[162,163] was used along with zero curvature tunneling (ZCT),[261,262] small curvature tunneling (SCT),[159] large curvature tunneling (LCT),[160,161,263] and microcanonical optimized multidimensional tunneling (μOMT)[162,163] calculations down to 50 K. Instanton rate constants have been calculated down to 100 K.

The results are compared to published experimental and computational values. Furthermore, the temperature dependence for the rate constants for all eight possible isotopologue reactions and the resulting kinetic isotope effects (KIEs) have been studied. At low temperatures ($\leq$ 100 K), tunneling dominates the reaction rate. The nuclear mass has a high impact on the tunneling probability leading to large kinetic isotope effects (KIEs).

9.2 Computational Details

The different H/D isotopologues are labeled as $H^1H^2OH^3$ such that the reaction reads $H^1H^2 + OH^3 \rightarrow H^1 + H^2OH^3$. DDOH therefore corresponds to a reaction of OH with D_2 while HDOH corresponds to the reaction HD + OH → H + DOH.

For the reaction H_2 + OH → H_2O + H containing protium only (HHOH), the crossover temperature is $T_C = 276.2$ K, while it is 204.2 K for the per-deuterated reaction (DDOD).

All calculations in this chapter were performed using the NN1 PES[258], which was interfaced with DL-FIND.[75] Instantons were optimized starting from the classical transition structure or by starting from an already optimized instanton of similar temperature using the adapted Newton–Raphson algorithm implemented in DL-FIND.[189,190] The convergence criterion for the instanton optimization on the NN1 PES was set to $5 \cdot 10^{-11}$ a.u. for the maximal component of the gradient. Here, mass-weighted coordinates and gradients with the masses in atomic units, *i.e.,* relative to the electron mass, have been used, which influences the convergence criterion.

The OH radical possesses a degenerate electronic ground state. Only one of the electronic states is reactive with respect to the reaction with H_2. This was taken into account in the rate expression.[264,265] Vibrational modes were described by the harmonic approximation around Feynman path. The translational partition function was in all cases approximated by the one of the ideal gas. Rotational partition functions were obtained from classical rigid rotors which is a valid approximation for the temperature region in this part of the study, see section 5.1.1. The symmetry numbers $\sigma_{\mathrm{H}_2} = 2$, $\sigma_{\mathrm{HD}} = 1$, and $\sigma_{\mathrm{D}_2} = 2$ were taken into account.

The full closed Feynman paths were represented by 512 images. Convergence with respect to the number of images was tested at the most severe case with the largest distances between adjacent images, the all-H reaction (HHOH) at 100 K. In this case, the rate constant obtained with 4096 images for the full path deviated by only 0.4 % from the value obtained with 512 images. Smaller deviations can be expected at higher temperature or for heavier isotopologues. Thus, the discretization can be considered to be converged with respect to the number of images.

Below 100 K, the instanton path for HHOH stretches into the pre-reactive minimum with parts of the path below the energy of the separated reactants, see Fig. 9.1. Since this may lead to unphysical results,[129] instanton rates are reported only down to 100 K for H-transfer reactions. For the D-transfer the whole instanton path remains above the reactants' energy for $T > 80$ K. Thus, instanton rates for D-transfer reactions are reported down to 80 K.

The aim of this study is low-temperature rate constants and can therefore not be achieved solely using instanton theory. For this reason, ZCT, SCT, LCT, and μOMT calculations have been performed based on canonical variational transition state theory (CVT)[20,136] by interfacing the NN1 PES[258] with POLYRATE.[266,267] For the LCT calculations, the action integrals (θ integrals) and the sine of the angle between the minimum energy path and the tunneling path were interpolated to 2^{nd} order. The ZCT, SCT, LCT, and μOMT calculations have been carried out down to 80 K in steps of 5 K and an additional rate calculation was performed at 50 K.

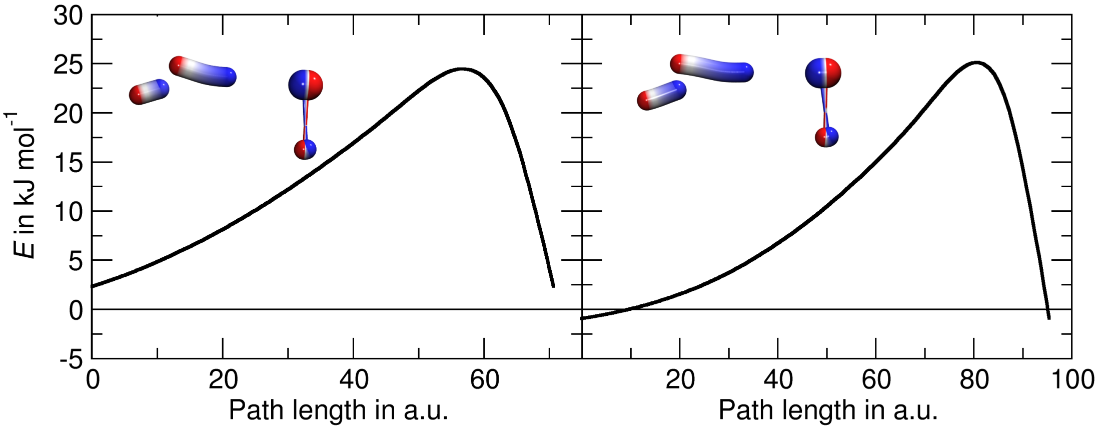

Figure 9.1 Potential energy along the instanton path at 130 K (left) and 80 K (right) relative to the energy of the separated reactants. At 130 K the whole instanton path is above the reactant's energy. At 80 K its ends are below that value. Pictures of the corresponding instantons are inserted. Reprinted with the permission from *J. Chem. Phys.* **144**, 174303 (2016), Copyright (2016) American Institute of Physics.

9.3 Reaction Profile

For bimolecular reactions, it is generally possible that a pre-reactive complex (PRC) can lead to an increase of the reaction rate constant with decreasing temperature. This effect was studied experimentally in the reaction of HBr and OH radicals as well as in the reactions with nitric acid or alcohols and OH radicals.[27,268,269] In these cases, the non-covalent interactions between the two reactants stem from the dipole moments and polarizabilities of the reacting molecules. In contrast to that, H_2 is neither very polarizable nor has a permanent dipole moment. The impact of the PRC is thus expected to be minor compared to the other cases mentioned above unless the temperature is much lower than considered here.

The relevant stationary points on the potential energy surface of the title reaction are depicted in Fig. 9.2. Relative to the separated reactants, H_2 and OH, the potential energy on the NN1 PES is -2.11 kJ mol^{-1} for the PRC, 22.50 kJ mol^{-1} for the transition structure (TS), and -68.08 kJ mol^{-1} for the products (H + H_2O). The imaginary harmonic frequency is 1206i cm^{-1} on the NN1 PES.

The zero-point energy and therefore the vibrationally adiabatic ground state energies of PRC, TS as well as the value of the crossover temperature T_C depend on

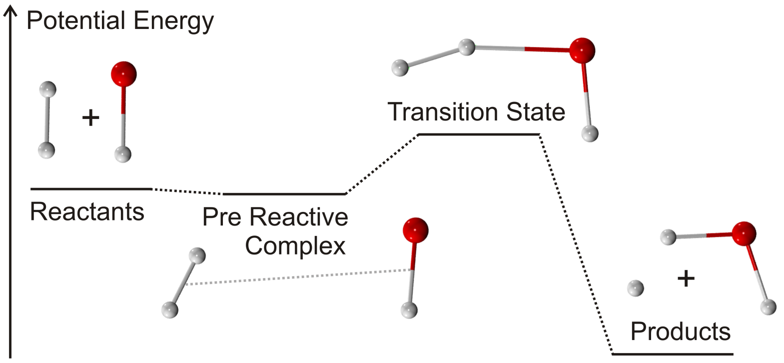

Figure 9.2 Potential energy profile of the reaction H_2 + OH → H_2O + H. Relative to the separated reactants, the pre-reactive complex has a potential energy of −2.1 kJ mol^{-1}, the transition structure 22.5 kJ mol^{-1} and the separated products −68.1 kJ mol^{-1}. Reprinted with the permission from *J. Chem. Phys.* **144**, 174303 (2016), Copyright (2016) American Institute of Physics.

the masses of the nuclei. For reactions with deuterium, the crossover temperature is significantly reduced, see table 9.1. It is barely affected by the deuteration of other hydrogen atoms than the transferred one.

Table 9.1 ZPE corrected energies of the corresponding characteristic points of the PES in kJ mol^{-1} relative to the separated reactants. The crossover temperature T_C is given in K. E_A refers to the activation energy, the energy difference between TS and PRC. For comparison, the values of E_A determined by Nguyen *et al.*, reference 71 is given. Reprinted with the permission from *J. Chem. Phys.* **144**, 174303 (2016), Copyright (2016) American Institute of Physics.

	PRC	TS	E_A	E_A(ref 71)	T_c
HHOH	0.54	24.76	24.22	24.41	276.2
HHOD	0.41	23.50	23.09	23.19	276.1
DHOH	0.30	24.13	23.82	23.74	266.0
DHOD	0.17	22.84	22.67	22.48	265.8
HDOH	0.20	25.86	25.66	25.37	208.9
HDOD	0.04	24.57	24.53	24.12	208.8
DDOH	−0.04	25.65	25.69	25.16	204.3
DDOD	−0.22	24.31	24.53	23.86	204.2

9.4 Reaction Rate Constants

The rate constant of the reaction of H_2 and OH has been measured several times using different techniques, see Fig. 9.3 and the references therein. The Arrhenius plot already shows a noticeable curvature at 300 K and below,[246,248], a clear sign that the reaction is influenced by atom tunneling. Experimental rate constants are available from 1000 K down to 200 K.[69,246–249] The sets of rate constants of the previous studies agree quite well, typically within 20–30%.

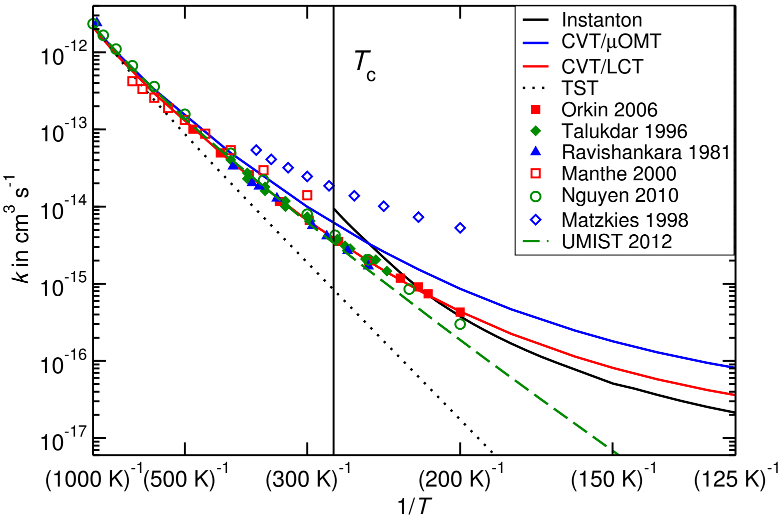

Figure 9.3 Reaction rate constants for HHOH compared to literature data. Experimental data: "■" data from reference 248, "♦" data from reference 69, "▲" data from reference 246; computational data: "□" data from reference 245, "○" data from reference 260, "◇" data from reference 259, and UMIST 2012 values from reference 102. Reprinted with the permission from *J. Chem. Phys.* **144**, 174303 (2016), Copyright (2016) American Institute of Physics.

A large variety of computational studies has been performed of this system. Among them, full-dimensional quantum dynamics calculations on the Schatz–Elgersma PES[252,253] by Matzkies in 1998 and Manthe in 2000[245,259] using the multi-configuration time-dependent Hartree (MCTHD) approach. At $T = 300$ K, the lowest temperature covered by close-coupling calculations employing a rigorously correct statistical sampling scheme for the rotational degrees of freedom,[245] their calculations overestimate the experimental rate constants by about a factor of 2. In an earlier work,[259] they calculated rate constants down to 200 K, which are more than an order of magnitude higher than the experimental value.[248] In general, MCTDH calculations are expected to be rather accurate. In this case, the large deviations of the MCTDH results from the experimental ones can be trace back to the quality of the Schatz–Elgersma PES. This makes it difficult to compare these values with the instanton rate constants presented here. Better agreement with the experimental values was achieved by Nguyen et al.[260] by applying semiclassical transition-state theory (SCTST) on a level of electronic structure theory which is comparable to the one used for the NN1 PES. At 200 K they underestimate the experimental rate constant by a factor of 1.43, which can be assumed to lie within the experimental error bar. They furthermore showed that SCT gives significantly higher reaction rate constants at lower temperatures compared to SCTST calculations.[260]

The rate constants calculated using HTST, LCT, μOMT, and instanton theory, are depicted in Fig. 9.3. For the values of the rate constants calculated using μOMT, and instanton theory, see tables 14.1 to 14.4 in the appendix. As expected[38] instanton theory overestimates the rate constant close to T_C. Agreement is improved at lower temperature. At 220 K the instanton rate constant ($8.9 \cdot 10^{-17}$ cm^3 s^{-1}) is just slightly lower by a factor of 0.98 than the results of flash photolysis resonance-fluorescence by Orkin et al.[248]. At 200 K, the lowest temperature at which comparison is possible, the instanton rate is lower by just 14 %. A high accuracy of instanton theory can be expected at lower temperature[38].

As in this reaction the SCT rate constant is always higher than the one obtained by LCT, the μOMT result is virtually indistinguishable from the SCT results. Therefore no graph for SCT is shown in Fig. 9.3. At temperatures below 300 K, CVT/LCT (and ZCT) agrees well with instanton theory whereas SCT and, thus μOMT, give significantly higher values. At 200 K μOMT overestimates the reaction rate constants by a factor of 2.0, see table 9.2 and Fig. 9.3.

For comparison, Fig. 9.3 includes the rate constant calculated by accounting for the vibrational zero-point energy, but not for tunneling (dotted line labeled as TST). As expected, it describes the rate constant very well at high temperatures (above 400 K) but deviates significantly below that temperature.

Table 9.2 Reaction rate constants k in cm^3 $molecule^{-1}$ s^{-1} at 200 K obtained by different methods. Experimental values are from reference 248. Reprinted with the permission from *J. Chem. Phys.* **144**, 174303 (2016), Copyright (2016) American Institute of Physics.

Method	k
Experimental	$4.3 \cdot 10^{-16}$
Instanton NN1	$3.78 \cdot 10^{-16}$
CVT/μOMT	$8.65 \cdot 10^{-16}$
CVT/SCT	$8.65 \cdot 10^{-16}$
CVT/LCT	$4.38 \cdot 10^{-16}$
CVT/ZCT	$3.50 \cdot 10^{-16}$
CVT	$1.38 \cdot 10^{-17}$
TST	$1.63 \cdot 10^{-17}$

9.5 Kinetic Isotope Effects

All eight possible isotopologues were investigated. Reaction rate constants were calculated using instanton theory and μOMT. The rate constants are shown in Fig. 9.4. Values of the KIEs at 160 K and 100 K (both instanton and μOMT), and 50 K (μOMT) are given in table 9.3. For the values of the reaction rate constants of all isotopologues see tables 14.1 to 14.4 in the appendix.

Down to 160 K the curvature of the resulting Arrhenius plot in Fig. 9.4 is negligible for isotopologues with D-transfer. Defazio et al. already mentioned that tunneling may be of less importance in the DDOH case.[270] This is certainly true in the temperature range where experimental data is available, *i.e.,* above 210 K. At lower temperatures, more precisely below about 100 K, the reactions of all isotopologues are dominated by tunneling. A direct comparison between the instanton calculations and experimental data is impossible for any of the deuterated cases, as no data is available below T_C. Above 50 K a clear primary KIE, *i.e.,* depending on the mass of the atom to be transferred, is measurable.

The KIE can stem from differences in zero-point energies or might be caused by atom tunneling.[9,271,272] One may, of course, question whether the harmonic approximation for zero-point energies is good enough to estimate rate constants at such low temperatures. However, the calculated vibrational adiabatic barriers of

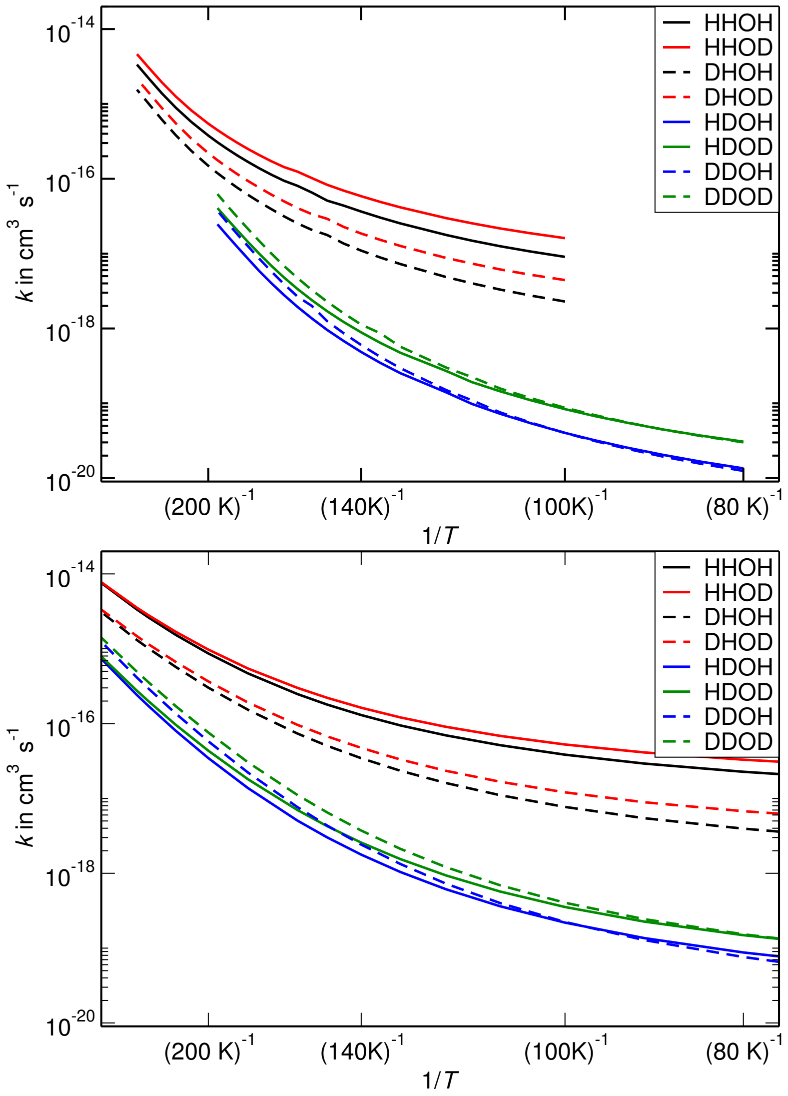

Figure 9.4 Temperature dependence of the reaction rate constants of all H/D isotopologues calculated with the instanton method (above) and with CVT/μOMT (below). Reprinted with the permission from *J. Chem. Phys.* **144**, 174303 (2016), Copyright (2016) American Institute of Physics.

the isotopologues agree well (with a deviation of less than 0.7 kJ mol^{-1}) with the literature values obtained by the more elaborate HEAT protocol,[71] see table 9.1. It was shown previously[71] that including anharmonicity changes the corresponding barrier height by less than 0.33 kJ mol^{-1}.

Table 9.3 Kinetic isotope effects at 150 K, 100 K, and 50 K with respect to HHOH. Reprinted with the permission from *J. Chem. Phys.* **144**, 174303 (2016), Copyright (2016) American Institute of Physics.

	Instanton		μOMT		
Isotopes	160 K	100 K	160 K	100 K	50 K
HHOH	1.00	1.00	1.00	1.00	1.00
DHOH	3.19	3.95	3.37	4.99	6.89
HHOD	0.649	0.561	0.828	0.732	0.610
DHOD	1.99	2.04	2.58	3.19	3.42
HDOH	41.5	224	49.1	176	382
DDOH	30.2	225	32.4	172	558
HDOD	23.9	108	35.4	109	216
DDOD	17.1	104	22.3	95.3	229

Apart from the primary KIE, secondary KIEs are observed. The deuteration of the hydroxy radical (OD) increases the reaction rate, leading to inverse KIEs. Depending on the deuteration of the other sites, OD increases the rates by factors of 1–3, see table 9.3. The main reason for this effect is that the heavier deuterium atom lowers E_A of the transition state by reducing the zero-point energy of the deformation modes of the two molecules with respect to each other.

The reaction rate constants obtained with CVT/μOMT are higher than the ones obtained with instanton theory by a factor of 4.2 for HHOH and 5.4 for HDOH at 100 K. It is obvious from Fig. 9.3 and table 9.2 that CVT/μOMT generally overestimates the reaction rate constants for this reaction. Apart from that, the rate constants seem to follow the same trends, in particular the KIEs obtained by both methods agree reasonably well, see table 9.3.

Instanton theory provides a dominant tunneling path for each specific temperature. At low temperature, that path is almost temperature-independent. The atoms contribute quite differently to that tunneling path. Geometries and the energy along the instanton path are depicted in Fig. 9.1. In the low-temperature limit for HHOH, the hydrogen atom to be transferred is delocalized over 1.34 Å, the hydrogen atom hat remains isolated after the reaction is delocalized over 0.80 Å. Both oxygen and hydrogen of OH contribute to the tunneling a lot less, they are delocalized over 0.14 and 0.21 Å, respectively. Deuteration changes these contributions: for HDOH, the transferred deuterium is delocalized over only 1.25 Å while the other tunneling path length remain almost unchanged (0.77, 0.15, and 0.21 Å).

Primary H/D-KIEs of > 200 at 50 K have been found using CVT/μOMT. At even lower temperature than reported here, the KIE can be expected to be at least similarly strong. Consequently, a significant influence of this reaction and its KIE on the deuterium fractionation of molecules in the interstellar medium is expected.

9.6 Summary

Reaction rate constants of the reaction $H_2 + OH \rightarrow H + H_2O$ have been calculated down to 100 K using instanton theory and down to 50 K using CVT/μOMT on the NN1 PES[258] for all H/D isotopologues. Atom tunneling sets in at about 250 K for H-transfer and at about 200 K for D-transfer. A significant primary H/D KIE of about 200 is found at 100 K and of 300–600 at 50 K. Secondary effects, some of them inverse due to vibrational zero-point energy, are smaller and negligible in this case. The reaction rate constants at these temperatures are significantly higher than the ones implemented in the UMIST data base.[102]

At 80–50 K the reaction rate constants of the H-transfer become almost temperature-independent due to atom tunneling. The presented results clearly indicate that the reaction is relevant for processes in the interstellar medium at even lower temperatures, even when deuterium is transferred instead of protium.

10 H_2 + OH → H_2O + H on an Ice Surface

10.1 Introduction

As discussed in section 1.2, the reaction

$$H_2 + OH \rightarrow H_2O + H \tag{R 8}$$

is supposed to be one of the main reactions transforming OH radicals to interstellar water. It was experimentally found that reaction (R 8) takes place at the cryogenic temperature of 10 K due to quantum mechanical tunneling of atoms.[65] even though the gas phase reaction exhibits a barrier of 17.5 kJ mol^{-1}.[70]

This part of the thesis is structured as follows: First, a benchmark was performed to find a suitable electronic potential by comparing the quality with highly correlated calculations on UCCSD(T)-F12 level.[207,208] Furthermore, the water ice surface and the organization of the QM/MM setup, as well as the computational details of the reaction rate calculations are described. After that, different binding sites and binding energies of the OH radical on the ice surface as well as accompanying activation energies, transition structures, and IRCs are shown. Reaction rate constants for the Eley–Rideal and the Langmuir–Hinshelwood mechanisms were given using semiclassical instanton theory to include multidimensional atom tunneling. The results are compared to those in the gas phase and the impact of

---

[*] **Parts of this Chapter have been used in:**
Atom Tunneling in the Water Formation Reaction H_2 + OH → H_2O + H on an Ice Surface, Jan Meisner, Thanja Lamberts, and Johannes Kästner *ACS Earth Space Chem* **1**, 399–410 (2017), see reference 76 and the content is adapted with permissions. Copyright 2017 Americal Chemical Society.

surfaces on the reactivity is discussed. Kinetic isotope effects for all eight possible permutations of exchanging hydrogen for deuterium are shown as well. The last section discusses the implications to astrochemistry, gives fits of the rate constants to a modified Arrhenius equation, and concludes the chapter.

10.2 Computational Details

10.2.1 Choice of the Electronic Potential

In order to obtain reliable reaction rate constants, the method to calculate the underlying electronic potential has to be as accurate as possible. Instanton calculations using highly correlated wave function methods are too time consuming, so density functional theory (DFT) was applied to describe the QM part of this part of the thesis. For this purpose, an extensive benchmark of the most common functionals and basis sets has been performed, which be seen in the appendix. The BHLYP functional[217,218,220,221,234] in combination with the def2-SVPD basis set[273] was found to describe the reaction well. It has also previously been found to describe astrochemical reactions with open-shell molecules properly.[274,275] Thus BHLYP is used in the remainder of this chapter.

To include the environment, *i.e.*, the water surface, a QM/MM framework was used applying the ChemShell interface.[205,206] The QM part can be polarized by means of electrostatic embedding into the MM charges. All geometry optimizations and reaction rate calculations were done with DL-FIND.[75] The visualization of the molecules and ice surface was done using Visual Molecules Dynamics (VMD).[276]

10.2.2 Surface Model and QM/MM setup

The (0001) surface of hexagonal ice I_h minimizing the surface free energy, as described by Fletcher,[277] was used, where the hydrogen atoms are ordered. The structure of the bare surface can be seen in Fig. 10.1 The majority of solid water in the interstellar medium is expected to be amorphous. Nevertheless, the conclusions obtained by using a crystalline surface can be generalized to amorphous water ice or small water clusters for this particular reaction.

The structural model consisted of a hemisphere with a radius of 25 Å comprised of 1151 water molecules. The MM part was described by the TIP3P potential.[278] For the QM part, five adjoining water hexagons of the top layer were used: 19 water molecules and the adsorbed atoms. Geometry optimizations included all

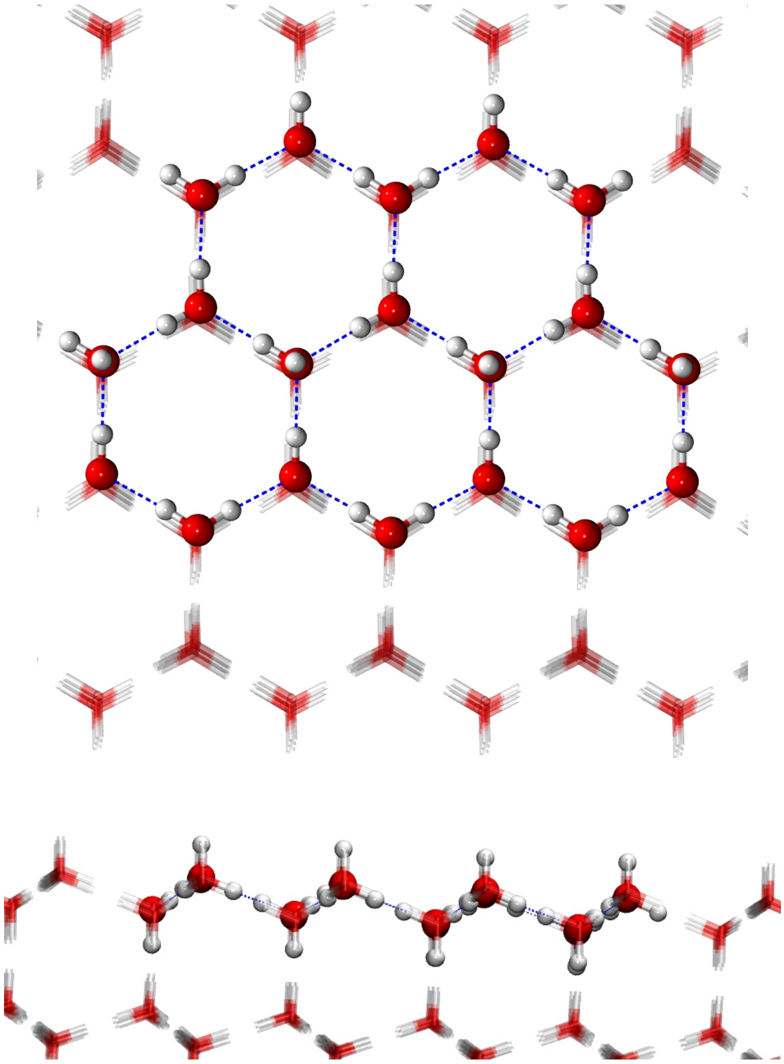

Figure 10.1 QM/MM setup of the Fletcher surface.[277] The solid ball-and-stick-molecules represent the QM region while the transparent ones represent the MM region. All MM water molecules within a radius of 15 Å are allowed to move and rotate. Reprinted with the permission from *ACS Earth Space Chem* **1**, 399–410 (2017). Copyright (2017) American Chemical Society.

water molecules within a radius of 15 Å around the center of the hemisphere (261 molecules) as active atoms, the other H_2O molecules were frozen. All in all, 2349 variables are to be optimized for the bare surface. For the calculations of IRCs, a step size of 0.05 mass-weighted atomic units was used. Instantons and the corresponding Hessians have been calculated with a reduced dimension: here, only the adsorbed atoms/molecules and the hexagon of the six closest water molecules were flexible.

The instanton rate calculations are computationally very demanding. Therefore, the implicit surface model was used to obtain rate constants of the eight possible H/D isotopologues.

10.2.3 Reaction Rate Calculations and Tunneling

To calculate reaction rate constants including atom tunneling, instanton theory was used. Vibrational modes are included harmonically around the Feynman path. The rotational partition functions of the reactants and the images of the instantons were approximated by those of rigid rotors. The translational partition function was included within the approximation of an ideal gas. Rotational partition functions were obtained from classical rigid rotors and the rotational partition function of the whole instanton was calculated to be the geometric mean value of the rotational partition functions of all images. The symmetry number $\sigma_{\mathrm{H}_2} = \sigma_{\mathrm{D}_2} = 2$ was taken into account when calculating the rotational partition function of the H_2 and D_2 molecules for bimolecular reaction rates.[136] For the reactions with HD and for unimolecular reaction rates in general, $\sigma = 1$ was used, because the rotation of adsorbed molecular hydrogen is hindered by the surface.

For the reaction on the Fletcher surface, the closed Feynman path was discretized with 40 images down to 175 K and with 78 images down to 80 K. For the instanton calculations using the implicit surface model, (of all isotopologues), 200 images were used for the whole temperature range. Instantons were considered to be converged when all components of the nuclear gradient were smaller than $1 \cdot 10^{-8}$ a.u.. Instanton calculations were performed at temperatures below the crossover temperature of 280 K ± 5 K (depending on the binding site). Because of the existence of a pre-reactive minimum, below a particular, mass-dependent tem-

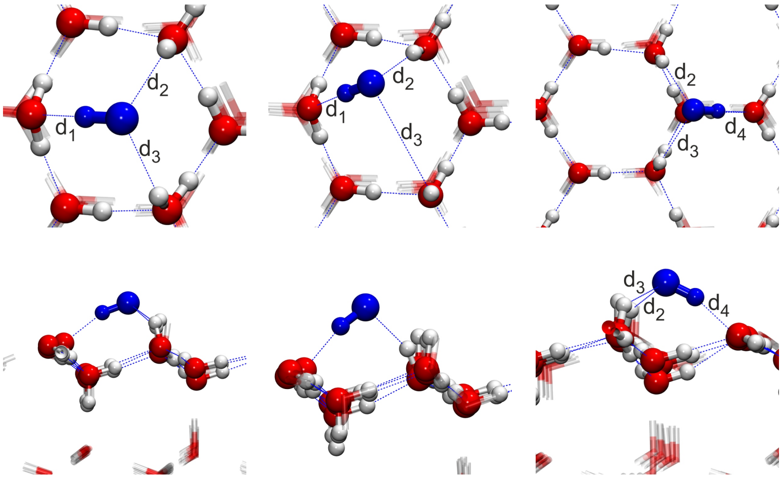

Figure 10.2 Structures of the adsorbed OH radical (blue) on the Fletcher surface. All binding sited are shown from top and side perspectives. Left: *Hollow*, Middle: *Bridged*, Right: *Top*. Reprinted with the permission from *ACS Earth Space Chem* **1**, 399–410 (2017). Copyright (2017) American Chemical Society.

perature, the tunneling energy is lower than the potential energy of the separated products for bimolecular reaction rates. At that temperature, canonical instanton theory becomes unreliable.[129] Therefore, bimolecular reaction rates can only be provided for 110 K and higher temperatures for the reaction H_2 + OH → H + H_2O.

10.3 Binding Sites and Energies

Three different binding sites of OH on the Fletcher surface could be identified, which are shown in Fig. 10.2. The corresponding adsorption energies with and without harmonically approximated vibrational zero-point energies have been calculated, see table 10.1. For all binding sites, zero-point energy reduces the binding energy by around 16 kJ mol^{-1} because the OH–surface complex has additional vibrational modes. The harmonic approximation can be assumed to overestimate the zero-point energy, which leads to an underestimation of the corresponding adsorbtion energy.

Table 10.1 Adsorption energies of OH on the Fletcher surface and hydrogen bond distances. V_{ads} and E_{ads} denote the adsorbtion energy without and with zero point energy, respectively. The hydrogen-bond lengths d_1 to d_4 are explained in Fig. 10.2. Energies are given in kJ mol^{-1}, distances in Å. Reprinted with the permission from *ACS Earth Space Chem* **1**, 399–410 (2017). Copyright (2017) American Chemical Society.

	V_{ads}	E_{ads}	d_1	d_2	d_3	d_4
Hollow	57.0	40.5	1.77	2.22	2.27	
Bridged	55.6	39.7	1.77	1.99	3.89	
Top	48.1	32.1		2.11	2.36	1.78

In the first binding site, the OH radical is located directly in the middle of a water hexamer where it accepts hydrogen bonds from two of the dangling hydrogen atoms and donates a hydrogen bond to the O atom of a water molecule of the surface. This binding site will be called *hollow*. The binding energy is 40.5 kJ mol^{-1} including zero-point energy.

In a similar binding site the OH radical is also hydrogen-bound to the oxygen atom of a water molecule and to one dangling hydrogen atom of the surface, see Fig. 10.2. The third hydrogen bond is absent, *i.e.*, the OH radical bridges two surface water molecules. This binding site is called *bridged*. As this binding site is rather similar to the *hollow* one, the binding energy is only slightly smaller with 39.7 kJ mol^{-1}.

In the third binding site the OH radical is located on top of one of the water molecules. Because of that, this binding site will be called *top*. The OH radical also accepts two hydrogen bonds from the surface and donates one. The binding energy of this site is with 32.1 kJ mol^{-1} lower than for the *hollow* and *bridged* binding sites. These values are nicely in the range of experimentally determined desorption energies on silicate surfaces of 1656–4760 K (13.8–39.6 kJ mol^{-1}).[279]

10.4 Reaction Barriers

One possibility for the reaction of the OH radical with molecular hydrogen on the ice surface is the Eley–Rideal (ER) mechanism, in which one species is adsorbed on the surface and the other one is approaching from the gas phase, see section 4.1.

Table 10.2 Reaction barriers including zero-point energies and geometric parameters of the transition structures. The label *bi* denotes that the barrier is given with respect to the separated reactants, *i.e.*, $OH_{(ads)}$ and $H_{2(g)}$. The label *uni* indicates barriers with respect to the respective pre-reactive complexes. The O–H distance of the newly formed bond, the H–H distance of the original H_2 molecule, and the H–O–H angle of the newly formed water molecule are denoted by $d_{\text{O–H}}$, $d_{\text{H–H}}$, and $\measuredangle$(H–O–H), respectively. All values are in kJ mol^{-1}, all distances in Å, and $\measuredangle$(H–O–H) in degrees. Reprinted with the permission from *ACS Earth Space Chem* **1**, 399–410 (2017). Copyright (2017) American Chemical Society.

	Hollow	Bridged	Top	Gas Phase
$E_{A,\text{bi}}^{\text{direct}}$	24.2	24.7	24.3	25.4
$E_{A,\text{bi}}^{\text{rotated}}$	49.3		45.7	
$E_{A,\text{uni}}^{\text{direct}}$	22.5	24.1	22.4	24.4
$d_{\text{O–H}}$	1.33	1.33	1.33	1.36
$d_{\text{H–H}}$	0.83	0.83	0.84	0.82
$\measuredangle$(H–O–H)	99.2	99.7	98.7	96.8

The binding energy of OH radicals is much higher than the binding energy of H_2 molecules (3.6–4.6 kJ mol^{-1}; 440–555 K).[119] Therefore, the reaction of adsorbed OH radicals with H_2 molecules directly from the gas phase is investigated here:

$$OH_{\text{ads}} + H_{2(g)} \rightarrow H_2O + H. \qquad \text{(R 17)}$$

For the products the label indicating the aggregate state was omitted, as this work focuses on the chemical reaction forming H_2O molecules and the physical processes after that are not treated here. For each binding site of OH one corresponding transition structure was found. These transition structures are called *direct* hereinafter, and the transition structure of the direct-hollow binding site can be seen in Fig. 10.3. The vibrational adiabatic reaction barriers with respect to the separated reactants (potential energy barriers including zero-point energy) of these

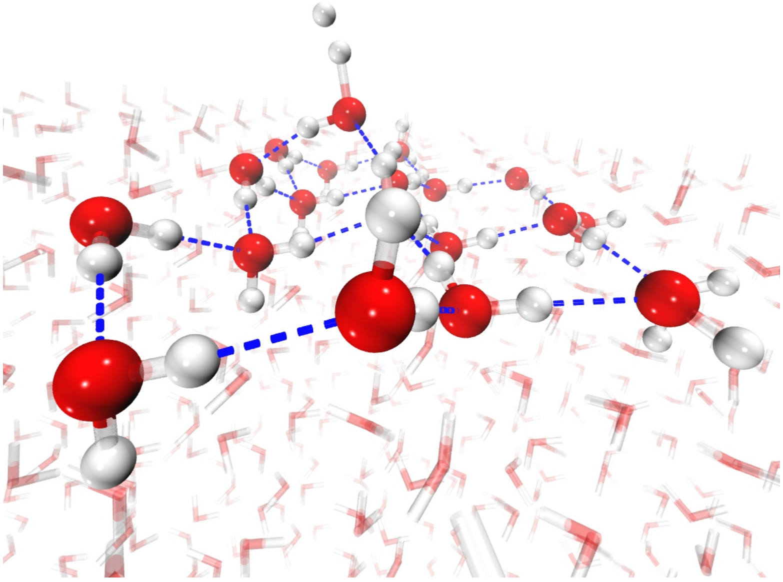

Figure 10.3 Transition structure of the *direct-hollow* binding site. QM atoms are shown as balls and sticks, MM atoms as transparent sticks. Reprinted with the permission from *ACS Earth Space Chem* **1**, 399–410 (2017). Copyright (2017) American Chemical Society.

transition structures lie between 24.2 and 24.7 kJ mol^{-1}, see table 10.2. This is just slightly lower than the adiabatic reaction barrier of the gas phase reaction of 25.4 kJ mol^{-1} (from separated reactants). Here it should be emphasized that all reaction barriers are very similar, independently of the corresponding adsorbtion energies, although the latter vary over 8 kJ mol^{-1}. This is in agreement with what is found for reactions on amorphous solid water.[180]

Another type of transition structures was found, in which the hydrogen atom of the OH radical points away from the surface and the H_2 molecule approaches *via* a path closer to the surface. The $[OH\cdots H_2]$ complex possesses similar internal coordinates as in the *direct* transition structures, but is rotated with respect to the ice surface, see Fig. 10.4. For these *rotated* transition structures, the adiabatic reaction barriers are 49.3 and 45.7 kJ mol^{-1} for the *hollow* and the *top* binding site, respectively. The transition structure of the rotated-hollow binding site is shown in Fig. 10.4. No *rotated* transition structure was found for the *bridged* binding site. The barriers via *rotated* transition structures are much higher than those via the *direct* transition structures, which can be seen in Fig. 15.2 in the appendix. For this reason, it is expected that the *rotated* transition structures result in much lower rates and from here, just the *direct* transition structures are considered further.

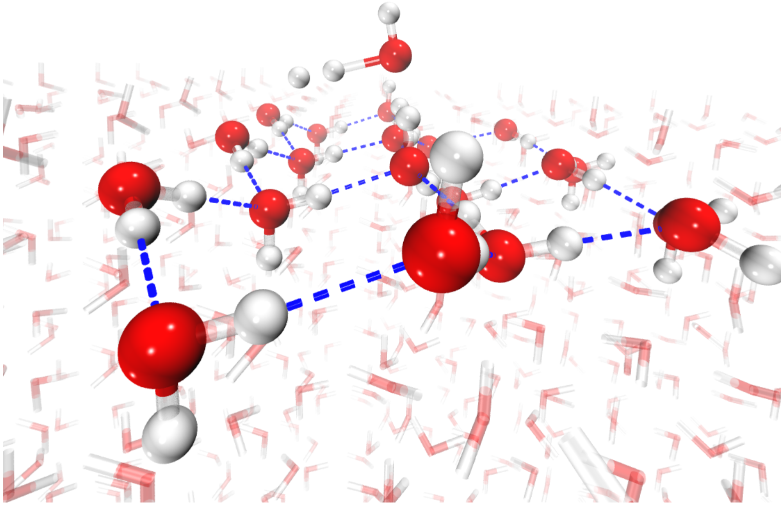

Figure 10.4 Transition structure of the *rotated-hollow* binding site. QM atoms are shown as balls and sticks, MM atoms as transparent sticks.

The potential energy along the IRCs of the different binding sites has been calculated, see Fig. 10.5. The ends of the IRCs define pre-reactive complexes (PRCs). Those are geometries in which an H_2 molecule is loosely bound to the surface in the vicinity of the OH radical. These structures are used as reactant structures to calculate the unimolecular activation energies shown in table 10.2.

The potential energy curves along the IRCs belonging to the different binding sites are almost indistinguishable from the one of the gas-phase reaction, see

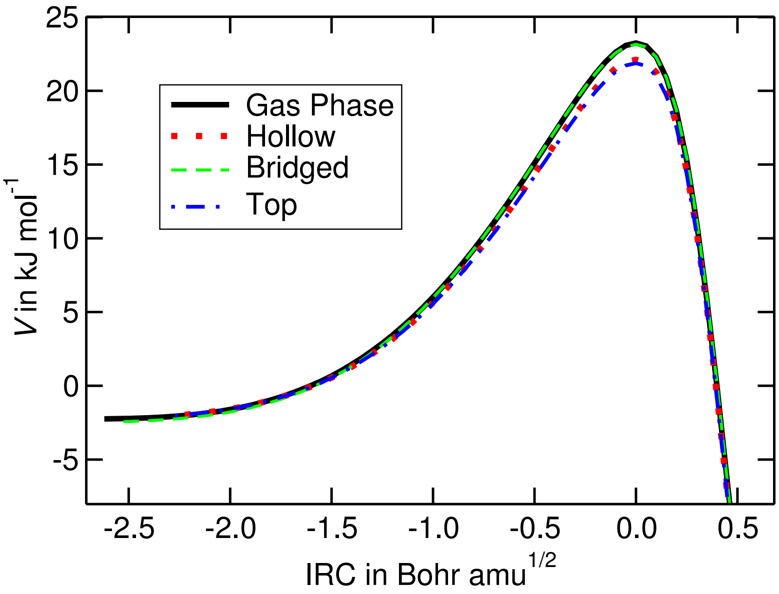

Figure 10.5 Potential energy V of the intrinsic reaction coordinates (IRCs) of the *hollow*, *top*, and the *bridged* binding site compared with the gas-phase reaction. Reprinted with the permission from *ACS Earth Space Chem* **1**, 399–410 (2017). Copyright (2017) American Chemical Society.

Fig. 10.5. This shows again that the surface has negligible influence on the potential energy along the reaction path. During the reaction, any changes in the hydrogen bond length remain below 0.2 Å, see Fig. 10.6. Overall, a classical catalytic effect is minimal: the activation barrier is almost unaltered and the reaction mechanism is unchanged. This can be explained by the adsorption energy during the reaction. In typical heterogeneous catalysis the molecules are activated through interactions with the surface in a way that the energy of the transition structures with respect to the energy of the reactant structure is reduced. These interactions are either forming new chemical bonds or causing a shift in electron density. In the case discussed here, the OH radical forms three hydrogen bonds in the adsorption process and these three hydrogen bonds are retained during the whole reaction. Therefore, the adsorption energies of the reactant structure and the transition structure are virtually the same and the potential energy of the reaction remains comparable to the gas phase. Reaction with an OH radical bound via four hydrogen bonds is impossible due to steric hindrance. Therefore, the maximal

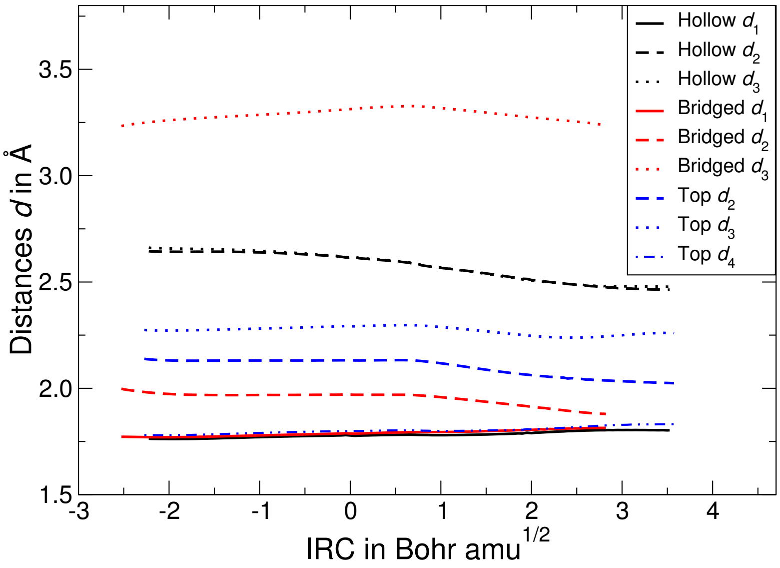

Figure 10.6 The black, red, blue curves correspond to the change in the O–H hydrogen bond lengths during the reaction in the *hollow*, *bridged*, and *top* binding site, respectively. The labeling follows that of Fig. 10.2. Reprinted with the permission from *ACS Earth Space Chem* **1**, 399–410 (2017). Copyright (2017) American Chemical Society.

number of hydrogen bonds to a reactive OH is always three, independent of the existence of *e.g.* cavities for surface defects. It can, therefore, be assumed that amorphous solid water ices behave similarly in terms of negligible catalytic effects.

Note, that any processes after the formation of the chemical bonds, like desorption or dissipation, are not covered in this thesis because they they do not influence the rate. The kinetic bottleneck in the water formation from H_2 molecules and OH radicals is the H–H bond breaking which is described here.

10.5 Reaction Rate Constants for the Eley–Rideal Mechanism

In the Eley–Rideal (ER) mechanism, one particle (a molecule or an atom) physisorbs on the surface and thermalizes there. Another particle impinges from the gas phase and directly reacts with the pre-adsorbed particle to form the products. This study focuses on reaction (R 17) where an OH radical is adsorbed and the

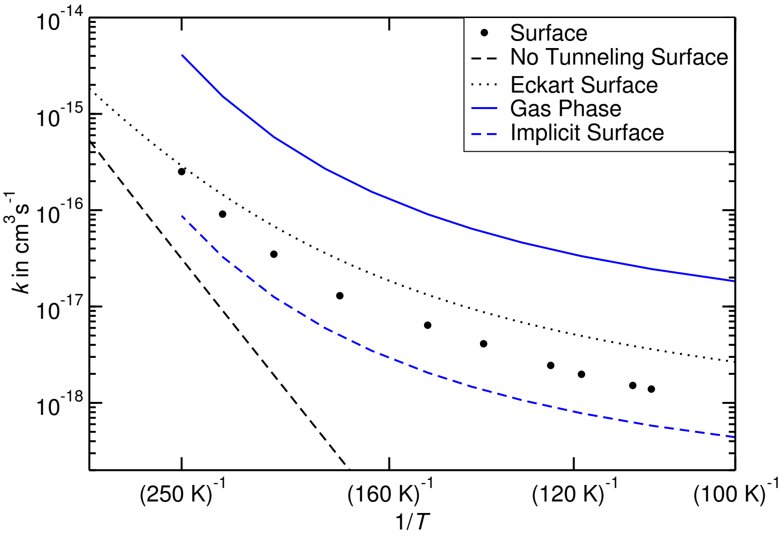

Figure 10.7 Arrhenius plot of the bimolecular (Eley–Rideal) reaction rate constants. Instanton theory is used if not stated otherwise. Surface reaction rates are calculated for the *direct-hollow* reaction path. Reprinted with the permission from *ACS Earth Space Chem* **1**, 399–410 (2017). Copyright (2017) American Chemical Society.

H_2 molecule comes in from the gas phase, since OH has a higher adsorption energy. The incoming H_2 molecule reacts with the OH-surface system in what can formally be seen as a bimolecular reaction. Instantons were calculated from 250 K to 110 K. For comparison, reaction rate constants using the approximation of an Eckart-shaped barrier have also been calculated.

As the reaction profiles of all three *direct* transition structures and IRCs are nearly identical, only reaction rate constants of the *direct-hollow* transition structure have been calculated. Due to high computational costs the active region for the instanton calculations was reduced to the one water hexamer below the adsorbed OH radical. The resulting adiabatic activation energy of 24.11 kJ mol^{-1} is almost equal to the 24.19 kJ mol^{-1} obtained for the full active region.

The resulting reaction rate constants are compared to the gas-phase data calculated on the same potential energy surface in the Arrhenius plot in Fig. 10.7. The rate constants including tunneling correction via the Eckart barrier and those obtained by transition state theory without tunneling are shown for comparison. The implicit surface model is able to reproduce the rate constants of the explicit surface calculations up to factors of 3.6 and 2.7 at 275 K and and 110 K, respectively. This indicates that for reactions without a classical catalytic effect, the implicit surface model is a promising approximation. Numeric values for the rate constants are available in the appendix in table 15.3.

10.6 Reaction Rate Constants for the Langmuir–Hinshelwood Mechanism

In the Langmuir–Hinshelwood (LH) mechanism, both particles are adsorbed on the surface and diffuse until they meet. If they approach each other, they form a PRC. This PRC can either react or decay by diffusion or desorption of one or both reactants. The reaction of a PRC to the products is a unimolecular process. Thus, Langmuir–Hinshelwood reactions are characterized by unimolecular rate constants. These unimolecular reaction rate constants are calculated for the *hollow* binding site.

The adiabatic activation barriers for the LH mechanism in all binding sites are given as $E_{A,\mathrm{uni}}^{\mathrm{direct}}$ in table 10.2. The resulting unimolecular rate constants k_{react} are shown in Fig. 10.8 and in table 15.4 in the appendix. Instantons were calculated down to 80 K. At even lower temperatures, more images would be required to obtain converged reaction rate constants which would render the computations too expensive.

The rate constants from the implicit surface model agree within one order of magnitude with those from the full ice surface model, see Fig. 10.8. The results of the standard gas-phase model and the (gas-phase) calculations using the implicit surface model are closer for the unimolecular reaction than for the bimolecular calculations. The reason for that is that in the unimolecular case, the implicit surface model merely assumes that the rotational partition function of the PRC is the same as the one of the transition structure (*e.g.* that both do not rotate), while their rotation is taken into account in the gas phase. As both PRC and transition structure have similar rotational partition functions (they include the same atoms), the neglect of this term is of minor importance. In the bimolecular case, the implicit surface model removes translation and rotation of one reactant (OH) and

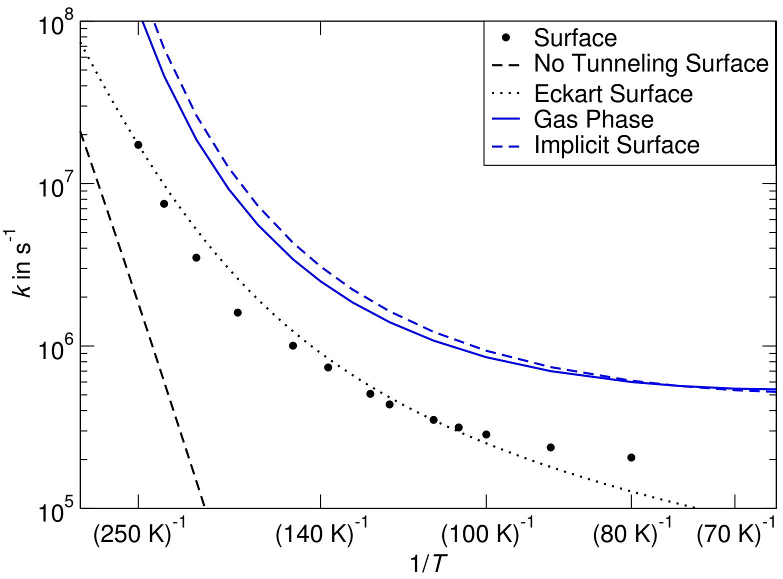

Figure 10.8 Arrhenius plot of the unimolecular Reaction rate constants. Surface reaction rates were calculated around the direct-hollow reaction pathway. Reprinted with the permission from *ACS Earth Space Chem* **1**, 399–410 (2017). Copyright (2017) American Chemical Society.

the transition state, which is a much larger alteration of the rate constant. Note, that due to the inhibited rotation of the H_2 molecule in the PRC the symmetry number $\sigma = 1$ was used for the explicit and implicit surface calculations.

10.7 Kinetic Isotope Effects

The implicit surface model was used to calculate kinetic isotope effects (KIEs) for all eight possible deuteration patterns. Bimolecular and unimolecular reaction rate constants are shown in Fig. 10.9 and Fig. 10.10, respectively. When substituting protium atoms with deuterium atoms, the crossover temperature reduces significantly as a result of a smaller imaginary frequency and, therefore, a smaller crossover temperature. Thus, the rate constants are reported here for 200 K and below. For bimolecular reaction rates, the temperature below which the tunneling energy is lower than the potential energy of the asymptotic reactants changes with the mass, too. Here and in Fig. 10.9 and Fig. 10.10 the isotope patterns are labeled $H^1H^2OH^3$ as previously defined, so that the reaction reads $H^1H^2 + OH^3 \rightarrow H^1 + H^2OH^3$. DDOH therefore corresponds to a reaction of OH with D_2 while HDOH corresponds to the reaction HD + OH → H + DOH.

Table 10.3 Obtained parameters as described by equation (4.9) for the bimolecular reaction rate constants (above) and the unimolecular rate constants (below). Reprinted with the permission from *ACS Earth Space Chem* **1**, 399–410 (2017). Copyright (2017) American Chemical Society.

Bimol.	HHOH	HHOD	DHOH	DHOD
$A[\mathrm{cm^3 s^{-1}}]$	$6.91{\cdot}10^{-14}$	$8.96{\cdot}10^{-14}$	$1.82{\cdot}10^{-14}$	$2.29{\cdot}10^{-14}$
γ[K]	1430.0	1373.0	1449.8	1372.1
T_0 [K]	147.7	151.8	142.7	143.4
Bimol.	HDOH	HDOD	DDOH	DDOD
$A[\mathrm{cm^3 s^{-1}}]$	$1.99{\cdot}10^{-14}$	$2.41{\cdot}10^{-14}$	$2.27{\cdot}10^{-14}$	$2.81{\cdot}10^{-14}$
γ[K]	1749.8	1655.6	1794.0	1701.4
T_0[K]	123.5	123.7	122.6	123.4
Unimol.	HHOH	HHOD	DHOH	DHOD
$A[\mathrm{s^{-1}}]$	$7.64{\cdot}10^{10}$	$4.77{\cdot}10^{10}$	$6.82{\cdot}10^{10}$	$4.36{\cdot}10^{10}$
γ [K]	1339.9	1247.9	1351.6	1265.7
T_0[K]	153.2	145.2	141.0	134.1
Unimol.	HDOH	HDOD	DDOH	DDOD
$A[\mathrm{s^{-1}}]$	$7.90{\cdot}10^{10}$	$4.91{\cdot}10^{10}$	$7.06{\cdot}10^{10}$	$4.45{\cdot}10^{10}$
γ[K]	1674.0	1579.1	1704.2	1611.8
T_0[K]	122.4	117.6	116.3	111.9

In both the bimolecular and unimolecular cases, the primary KIE is as large as two orders of magnitude, but also depends on the isotope pattern of the other two hydrogen atoms. For the bimolecular case, the KIEs are similar to the ones reported in the gas phase in section 9. Here, the secondary KIEs again play a smaller role. In all cases, secondary KIEs are smaller than 10. Like in the gas phase study, an inverse KIE occurs when substituting OH by OD. This small inverse secondary KIE of about 2–3 is caused by differences in the zero-point energy.[1,9,271,272] In the unimolecular case, the primary KIEs are ≈ 5 at 200 K and increase to ≈ 300 at 60 K. The secondary KIEs play an even smaller role than in the bimolecular case and no inverse KIE is present, see Fig. 10.10.

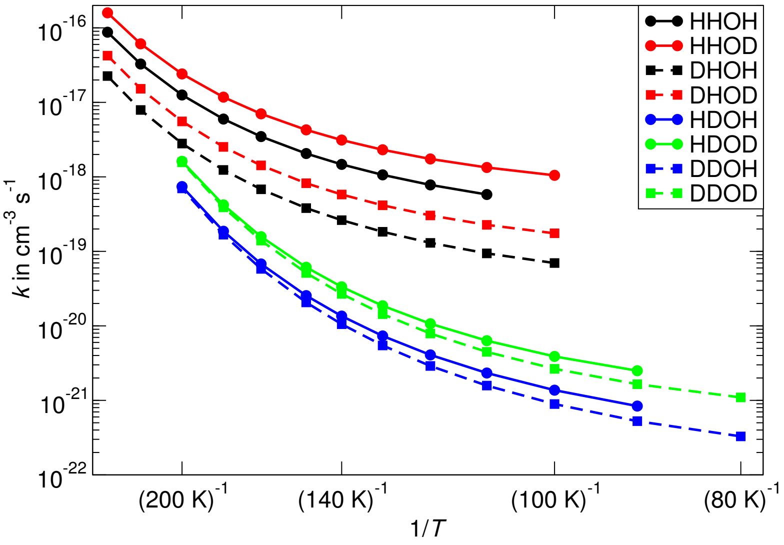

Figure 10.9 Temperature dependence of the (bimolecular) Eley–Rideal reaction rate constants of all H/D isotopologues calculated with the instanton method and the implicit surface approximation. Reprinted with the permission from *ACS Earth Space Chem* **1**, 399–410 (2017). Copyright (2017) American Chemical Society.

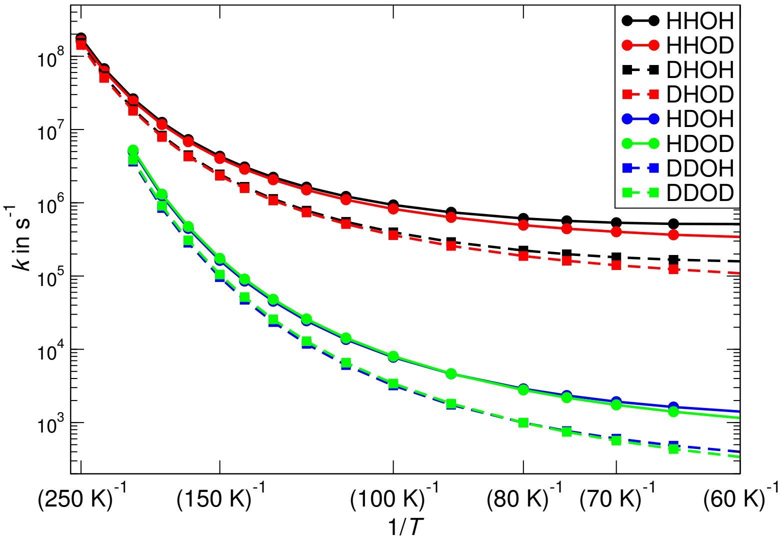

Figure 10.10 Temperature dependence of the unimolecular rate constants of all H/D isotopologues. which can be used to calculate R_{LH} calculated with the instanton method and the implicit surface approximation. Reprinted with the permission from *ACS Earth Space Chem* **1**, 399–410 (2017). Copyright (2017) American Chemical Society.

10.8 Summary

In this chapter, chemical reaction rate constants of the reaction of hydroxyl radicals with molecular hydrogen on an I_h ice surface have been presented. For this purpose, instanton theory on a thoroughly benchmarked QM/MM potential energy surfaces was used. Reaction rate constants from 275 K down to 110 K for the ER mechanism (bimolecular) and down to 60 K for the LH mechanism (unimolecular) have been calculated. For both mechanisms, a fit of parameters to equation (4.9), was performed to obtain a continuous expression of $k(T)$.

To summarize the most important results:

- For the reaction of H_2 and OH radicals, an ice surface just barely influences the potential energy along the reaction path, *i.e.*, there is no classical catalytic effect. The most important transition structures and reaction paths are comparable to the ones in the gas phase. It follows that the adiabatic energy barriers (24–25 kJ mol^{-1}) are similar to the barrier of the gas phase reaction (25.4 kJ mol^{-1}).

- Due to the absence of a classical catalytic effect, the implicit surface model is used to successfully mimic the surface reactions. The reaction rate constants obtained in this way differ at most by a factor of 9.3 from the ones calculated on a full ice surface model.

- Three different binding sites on the I_h surface have been found. Their binding energies lie between 32 and 41 kJ mol^{-1}.

- Kinetic isotope effects have been calculated for all possible isotope substitution patterns. Exchanging the H to be transferred to D leads to a decrease in the rate constant of 2–3 orders of magnitude. Secondary KIEs are at most half an order of magnitude.

11 Conclusion

The understanding of the chemical reaction mechanism, *i.e.,* the dissection of a chemical process into several elementary reactions, is crucial for the understanding of chemical reactivity. In the last decades, computations based on quantum mechanical or (semi-) empirical methods have increasingly been used to elucidate reaction mechanisms. In this context, it can be understood as the connection of the reactant structure and the product structure of the potential energy hyper surface.

An essential part of a computational study is therefore the determination of the path of least potential energy connecting two minimum structures. The minimum energy path in mass-weighted Cartesian coordinates is called intrinsic reaction coordinate (IRC). In this thesis, a new Hessian-based predictor-corrector algorithm was implemented into the DL-Find optimization library[75] based on an existing algorithm.[74,96] The modified algorithm avoids matrix diagonalization and therefore scales with less than $\mathcal{O}(N^3)$, N being the number of atoms, and is suitable for IRC calculations of large systems. Throughout the whole thesis, all reaction paths were calculated using the newly implemented IRC optimizer.

The rate constant of a chemical reaction depends on the mechanism, *i.e.,* the elementary reaction steps, and the corresponding barrier heights. A classical particle can overcome the barrier only if it possesses sufficient kinetic energy, otherwise, it will be reflected. In quantum mechanics, however, objects can tunnel through a potential energy barrier due to the wave nature of a quantum object. The tunnel effect is mass-dependent, and therefore essential to include when describing the motion of light particles such as electrons. Light atoms, such as hydrogen, that can tunnel through potential energy barriers, enhancing chemical reactivity. This mainly concerns proton or hydrogen atom transfer reactions, but heavy elements have also been observed to be involved in the tunnel process. Reactions where atom tunneling is important show a curved Arrhenius plot and the rate constant is temperature independent at very low temperatures for exothermic reactions. The mass-dependence of the tunnel effect leads to strong kinetic isotope effects (KIEs), which is the ratio of the rate of the light isotopologue divided by the rate of the heavier one. The KIE is a sensitive experimentally accessible probe for tunneling and therefore of fundamental interest.

In chapter 5 to 6 different methods to calculate reaction rate constants including atom tunneling are described, ranging from transition state theory to semiclassical instanton theory. In semiclassical instanton theory, the most likely tunneling path, the instanton, is optimized for each temperature. The instanton is a first order saddle point of the Euclidean action. Instanton theory, which is based on Feynman path integrals, provides an accurate and robust tool to calculate rate constants for chemical reactions and is capable of including several dozens of atoms. However, the most computationally expensive steps, the instanton optimization, which need a large amount of energy and gradient evaluations, and the calculation of second derivatives of the potential energy along the path, restrict the availability of the instanton method.

In this thesis, a dual-level instanton approach is presented, where exactly those computational bottlenecks are avoided using a computationally efficient potential. Subsequently, a more accurate electronic structure method is applied to recalculate the potential energy along the tunneling path and at the reactant structure. The accuracy of this approach is tested on three different chemical reactions: the unimolecular rearrangement reaction of HNC to HCN, a sigmatropic hydride transfer reaction and the bimolecular hydrogen atom transfer of hydrogen molecules and NH_2 forming ammonia and H atoms. In all of these three cases, the dual-level method corrects the error of the basic potential and yields rate constants close to the ones obtained by exclusive use of the accurate potential. As no 1^{st} and 2^{nd} derivatives of the refined potential are necessary, but only single point energy calculations are performed, highly accurate electronic structure methods like explicitly correlated coupled cluster (UCCSD(T)-F12) can now be used in combination with instanton theory. It is shown that the basic potential has to describe the reaction energy qualitatively correctly. If this is not the case, the distribution of the images of the discretized Feynman path is distorted and so is the value of S_0. This can not be corrected by means of a better potential energy hyper surface.

The reaction

$$H_2 + OH \rightarrow H_2O + H \tag{R 8}$$

is one of the main water formation routes in the interstellar medium, in particular in cold dense cores. In this thesis, reaction rate constants of the gas phase reaction have been carried out using instanton theory and canonical variational theory with microcanonical optimized multidimensional tunneling (CVT/μOMT) The rate constants are in excellent agreement with experimental values at temperatures down to 200 K. At lower temperatures, down to 50 K, reaction rate constants are calculated for which no experimental values are available. Furthermore, kinetic isotope effects (KIEs) have been calculated for all possible isotope patterns. The KIE for the subsitution of the transferred hydrogen atom by a deuterium atom is 176 at 100 K and 382 at 50 K. The secondary KIEs are smaller and stem partially from differences in zero-point energy.

In this thesis, the influence of a water ice surface on reaction reaction (R 8) was investigated. For that, density functional theory rigorously benchmarked against highly accurate correlation methods (UCCSD(T)-F12) in combination with the TIP3P force field in a QM/MM setup was used. Three different binding sites of the OH radical with adsorption energies of 32.1–40.5 kJ mol^{-1} have been found. The potential energy along the reaction coordinate is barely affected by the chemical environment of the water molecules. The reason of this absence of a classical catalytic effect is that the transition structure is not stabilized because all hydrogen bonds are already formed in the reactant complex. Therefore, the influence of the surface was taken into account by the *implicit surface model*, which modifies the rotational and translational partition functions during the reaction. Reaction rate constans using instanton theory down to 100 K for the Eley–Rideal mechanism and down to 60 K for the Langmuir–Hinshelwood mechanism are presented. For both mechanisms, KIEs of all possible H/D patterns have been calculated, showing the same trends as the gas-phase calculations.

This work presents values of reaction rate constants which can be used for astrochemical modeling. The gas-phase rate constants are important for the simulation of chemical reaction networks in protoplanetary discs while the reaction rates for the surface reactions are crucial for the water formation in dense molecular clouds. The kinetic isotope effects differ from the ones used in kinetic data bases and can help to model the HDO/H_2O ratio in the interstellar medium.

Part IV

Appendix

12 Gradient of the DWI Surface

The DWI-Energy is given as

$$E^{\mathrm{DWI}}(\boldsymbol{x}) = T_1(\boldsymbol{x})w_1(\boldsymbol{x}) + T_2(\boldsymbol{x})w_2(\boldsymbol{x}) \tag{12.1}$$

where 1 and 2 stand for the old respective new predictor coordinates, respectively. Thus, the gradient is simply

$$\begin{aligned} \nabla E^{\mathrm{DWI}}(\boldsymbol{x}) &= \nabla T_1(\boldsymbol{x})w_1(\boldsymbol{x}) \\ &+ T_1(\boldsymbol{x})\nabla w_1(\boldsymbol{x}) \\ &+ \nabla T_2(\boldsymbol{x})w_2(\boldsymbol{x}) \\ &+ T_2(\boldsymbol{x})\nabla w_2(\boldsymbol{x}) \end{aligned} \tag{12.2}$$

The gradients of the Taylor expansions are obtained quite intuitively:

$$\nabla T_1(\boldsymbol{x}) = \boldsymbol{g(x_1)} + \mathbf{H}(\mathrm{x}_1)\boldsymbol{\Delta x}_1 \tag{12.3}$$

with

$$\boldsymbol{\Delta x}_i = \boldsymbol{x} - \boldsymbol{x}_i. \tag{12.4}$$

The derivative of the squared distance with respect to coordinate $x^{(k)}$ is

$$
\begin{aligned}
\frac{\partial}{\partial x^{(k)}} |\boldsymbol{\Delta x_2}|^{2n} &= \frac{\partial}{\partial x^{(k)}} \left(\sqrt{\sum_l \left(x_2^{(k)} - x^{(k)} \right)^2} \right)^{2n} \\
&= \frac{\partial}{\partial x^{(k)}} \left(\underbrace{\sum_l \left(x_2^{(k)} - x^{(k)} \right)^2}_{|\boldsymbol{\Delta x_2}|^2} \right)^{n} \\
&= n \left(|\boldsymbol{\Delta x_2}|^2 \right)^{n-1} \cdot \frac{\partial}{\partial x^{(k)}} \left(\underbrace{\sum_l \left(x_2^{(k)} - x^{(k)} \right)^2}_{|\boldsymbol{\Delta x_2}|^2} \right) \\
&= n \left(|\boldsymbol{\Delta x_2}|^2 \right)^{n-1} 2(x^{(k)} - x_2^{(k)})
\end{aligned}
\tag{12.5}
$$

Thus, the gradient is

$$
\nabla |\boldsymbol{\Delta x_2}|^{2n} = 2n \left(|\boldsymbol{\Delta x_2}|^2 \right)^{n-1} (\boldsymbol{x} - \boldsymbol{x_2}) \tag{12.6}
$$

The gradient of the weights is:

$$\nabla w_1(\boldsymbol{x}) = \nabla \left(\frac{|\boldsymbol{\Delta x}_2|^{2n}}{|\boldsymbol{\Delta x}_1|^{2n} + |\boldsymbol{\Delta x}_2|^{2n}} \right) \tag{12.7}$$

$$= \frac{\nabla|\boldsymbol{\Delta x}_2|^{2n} \cdot (|\boldsymbol{\Delta x}_1|^{2n} + |\boldsymbol{\Delta x}_2|^{2n}) - |\boldsymbol{\Delta x}_2|^{2n} \cdot \nabla\left(|\boldsymbol{\Delta x}_1|^{2n} + |\boldsymbol{\Delta x}_2|^{2n}\right)}{\left(|\boldsymbol{\Delta x}_1|^{2n} + |\boldsymbol{\Delta x}_2|^{2n}\right)^2}$$

$$= \frac{\nabla|\boldsymbol{\Delta x}_2|^{2n} \cdot |\boldsymbol{\Delta x}_1|^{2n} - |\boldsymbol{\Delta x}_2|^{2n} \cdot \nabla|\boldsymbol{\Delta x}_1|^{2n}}{\left(|\boldsymbol{\Delta x}_1|^{2n} + |\boldsymbol{\Delta x}_2|^{2n}\right)^2}$$

$$= \frac{2n|\boldsymbol{\Delta x}_2|^{2n-2}(\boldsymbol{x} - \boldsymbol{x_2}) \cdot |\boldsymbol{\Delta x}_1|^{2n} - |\boldsymbol{\Delta x}_2|^{2n} \cdot 2n|\boldsymbol{\Delta x}_1|^{2n-2}(\boldsymbol{x} - \boldsymbol{x_1})}{\left(|\boldsymbol{\Delta x}_1|^{2n} + |\boldsymbol{\Delta x}_2|^{2n}\right)^2}$$

$$= \frac{2n\left(|\boldsymbol{\Delta x_1}||\boldsymbol{\Delta x_2}|\right)^{2n-2}}{\left(|\boldsymbol{\Delta x}_1|^{2n} + |\boldsymbol{\Delta x}_2|^{2n}\right)^2} \left[(\boldsymbol{x} - \boldsymbol{x_2}) \cdot |\boldsymbol{\Delta x}_1|^2 - |\boldsymbol{\Delta x}_2|^2 \cdot |(\boldsymbol{x} - \boldsymbol{x_1})\right]$$

13 Richardson Extrapolation

The series acceleration method of Richardson extrapolation is outlined here. The idea is to reduce the formal order of error by using another, smaller stepsize. In the case of the Hessian-based predictor-corrector algorithmus, the integration is carried out with the explicit Euler method within the Local Quadratic Approximation (LQA). This is a method of 0^{th} order and, thus, the result has an error of first order with respect of the step size h. The integration result with the stepsize h, $x(h)$ is expanded in a Taylor series of orders of h, leading to the expression

$$x(h) = a_0 + h\, a_1 + \mathcal{O}(h^2) \tag{13.1}$$

where $a_0 = x(h = 0)$ is the unknown, desired value without error in the step size, a_1 the linear coefficient and so forth. If the calculation is repeated with a smaller step size kh, where $0 > k > 1$, the result

$$x(kh) = a_0 + kha_1 + \mathcal{O}((kh)^2) \tag{13.2}$$

is obtained. The linear term can be eliminated:

$$x(kh) - k \cdot x(h) = a_0\,(1 - k) + \mathcal{O}(h^2) \Rightarrow a_0 \approx \frac{x(kh) - k \cdot x(h)}{1 - k} \tag{13.3}$$

The approximate value of a_0 is, thus, a result with an error of second order in h. This result can be reused in the Neville scheme see Fig. 3.1.

To further improve the result, the error of 2^{nd} order has to be eliminated. For this iterative process, we assume this solution having a step size of kh.

In general, a method of $(p-1)^{\text{th}}$ order has an error of p^{th} order in stepsize:

$$x(h) = a_0 + h^p a_p + \mathcal{O}(h^r) \tag{13.4}$$

The remaining error is of order r with $r > p$. If we are interested in the reduction of the h^p term, we use a similar formula:

$$a_0 \approx \frac{x(kh) - k^p \cdot x(h)}{1 - k^p} \tag{13.5}$$

14 Rate Constants for the Gas-Phase Reaction

Table 14.1 Reaction rate constants for the H-transfer calculated with the instanton method on the NN1 PES. Temperature in K, rate constants in cm^3 molecule^{-1} s^{-1}.

T [K]	HHOH	HHOD	DHOH	DHOD
100	$9.05 \cdot 10^{-18}$	$1.61 \cdot 10^{-17}$	$2.29 \cdot 10^{-18}$	$4.43 \cdot 10^{-18}$
105	$1.07 \cdot 10^{-17}$	$1.87 \cdot 10^{-17}$	$2.75 \cdot 10^{-18}$	$5.20 \cdot 10^{-18}$
110	$1.26 \cdot 10^{-17}$	$2.17 \cdot 10^{-17}$	$3.31 \cdot 10^{-18}$	$6.15 \cdot 10^{-18}$
115	$1.49 \cdot 10^{-17}$	$2.54 \cdot 10^{-17}$	$4.01 \cdot 10^{-18}$	$7.35 \cdot 10^{-18}$
120	$1.78 \cdot 10^{-17}$	$2.98 \cdot 10^{-17}$	$4.87 \cdot 10^{-18}$	$8.75 \cdot 10^{-18}$
130	$2.53 \cdot 10^{-17}$	$4.15 \cdot 10^{-17}$	$7.25 \cdot 10^{-18}$	$1.27 \cdot 10^{-17}$
140	$3.65 \cdot 10^{-17}$	$5.85 \cdot 10^{-17}$	$1.10 \cdot 10^{-17}$	$1.86 \cdot 10^{-17}$
150	$5.10 \cdot 10^{-17}$	$8.30 \cdot 10^{-17}$	$1.77 \cdot 10^{-17}$	$2.92 \cdot 10^{-17}$
155	$6.55 \cdot 10^{-17}$	$1.02 \cdot 10^{-16}$	$2.08 \cdot 10^{-17}$	$3.37 \cdot 10^{-17}$
160	$8.05 \cdot 10^{-17}$	$1.25 \cdot 10^{-16}$	$2.53 \cdot 10^{-17}$	$4.06 \cdot 10^{-17}$
165	$9.40 \cdot 10^{-17}$	$1.44 \cdot 10^{-16}$	$3.15 \cdot 10^{-17}$	$5.00 \cdot 10^{-17}$
170	$1.14 \cdot 10^{-16}$	$1.72 \cdot 10^{-16}$	$3.93 \cdot 10^{-17}$	$6.15 \cdot 10^{-17}$
175	$1.38 \cdot 10^{-16}$	$2.07 \cdot 10^{-16}$	$4.90 \cdot 10^{-17}$	$7.60 \cdot 10^{-17}$
180	$1.68 \cdot 10^{-16}$	$2.50 \cdot 10^{-16}$	$6.10 \cdot 10^{-17}$	$9.35 \cdot 10^{-17}$
185	$2.05 \cdot 10^{-16}$	$3.03 \cdot 10^{-16}$	$7.60 \cdot 10^{-17}$	$1.16 \cdot 10^{-16}$
190	$2.51 \cdot 10^{-16}$	$3.68 \cdot 10^{-16}$	$9.50 \cdot 10^{-17}$	$1.43 \cdot 10^{-16}$
195	$3.08 \cdot 10^{-16}$	$4.48 \cdot 10^{-16}$	$1.19 \cdot 10^{-16}$	$1.77 \cdot 10^{-16}$
200	$3.78 \cdot 10^{-16}$	$5.45 \cdot 10^{-16}$	$1.49 \cdot 10^{-16}$	$2.20 \cdot 10^{-16}$
210	$5.75 \cdot 10^{-16}$	$8.20 \cdot 10^{-16}$	$2.37 \cdot 10^{-16}$	$3.44 \cdot 10^{-16}$
220	$8.90 \cdot 10^{-16}$	$1.26 \cdot 10^{-15}$	$3.82 \cdot 10^{-16}$	$5.50 \cdot 10^{-16}$
230	$1.39 \cdot 10^{-15}$	$1.95 \cdot 10^{-15}$	$6.20 \cdot 10^{-16}$	$8.85 \cdot 10^{-16}$
240	$2.19 \cdot 10^{-15}$	$3.04 \cdot 10^{-15}$	$1.00 \cdot 10^{-15}$	$1.41 \cdot 10^{-15}$
250	$3.36 \cdot 10^{-15}$	$4.63 \cdot 10^{-15}$	$1.55 \cdot 10^{-15}$	$2.17 \cdot 10^{-15}$

Table 14.2 Reaction rate constants for the D-transfer calculated with the instanton method on the NN1 PES. Temperature in K, rate constants in cm^3 molecule^{-1} s^{-1}.

T [K]	HDOH	DDOH	HDOD	DDOD
80	$1.35 \cdot 10^{-20}$	$3.07 \cdot 10^{-20}$	$1.25 \cdot 10^{-20}$	$3.01 \cdot 10^{-20}$
84	$1.66 \cdot 10^{-20}$	$3.70 \cdot 10^{-20}$	$1.56 \cdot 10^{-20}$	$3.66 \cdot 10^{-20}$
88	$2.06 \cdot 10^{-20}$	$4.48 \cdot 10^{-20}$	$1.95 \cdot 10^{-20}$	$4.49 \cdot 10^{-20}$
92	$2.56 \cdot 10^{-20}$	$5.50 \cdot 10^{-20}$	$2.47 \cdot 10^{-20}$	$5.55 \cdot 10^{-20}$
96	$3.20 \cdot 10^{-20}$	$6.75 \cdot 10^{-20}$	$3.14 \cdot 10^{-20}$	$6.95 \cdot 10^{-20}$
100	$4.03 \cdot 10^{-20}$	$8.35 \cdot 10^{-20}$	$4.02 \cdot 10^{-20}$	$8.70 \cdot 10^{-20}$
105	$5.40 \cdot 10^{-20}$	$1.10 \cdot 10^{-19}$	$5.50 \cdot 10^{-20}$	$1.17 \cdot 10^{-19}$
110	$7.25 \cdot 10^{-20}$	$1.45 \cdot 10^{-19}$	$7.55 \cdot 10^{-20}$	$1.58 \cdot 10^{-19}$
115	$9.80 \cdot 10^{-20}$	$1.92 \cdot 10^{-19}$	$1.10 \cdot 10^{-19}$	$2.24 \cdot 10^{-19}$
120	$1.40 \cdot 10^{-19}$	$2.71 \cdot 10^{-19}$	$1.50 \cdot 10^{-19}$	$3.01 \cdot 10^{-19}$
130	$2.53 \cdot 10^{-19}$	$4.74 \cdot 10^{-19}$	$2.95 \cdot 10^{-19}$	$5.70 \cdot 10^{-19}$
135	$3.48 \cdot 10^{-19}$	$6.45 \cdot 10^{-19}$	$4.20 \cdot 10^{-19}$	$8.65 \cdot 10^{-19}$
140	$4.85 \cdot 10^{-19}$	$8.85 \cdot 10^{-19}$	$6.00 \cdot 10^{-19}$	$1.13 \cdot 10^{-18}$
145	$6.80 \cdot 10^{-19}$	$1.22 \cdot 10^{-18}$	$8.65 \cdot 10^{-19}$	$1.60 \cdot 10^{-18}$
150	$9.55 \cdot 10^{-19}$	$1.70 \cdot 10^{-18}$	$1.25 \cdot 10^{-18}$	$2.28 \cdot 10^{-18}$
155	$1.36 \cdot 10^{-18}$	$2.39 \cdot 10^{-18}$	$2.00 \cdot 10^{-18}$	$3.27 \cdot 10^{-18}$
160	$1.94 \cdot 10^{-18}$	$3.37 \cdot 10^{-18}$	$2.67 \cdot 10^{-18}$	$4.72 \cdot 10^{-18}$
165	$2.80 \cdot 10^{-18}$	$4.81 \cdot 10^{-18}$	$3.92 \cdot 10^{-18}$	$6.85 \cdot 10^{-18}$
170	$4.04 \cdot 10^{-18}$	$6.90 \cdot 10^{-18}$	$5.80 \cdot 10^{-18}$	$1.01 \cdot 10^{-17}$
175	$5.85 \cdot 10^{-18}$	$9.95 \cdot 10^{-18}$	$8.55 \cdot 10^{-18}$	$1.47 \cdot 10^{-17}$
180	$8.55 \cdot 10^{-18}$	$1.43 \cdot 10^{-17}$	$1.26 \cdot 10^{-17}$	$2.14 \cdot 10^{-17}$
185	$1.23 \cdot 10^{-17}$	$2.05 \cdot 10^{-17}$	$1.82 \cdot 10^{-17}$	$3.08 \cdot 10^{-17}$
190	$1.75 \cdot 10^{-17}$	$2.90 \cdot 10^{-17}$	$2.61 \cdot 10^{-17}$	$4.39 \cdot 10^{-17}$
195	$2.47 \cdot 10^{-17}$	$4.06 \cdot 10^{-17}$	$3.73 \cdot 10^{-17}$	$6.25 \cdot 10^{-17}$

Table 14.3 Reaction rate constants for the H-transfer calculated with CVT/μOMT on the NN1 PES. Temperature in K, rate constants in cm^3 molecule^{-1} s^{-1}.

T [K]	HHOH	HHOD	DHOH	DHOD
50	$1.25 \cdot 10^{-17}$	$2.05 \cdot 10^{-17}$	$1.82 \cdot 10^{-18}$	$3.65 \cdot 10^{-18}$
55	$1.35 \cdot 10^{-17}$	$2.16 \cdot 10^{-17}$	$2.01 \cdot 10^{-18}$	$3.93 \cdot 10^{-18}$
60	$1.47 \cdot 10^{-17}$	$2.31 \cdot 10^{-17}$	$2.26 \cdot 10^{-18}$	$4.28 \cdot 10^{-18}$
65	$1.62 \cdot 10^{-17}$	$2.49 \cdot 10^{-17}$	$2.56 \cdot 10^{-18}$	$4.72 \cdot 10^{-18}$
70	$1.80 \cdot 10^{-17}$	$2.71 \cdot 10^{-17}$	$2.94 \cdot 10^{-18}$	$5.25 \cdot 10^{-18}$
75	$2.02 \cdot 10^{-17}$	$2.98 \cdot 10^{-17}$	$3.39 \cdot 10^{-18}$	$5.95 \cdot 10^{-18}$
80	$2.27 \cdot 10^{-17}$	$3.29 \cdot 10^{-17}$	$3.95 \cdot 10^{-18}$	$6.75 \cdot 10^{-18}$
90	$2.93 \cdot 10^{-17}$	$4.12 \cdot 10^{-17}$	$5.45 \cdot 10^{-18}$	$8.90 \cdot 10^{-18}$
100	$3.85 \cdot 10^{-17}$	$5.25 \cdot 10^{-17}$	$7.70 \cdot 10^{-18}$	$1.21 \cdot 10^{-17}$
110	$5.15 \cdot 10^{-17}$	$6.85 \cdot 10^{-17}$	$1.11 \cdot 10^{-17}$	$1.67 \cdot 10^{-17}$
120	$6.95 \cdot 10^{-17}$	$9.05 \cdot 10^{-17}$	$1.61 \cdot 10^{-17}$	$2.34 \cdot 10^{-17}$
130	$9.45 \cdot 10^{-17}$	$1.21 \cdot 10^{-16}$	$2.35 \cdot 10^{-17}$	$3.32 \cdot 10^{-17}$
140	$1.30 \cdot 10^{-16}$	$1.63 \cdot 10^{-16}$	$3.45 \cdot 10^{-17}$	$4.73 \cdot 10^{-17}$
150	$1.80 \cdot 10^{-16}$	$2.21 \cdot 10^{-16}$	$5.05 \cdot 10^{-17}$	$6.75 \cdot 10^{-17}$
160	$2.48 \cdot 10^{-16}$	$3.00 \cdot 10^{-16}$	$7.35 \cdot 10^{-17}$	$9.60 \cdot 10^{-17}$
180	$4.69 \cdot 10^{-16}$	$5.45 \cdot 10^{-16}$	$1.53 \cdot 10^{-16}$	$1.92 \cdot 10^{-16}$
200	$8.65 \cdot 10^{-16}$	$9.75 \cdot 10^{-16}$	$3.03 \cdot 10^{-16}$	$3.67 \cdot 10^{-16}$
220	$1.53 \cdot 10^{-15}$	$1.68 \cdot 10^{-15}$	$5.70 \cdot 10^{-16}$	$6.65 \cdot 10^{-16}$
240	$2.60 \cdot 10^{-15}$	$2.78 \cdot 10^{-15}$	$1.01 \cdot 10^{-15}$	$1.14 \cdot 10^{-15}$
250	$3.34 \cdot 10^{-15}$	$3.53 \cdot 10^{-15}$	$1.31 \cdot 10^{-15}$	$1.47 \cdot 10^{-15}$
298	$9.60 \cdot 10^{-15}$	$9.70 \cdot 10^{-15}$	$3.97 \cdot 10^{-15}$	$4.23 \cdot 10^{-15}$
300	$1.00 \cdot 10^{-14}$	$1.01 \cdot 10^{-14}$	$4.10 \cdot 10^{-15}$	$4.40 \cdot 10^{-15}$
400	$4.94 \cdot 10^{-14}$	$4.67 \cdot 10^{-14}$	$2.09 \cdot 10^{-14}$	$2.09 \cdot 10^{-14}$
600	$3.15 \cdot 10^{-13}$	$2.93 \cdot 10^{-13}$	$1.38 \cdot 10^{-13}$	$1.30 \cdot 10^{-13}$
800	$1.01 \cdot 10^{-12}$	$8.80 \cdot 10^{-13}$	$4.24 \cdot 10^{-13}$	$3.89 \cdot 10^{-13}$
1000	$2.18 \cdot 10^{-12}$	$1.88 \cdot 10^{-12}$	$9.30 \cdot 10^{-13}$	$8.35 \cdot 10^{-13}$
1250	$4.48 \cdot 10^{-12}$	$3.81 \cdot 10^{-12}$	$1.95 \cdot 10^{-12}$	$1.75 \cdot 10^{-12}$
1500	$7.80 \cdot 10^{-12}$	$6.60 \cdot 10^{-12}$	$3.46 \cdot 10^{-12}$	$3.10 \cdot 10^{-12}$
2000	$1.82 \cdot 10^{-11}$	$1.53 \cdot 10^{-11}$	$8.20 \cdot 10^{-12}$	$7.35 \cdot 10^{-12}$

Table 14.4 Reaction rate constants for the D-transfer calculated with CVT/μOMT on the NN1 PES. Temperature in K, rate constants in cm^3 molecule^{-1} s^{-1}.

T [K]	HDOH	HDOD	DDOH	DDOD
50	$3.27 \cdot 10^{-20}$	$5.80 \cdot 10^{-20}$	$2.24 \cdot 10^{-20}$	$5.45 \cdot 10^{-20}$
55	$3.71 \cdot 10^{-20}$	$6.50 \cdot 10^{-20}$	$2.63 \cdot 10^{-20}$	$6.15 \cdot 10^{-20}$
60	$4.28 \cdot 10^{-20}$	$7.45 \cdot 10^{-20}$	$3.14 \cdot 10^{-20}$	$7.15 \cdot 10^{-20}$
65	$5.00 \cdot 10^{-20}$	$8.70 \cdot 10^{-20}$	$3.83 \cdot 10^{-20}$	$8.45 \cdot 10^{-20}$
70	$5.95 \cdot 10^{-20}$	$1.03 \cdot 10^{-19}$	$4.75 \cdot 10^{-20}$	$1.01 \cdot 10^{-19}$
75	$7.15 \cdot 10^{-20}$	$1.23 \cdot 10^{-19}$	$5.95 \cdot 10^{-20}$	$1.24 \cdot 10^{-19}$
80	$8.75 \cdot 10^{-20}$	$1.49 \cdot 10^{-19}$	$7.60 \cdot 10^{-20}$	$1.53 \cdot 10^{-19}$
90	$1.36 \cdot 10^{-19}$	$2.26 \cdot 10^{-19}$	$1.28 \cdot 10^{-19}$	$2.44 \cdot 10^{-19}$
100	$2.19 \cdot 10^{-19}$	$3.54 \cdot 10^{-19}$	$2.23 \cdot 10^{-19}$	$4.04 \cdot 10^{-19}$
110	$3.63 \cdot 10^{-19}$	$5.70 \cdot 10^{-19}$	$4.00 \cdot 10^{-19}$	$6.90 \cdot 10^{-19}$
120	$6.10 \cdot 10^{-19}$	$9.35 \cdot 10^{-19}$	$7.25 \cdot 10^{-19}$	$1.21 \cdot 10^{-18}$
130	$1.04 \cdot 10^{-18}$	$1.55 \cdot 10^{-18}$	$1.33 \cdot 10^{-18}$	$2.12 \cdot 10^{-18}$
140	$1.78 \cdot 10^{-18}$	$2.57 \cdot 10^{-18}$	$2.42 \cdot 10^{-18}$	$3.72 \cdot 10^{-18}$
150	$3.02 \cdot 10^{-18}$	$4.26 \cdot 10^{-18}$	$4.34 \cdot 10^{-18}$	$6.50 \cdot 10^{-18}$
160	$5.05 \cdot 10^{-18}$	$7.00 \cdot 10^{-18}$	$7.65 \cdot 10^{-18}$	$1.11 \cdot 10^{-17}$
180	$1.38 \cdot 10^{-17}$	$1.81 \cdot 10^{-17}$	$2.22 \cdot 10^{-17}$	$3.04 \cdot 10^{-17}$
200	$3.47 \cdot 10^{-17}$	$4.35 \cdot 10^{-17}$	$5.80 \cdot 10^{-17}$	$7.60 \cdot 10^{-17}$
220	$8.00 \cdot 10^{-17}$	$9.60 \cdot 10^{-17}$	$1.36 \cdot 10^{-16}$	$1.71 \cdot 10^{-16}$
240	$1.70 \cdot 10^{-16}$	$1.97 \cdot 10^{-16}$	$2.91 \cdot 10^{-16}$	$3.53 \cdot 10^{-16}$
250	$2.41 \cdot 10^{-16}$	$2.75 \cdot 10^{-16}$	$4.12 \cdot 10^{-16}$	$4.93 \cdot 10^{-16}$
298	$1.01 \cdot 10^{-15}$	$1.07 \cdot 10^{-15}$	$1.71 \cdot 10^{-15}$	$1.91 \cdot 10^{-15}$
300	$1.07 \cdot 10^{-15}$	$1.13 \cdot 10^{-15}$	$1.80 \cdot 10^{-15}$	$2.01 \cdot 10^{-15}$
400	$8.40 \cdot 10^{-15}$	$8.15 \cdot 10^{-15}$	$1.36 \cdot 10^{-14}$	$1.37 \cdot 10^{-14}$
600	$8.60 \cdot 10^{-14}$	$7.75 \cdot 10^{-14}$	$1.35 \cdot 10^{-13}$	$1.29 \cdot 10^{-13}$
800	$3.21 \cdot 10^{-13}$	$2.80 \cdot 10^{-13}$	$5.05 \cdot 10^{-13}$	$4.68 \cdot 10^{-13}$
1000	$7.80 \cdot 10^{-13}$	$6.70 \cdot 10^{-13}$	$1.25 \cdot 10^{-12}$	$1.14 \cdot 10^{-12}$
1250	$1.75 \cdot 10^{-12}$	$1.49 \cdot 10^{-12}$	$2.86 \cdot 10^{-12}$	$2.58 \cdot 10^{-12}$
1500	$3.23 \cdot 10^{-12}$	$2.72 \cdot 10^{-12}$	$5.40 \cdot 10^{-12}$	$4.81 \cdot 10^{-12}$
2000	$8.00 \cdot 10^{-12}$	$6.70 \cdot 10^{-12}$	$1.36 \cdot 10^{-11}$	$1.20 \cdot 10^{-11}$

15 Details of the Calculations of the Surface Reaction

15.1 Choice of the Electronic Potential

To obtain a reliable electronic potential for the rate calculations, firstly, the stationary points (pre-reactive complex, transition state structure, and product state) and the separated reactants were optimized on highly accurate UCCSD(T)-F12[207,208] level using an aug-cc-pVTZ basis set[280] to ensure a basis set size close to the basis set limit.[207] A restricted open shell Hartree-Fock (ROHF) wave function was used as reference for the UCCSD(T)-F12 calculations. This electronic potential leads to a pre-reactive complex, a transition state structure, and a product state with energies of $-2.07\,\mathrm{kJ\ mol^{-1}}$, $22.52\,\mathrm{kJ\ mol^{-1}}$, and $-67.93\,\mathrm{kJ\ mol^{-1}}$, respectively, with respect to the separated reactants. The barrier relative to the pre-reactive complex is, thus, $24.58\,\mathrm{kJ\ mol^{-1}}$.

Single point energy calculations with various functionals (B3LYP,[217–222] B97-D,[281] BHLYP,[217,218,220,221,234] BP86,[217–220,233] M06-2X,[282] PBE0,[217,218,283,284,284] PBEh-3C,[285] PBE,[217,218,283,284] TPSSH,[217,218,283,286,287] TPSS,[217,218,283,286] and VWN[219]) and basis sets have been performed and compared. For the functionals where Grimme's dispersion correction was feasible, the influence of the D3 dispersion correction scheme[288] was tested. The values have been compared to the UCCSD(T)-F12 values in order to find the most suitable density functional to describe the reaction. The resulting relative energies can be seen in table S 1 and S 2. The most suitable density functional in terms of accuracy-to-cost ratio was found to be BHLYP[217,218,220,221,234] in combination with the def2-SVPD basis set.[273] Dispersion correction in general only has minor effect and, in the case of

BHLYP/def2-SVPD, deteriorated the quality of the potential, in particular in the region around the pre-reactive complex.

The errors in the depth of the potential well and the barrier height are only 0.11 kJ mol^{-1} and 0.32 kJ mol^{-1}, respectively. The curvature around the transition state structure, which is important to elucidate the impact of tunneling, results in an imaginary frequency of 1259.6 i cm^{-1}. At the DFT level this value is 56.9 i cm^{-1} larger than the UCCSD(T)-F12 reference of 1202.8 i cm^{-1}.

Table 15.1 Relative potential energies to H_2 + OH in kJ mol^{-1}. V_{PRC}, V_A, and ΔV denote the potential energies of pre-reactive complex, transition state structure, and products (H_2O + H), respectively, with respect to the separated reactants OH and H_2.

Basis Set		B3LYP	B97-D	BHLYP	BP86	M06-2X	PBE0	PBEh-3C	PBE	TPSSH	TPSS	VWN
SVP	V_{PRC}	−2.48	−2.27	−2.37	−1.08	−4.29	−2.96	−2.37	−4.42	−2.45	−2.83	−30.41
	V_A	0.62	−4.44	24.83	−19.15	20.75	0.47	9.47	−25.01	1.70	−5.64	4.80
	ΔV	−48.53	−43.85	−36.80	−56.66	−60.02	−67.30	−58.45	−78.11	−28.88	−29.21	51.68
SVPD	V_{PRC}	−2.15	−2.31	−2.16	−0.83	−4.21	−2.86	−2.31	−4.40	−2.10	−2.40	−10.78
	V_A	−2.47	−8.05	22.83	−23.68	18.24	−3.13	6.12	−29.56	−1.83	−9.44	26.22
	ΔV	−66.49	−60.78	−52.90	−74.61	−75.02	−83.84	−73.85	−96.53	−45.74	−46.74	90.98
TZVP	V_{PRC}	−0.65	−0.59	−1.02	0.49	−2.94	−1.65	−1.39	−2.73	−0.99	−1.24	−2.10
	V_A	6.85	1.44	29.98	−14.24	24.07	4.95	12.87	−19.37	5.17	−2.17	45.04
	ΔV	−44.97	−40.54	−32.84	−54.96	−59.10	−65.07	−56.42	−76.02	−30.01	−31.16	101.43
TZVPD	V_{PRC}	−0.72	−0.66	−1.16	0.32	−3.27	−1.81	−1.64	−2.87	−1.06	−1.28	−2.04
	V_A	5.14	−0.49	28.83	−16.67	22.37	3.20	11.24	−21.76	3.44	−4.10	42.90
	ΔV	−49.23	−44.66	−36.37	−59.53	−62.62	−69.07	−59.99	−80.83	−34.04	−35.47	110.63
TZVPP	V_{PRC}	−0.90	−0.84	−1.24	0.22	−3.15	−1.90	−1.62	−3.03	−1.25	−1.51	−3.41
	V_A	5.30	−0.23	28.66	−16.22	22.18	3.10	11.10	−21.35	3.37	−4.04	41.09
	ΔV	−49.43	−44.56	−37.16	−59.54	−62.48	−69.44	−60.73	−80.57	−33.88	−35.11	97.55
TZVPPD	V_{PRC}	−0.76	−0.67	−1.19	0.29	−3.26	−1.84	−1.66	−2.92	−1.12	−1.34	−2.07
	V_A	4.51	−1.16	28.26	−17.41	21.48	2.36	10.49	−22.60	2.63	−4.93	41.60
	ΔV	−52.21	−47.29	−39.33	−62.37	−64.43	−71.97	−62.75	−83.81	−36.49	−37.94	107.84

Table 15.2 Relative potential energies to H_2 + OH in kJ mol^{-1}. V_{PRC}, V_A, and ΔV denote the potential energies of pre-reactive complex, transition state structure, and products (H_2O + H), respectively, with respect to the separated reactants OH and H_2.

Basis Set		B3LYP-D3	BHLYP-D3	BP86-D3	PBE-D3	TPSS-D3	PBE0-D3	TPSSH-D3
SVP	V_{PRC}	−4.66	−4.04	−5.57	−7.82	−4.77	−4.25	−4.26
	V_A	−0.66	23.77	−20.55	−25.61	−6.57	−0.24	0.74
	ΔV	−49.76	−37.78	−58.05	−78.89	−30.26	−68.11	−29.91
SVPD	V_{PRC}	−4.32	−3.83	−3.54	−5.70	−4.35	−4.15	−3.90
	V_A	−3.75	21.77	−25.09	−30.16	−10.37	−3.84	−2.79
	ΔV	−67.72	−53.88	−76.00	−97.31	−47.79	−84.65	−46.77
TZVP	V_{PRC}	−2.83	−2.69	−2.22	−4.04	−3.18	−2.94	−2.79
	V_A	5.56	28.91	−15.65	−19.97	−3.11	4.24	4.22
	ΔV	−46.20	−33.82	−56.35	−76.80	−32.21	−65.88	−31.03
TZVPD	V_{PRC}	−2.90	−2.83	−2.39	−4.18	−3.23	−3.10	−2.87
	V_A	3.85	27.77	−18.08	−22.36	−5.04	2.49	2.48
	ΔV	−50.46	−37.35	−60.92	−81.62	−36.52	−69.88	−35.07
TZVPP	V_{PRC}	−3.07	−2.90	−2.49	−4.33	−3.46	−3.19	−3.06
	V_A	4.01	27.59	−17.62	−21.95	−4.98	2.39	2.41
	ΔV	−50.66	−38.14	−60.93	−81.35	−36.16	−70.25	−34.91
TZVPPD	V_{PRC}	−2.93	−2.86	−2.41	−4.22	−3.29	−3.13	−2.92
	V_A	3.22	27.19	−18.82	−23.20	−5.87	1.65	1.67
	ΔV	−53.44	−40.31	−63.76	−84.60	−38.99	−72.78	−37.52

Additionally, the energies of the intrinsic reaction coordinates (IRCs) at UCCSD(T)-F12 and BHLYP level are compared. In Fig S15.1 electronic energies of both methods along the corresponding IRC are ploted relative to the separated reactants' energies. The shapes of both electronic potentials are very similar in the region of the transition state structure which is the important region for reliable studies of reaction rate constants and atom tunneling.[1]

In the region around the reactants' valley and on the product side of the barrier up to the point where the energy becomes lower than the reactants' energy both curves are still surprisingly similar.

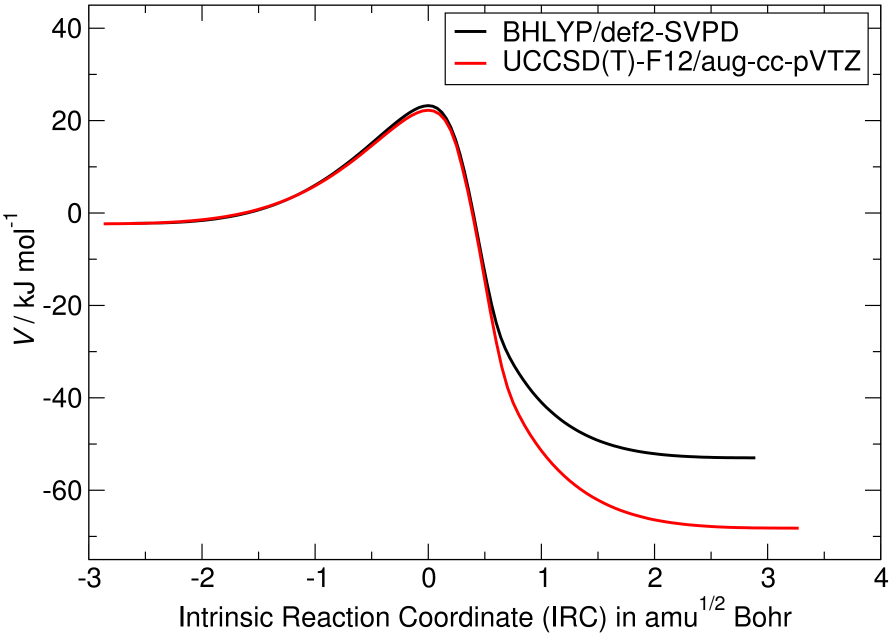

Figure 15.1 Comparison of the energies of the intrinsic reaction coordinates (IRCs) calculated with UCCSD(T)-F12/aug-cc-pVTZ and BHLYP/def2-SVPD. The energies are relative to the energy of the separated reactants.

15.2 Comparison of the IRCs of Intrinic Reaction Coordinates of direct and rotated Reaction Pathways

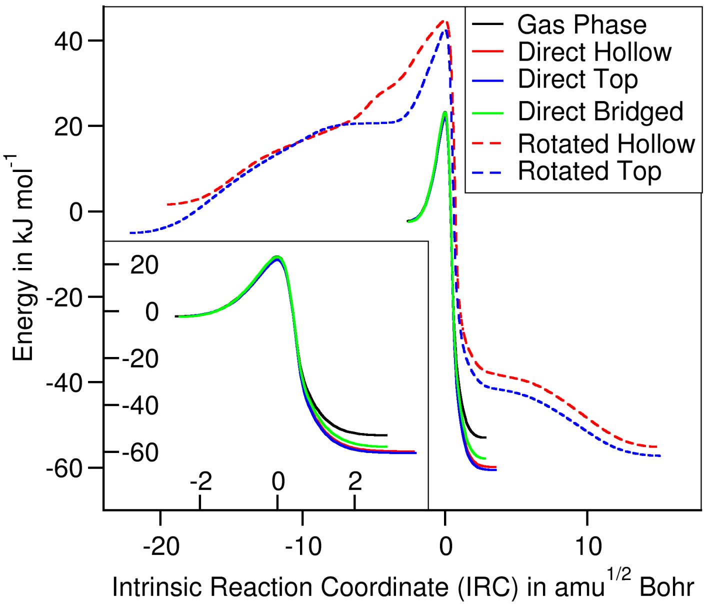

Figure 15.2 Potential energy along all intrinsic reaction coordinates (IRCs) found on the ice surface. The three *direct* reaction pathways deviate only marginally from the gas-phase reaction, as can be seen in the inset. The reaction pathways via *rotated* transition state structures are significantly longer than in the *direct* cases because of the lengthy OH rotation movement.

15.3 Rate Constants for the Reaction $H_2 + OH \rightarrow H_2O + H$ on an Ice Surface

Table 15.3 Bimolecular reaction rate constants for the Eley–Rideal mechanism on the ice surface, in the gas phase, and using the implicit surface model as described in the main text. All rate constants are in cm^3 s^{-1}.

T [K]	Surface	Gas Phase	Impl. Surface
110	$1.39 \cdot 10^{-18}$	$2.45 \cdot 10^{-17}$	$5.81 \cdot 10^{-19}$
112.5	$1.52 \cdot 10^{-18}$		
120	$1.98 \cdot 10^{-18}$	$3.33 \cdot 10^{-17}$	$7.80 \cdot 10^{-19}$
125	$2.45 \cdot 10^{-18}$		
130		$4.60 \cdot 10^{-17}$	$1.06 \cdot 10^{-18}$
138	$4.11 \cdot 10^{-18}$	$6.43 \cdot 10^{-17}$	$1.47 \cdot 10^{-18}$
150	$6.39 \cdot 10^{-18}$	$9.08 \cdot 10^{-17}$	$2.06 \cdot 10^{-18}$
165		$1.55 \cdot 10^{-16}$	$3.47 \cdot 10^{-18}$
175	$1.29 \cdot 10^{-17}$		
180		$2.70 \cdot 10^{-16}$	$5.97 \cdot 10^{-18}$
200	$3.49 \cdot 10^{-17}$	$5.75 \cdot 10^{-16}$	$1.26 \cdot 10^{-17}$
225	$9.11 \cdot 10^{-17}$	$1.52 \cdot 10^{-15}$	$3.28 \cdot 10^{-17}$
250	$2.51 \cdot 10^{-16}$	$4.11 \cdot 10^{-15}$	$8.75 \cdot 10^{-17}$

Table 15.4 Unimolecular reaction rate constants for the Langmuir–Hinshelwood mechanism on the ice surface, in the gas phase, and using the implicit surface model as described in the main text. All rate constants are in s^{-1}.

T [K]	Surface	Gas Phase	Impl. Surface
60		$5.47{\cdot}10^{5}$	$5.12{\cdot}10^{5}$
65		$5.38{\cdot}10^{5}$	$5.16{\cdot}10^{5}$
70		$5.46{\cdot}10^{5}$	$5.34{\cdot}10^{5}$
75		$5.67{\cdot}10^{5}$	$5.67{\cdot}10^{5}$
80	$2.06{\cdot}10^{5}$	$6.00{\cdot}10^{5}$	$6.12{\cdot}10^{5}$
90	$2.37{\cdot}10^{5}$	$7.00{\cdot}10^{5}$	$7.41{\cdot}10^{5}$
100	$2.85{\cdot}10^{5}$	$8.53{\cdot}10^{5}$	$9.35{\cdot}10^{5}$
105	$3.15{\cdot}10^{5}$		
110	$3.51{\cdot}10^{5}$	$1.08{\cdot}10^{6}$	$1.22{\cdot}10^{6}$
120	$4.37{\cdot}10^{5}$	$1.40{\cdot}10^{6}$	$1.63{\cdot}10^{6}$
125	$5.08{\cdot}10^{5}$		
130		$1.86{\cdot}10^{6}$	$2.23{\cdot}10^{6}$
137.5	$7.38{\cdot}10^{5}$		
140		$2.50{\cdot}10^{6}$	$3.08{\cdot}10^{6}$
150	$1.01{\cdot}10^{6}$	$3.42{\cdot}10^{6}$	$4.32{\cdot}10^{6}$
165		$5.57{\cdot}10^{6}$	$7.30{\cdot}10^{6}$
175	$1.61{\cdot}10^{6}$		
180		$9.26{\cdot}10^{6}$	$1.25{\cdot}10^{7}$
200	$3.50{\cdot}10^{6}$	$1.86{\cdot}10^{7}$	$2.63{\cdot}10^{7}$
225	$7.51{\cdot}10^{6}$	$4.60{\cdot}10^{7}$	$6.77{\cdot}10^{7}$
250	$1.73{\cdot}10^{7}$	$1.16{\cdot}10^{8}$	$1.78{\cdot}10^{8}$

15.4 Rate Constants using the Implicit Surface Model

Table 15.5 Bimolecular reaction rate constants in $\mathrm{cm}^3\ \mathrm{s}^{-1}$ for the H-transfer for the Eley–Rideal mechanism calculated using the implicit surface model. For $T \leq 250$ K, instanton theory and for $T \geq 300$ K, the Eckart approximation was used.

T[K]	HHOH	HHOD	DHOH	DHOD
100		$1.05\cdot10^{-18}$	$6.97\cdot10^{-20}$	$1.75\cdot10^{-19}$
110	$5.81\cdot10^{-19}$	$1.34\cdot10^{-18}$	$9.42\cdot10^{-20}$	$2.27\cdot10^{-19}$
120	$7.80\cdot10^{-19}$	$1.74\cdot10^{-18}$	$1.30\cdot10^{-19}$	$3.03\cdot10^{-19}$
130	$1.06\cdot10^{-18}$	$2.31\cdot10^{-18}$	$1.83\cdot10^{-19}$	$4.15\cdot10^{-19}$
140	$1.47\cdot10^{-18}$	$3.12\cdot10^{-18}$	$2.63\cdot10^{-19}$	$5.80\cdot10^{-19}$
150	$2.06\cdot10^{-18}$	$4.28\cdot10^{-18}$	$3.81\cdot10^{-19}$	$8.23\cdot10^{-19}$
165	$3.47\cdot10^{-18}$	$7.01\cdot10^{-18}$	$6.81\cdot10^{-19}$	$1.43\cdot10^{-18}$
180	$5.97\cdot10^{-18}$	$1.18\cdot10^{-17}$	$1.24\cdot10^{-18}$	$2.53\cdot10^{-18}$
200	$1.26\cdot10^{-17}$	$2.41\cdot10^{-17}$	$2.80\cdot10^{-18}$	$5.55\cdot10^{-18}$
225	$3.28\cdot10^{-17}$	$6.11\cdot10^{-17}$	$7.91\cdot10^{-18}$	$1.52\cdot10^{-17}$
250	$8.75\cdot10^{-17}$	$1.59\cdot10^{-16}$	$2.26\cdot10^{-17}$	$4.24\cdot10^{-17}$
300	$2.74\cdot10^{-16}$	$4.66\cdot10^{-16}$	$6.78\cdot10^{-17}$	$1.18\cdot10^{-16}$
333	$4.95\cdot10^{-16}$	$8.11\cdot10^{-16}$	$1.23\cdot10^{-16}$	$2.05\cdot10^{-16}$
375	$9.29\cdot10^{-16}$	$1.47\cdot10^{-15}$	$2.30\cdot10^{-16}$	$3.71\cdot10^{-16}$
429	$1.81\cdot10^{-15}$	$2.75\cdot10^{-15}$	$4.48\cdot10^{-16}$	$6.97\cdot10^{-16}$
500	$3.66\cdot10^{-15}$	$5.39\cdot10^{-15}$	$9.10\cdot10^{-16}$	$1.37\cdot10^{-15}$
600	$7.80\cdot10^{-15}$	$1.11\cdot10^{-14}$	$1.94\cdot10^{-15}$	$2.83\cdot10^{-15}$
750	$1.77\cdot10^{-14}$	$2.45\cdot10^{-14}$	$4.46\cdot10^{-15}$	$6.31\cdot10^{-15}$
1000	$4.48\cdot10^{-14}$	$6.06\cdot10^{-14}$	$1.15\cdot10^{-14}$	$1.59\cdot10^{-14}$

Table 15.6 Bimolecular reaction rate constants in cm^3 s^{-1} for the D-transfer for the Eley–Rideal mechanism calculated using the implicit surface model. For $T \leq 200$ K, instanton theory and for $T \geq 300$ K, the Eckart approximation was used.

T[K]	HDOH	HDOD	DDOH	DDOD
80			$3.28{\cdot}10^{-22}$	$1.09{\cdot}10^{-21}$
90	$8.40{\cdot}10^{-22}$	$2.50{\cdot}10^{-21}$	$5.26{\cdot}10^{-22}$	$1.65{\cdot}10^{-21}$
100	$1.37{\cdot}10^{-21}$	$3.90{\cdot}10^{-21}$	$8.93{\cdot}10^{-22}$	$2.65{\cdot}10^{-21}$
110	$2.33{\cdot}10^{-21}$	$6.32{\cdot}10^{-21}$	$1.58{\cdot}10^{-21}$	$4.48{\cdot}10^{-21}$
120	$4.08{\cdot}10^{-21}$	$1.07{\cdot}10^{-20}$	$2.90{\cdot}10^{-21}$	$7.89{\cdot}10^{-21}$
130	$7.34{\cdot}10^{-21}$	$1.86{\cdot}10^{-20}$	$5.45{\cdot}10^{-21}$	$1.44{\cdot}10^{-20}$
140	$1.35{\cdot}10^{-20}$	$3.34{\cdot}10^{-20}$	$1.05{\cdot}10^{-20}$	$2.69{\cdot}10^{-20}$
150	$2.55{\cdot}10^{-20}$	$6.12{\cdot}10^{-20}$	$2.06{\cdot}10^{-20}$	$5.13{\cdot}10^{-20}$
165	$6.78{\cdot}10^{-20}$	$1.58{\cdot}10^{-19}$	$5.82{\cdot}10^{-20}$	$1.40{\cdot}10^{-19}$
180	$1.86{\cdot}10^{-19}$	$4.20{\cdot}10^{-19}$	$1.68{\cdot}10^{-19}$	$3.90{\cdot}10^{-19}$
200	$7.41{\cdot}10^{-19}$	$1.62{\cdot}10^{-18}$	$6.99{\cdot}10^{-19}$	$1.57{\cdot}10^{-18}$
300	$1.93{\cdot}10^{-17}$	$3.38{\cdot}10^{-17}$	$1.85{\cdot}10^{-17}$	$3.30{\cdot}10^{-17}$
333	$4.21{\cdot}10^{-17}$	$7.07{\cdot}10^{-17}$	$4.08{\cdot}10^{-17}$	$6.98{\cdot}10^{-17}$
375	$9.43{\cdot}10^{-17}$	$1.52{\cdot}10^{-16}$	$9.26{\cdot}10^{-17}$	$1.52{\cdot}10^{-16}$
429	$2.17{\cdot}10^{-16}$	$3.36{\cdot}10^{-16}$	$2.16{\cdot}10^{-16}$	$3.40{\cdot}10^{-16}$
500	$5.14{\cdot}10^{-16}$	$7.68{\cdot}10^{-16}$	$5.21{\cdot}10^{-16}$	$7.90{\cdot}10^{-16}$
600	$1.27{\cdot}10^{-15}$	$1.83{\cdot}10^{-15}$	$1.31{\cdot}10^{-15}$	$1.93{\cdot}10^{-15}$
750	$3.33{\cdot}10^{-15}$	$4.67{\cdot}10^{-15}$	$3.54{\cdot}10^{-15}$	$5.05{\cdot}10^{-15}$
1000	$9.66{\cdot}10^{-15}$	$1.32{\cdot}10^{-14}$	$1.07{\cdot}10^{-14}$	$1.48{\cdot}10^{-14}$

Table 15.7 Unimolecular reaction rate constants in s^{-1} for the H-transfer for the Langmuir–Hinshelwood mechanism calculated using the implicit surface model. For $T \leq 250$ K, instanton theory and for $T \geq 300$ K, the Eckart approximation was used.

T[K]	HHOH	HHOD	DHOH	DHOD
60	$5.12{\cdot}10^{5}$	$3.42{\cdot}10^{5}$	$1.59{\cdot}10^{5}$	$1.09{\cdot}10^{5}$
65	$5.16{\cdot}10^{5}$	$3.66{\cdot}10^{5}$	$1.67{\cdot}10^{5}$	$1.24{\cdot}10^{5}$
70	$5.34{\cdot}10^{5}$	$4.02{\cdot}10^{5}$	$1.80{\cdot}10^{5}$	$1.40{\cdot}10^{5}$
75	$5.67{\cdot}10^{5}$	$4.43{\cdot}10^{5}$	$1.99{\cdot}10^{5}$	$1.61{\cdot}10^{5}$
80	$6.12{\cdot}10^{5}$	$4.95{\cdot}10^{5}$	$2.23{\cdot}10^{5}$	$1.88{\cdot}10^{5}$
90	$7.41{\cdot}10^{5}$	$6.32{\cdot}10^{5}$	$2.92{\cdot}10^{5}$	$2.58{\cdot}10^{5}$
100	$9.35{\cdot}10^{5}$	$8.24{\cdot}10^{5}$	$3.96{\cdot}10^{5}$	$3.61{\cdot}10^{5}$
110	$1.22{\cdot}10^{6}$	$1.10{\cdot}10^{6}$	$5.50{\cdot}10^{5}$	$5.12{\cdot}10^{5}$
120	$1.63{\cdot}10^{6}$	$1.50{\cdot}10^{6}$	$7.82{\cdot}10^{5}$	$7.37{\cdot}10^{5}$
130	$2.23{\cdot}10^{6}$	$2.06{\cdot}10^{6}$	$1.13{\cdot}10^{6}$	$1.07{\cdot}10^{6}$
140	$3.08{\cdot}10^{6}$	$2.87{\cdot}10^{6}$	$1.66{\cdot}10^{6}$	$1.58{\cdot}10^{6}$
150	$4.32{\cdot}10^{6}$	$4.03{\cdot}10^{6}$	$2.45{\cdot}10^{6}$	$2.34{\cdot}10^{6}$
165	$7.30{\cdot}10^{6}$	$6.82{\cdot}10^{6}$	$4.48{\cdot}10^{6}$	$4.28{\cdot}10^{6}$
180	$1.25{\cdot}10^{7}$	$1.17{\cdot}10^{7}$	$8.28{\cdot}10^{6}$	$7.89{\cdot}10^{6}$
200	$2.63{\cdot}10^{7}$	$2.44{\cdot}10^{7}$	$1.90{\cdot}10^{7}$	$1.80{\cdot}10^{7}$
225	$6.77{\cdot}10^{7}$	$6.24{\cdot}10^{7}$	$5.38{\cdot}10^{7}$	$5.05{\cdot}10^{7}$
250	$1.78{\cdot}10^{8}$	$1.62{\cdot}10^{8}$	$1.53{\cdot}10^{8}$	$1.42{\cdot}10^{8}$
300	$5.19{\cdot}10^{8}$	$4.56{\cdot}10^{8}$	$4.37{\cdot}10^{8}$	$3.88{\cdot}10^{8}$
333	$9.12{\cdot}10^{8}$	$7.76{\cdot}10^{8}$	$7.73{\cdot}10^{8}$	$6.64{\cdot}10^{8}$
375	$1.64{\cdot}10^{9}$	$1.35{\cdot}10^{9}$	$1.39{\cdot}10^{9}$	$1.16{\cdot}10^{9}$
429	$2.98{\cdot}10^{9}$	$2.39{\cdot}10^{9}$	$2.56{\cdot}10^{9}$	$2.06{\cdot}10^{9}$
500	$5.52{\cdot}10^{9}$	$4.28{\cdot}10^{9}$	$4.75{\cdot}10^{9}$	$3.72{\cdot}10^{9}$
600	$1.03{\cdot}10^{10}$	$7.78{\cdot}10^{9}$	$8.93{\cdot}10^{9}$	$6.80{\cdot}10^{9}$
750	$1.94{\cdot}10^{10}$	$1.43{\cdot}10^{10}$	$1.70{\cdot}10^{10}$	$1.27{\cdot}10^{10}$
1000	$3.71{\cdot}10^{10}$	$2.68{\cdot}10^{10}$	$3.32{\cdot}10^{10}$	$2.42{\cdot}10^{10}$

Table 15.8 Unimolecular reaction rate constants in s^{-1} for the D-transfer for the Langmuir–Hinshelwood mechanism calculated using the implicit surface model. For $T \leq 200$ K, instanton theory and for $T \geq 300$ K, the Eckart approximation was used.

T[K]	HDOH	HDOD	DDOH	DDOD
60	$1.41{\cdot}10^{3}$	$1.15{\cdot}10^{3}$	$3.99{\cdot}10^{2}$	$3.39{\cdot}10^{2}$
65	$1.63{\cdot}10^{3}$	$1.41{\cdot}10^{3}$	$4.85{\cdot}10^{2}$	$4.36{\cdot}10^{2}$
70	$1.93{\cdot}10^{3}$	$1.74{\cdot}10^{3}$	$6.04{\cdot}10^{2}$	$5.67{\cdot}10^{2}$
75	$2.34{\cdot}10^{3}$	$2.19{\cdot}10^{3}$	$7.68{\cdot}10^{2}$	$7.46{\cdot}10^{2}$
80	$2.89{\cdot}10^{3}$	$2.79{\cdot}10^{3}$	$9.97{\cdot}10^{2}$	$9.96{\cdot}10^{2}$
90	$4.63{\cdot}10^{3}$	$4.65{\cdot}10^{3}$	$1.75{\cdot}10^{3}$	$1.82{\cdot}10^{3}$
100	$7.79{\cdot}10^{3}$	$8.03{\cdot}10^{3}$	$3.21{\cdot}10^{3}$	$3.41{\cdot}10^{3}$
110	$1.36{\cdot}10^{4}$	$1.43{\cdot}10^{4}$	$6.09{\cdot}10^{3}$	$6.57{\cdot}10^{3}$
120	$2.45{\cdot}10^{4}$	$2.60{\cdot}10^{4}$	$1.19{\cdot}10^{4}$	$1.29{\cdot}10^{4}$
130	$4.53{\cdot}10^{4}$	$4.82{\cdot}10^{4}$	$2.35{\cdot}10^{4}$	$2.56{\cdot}10^{4}$
140	$8.55{\cdot}10^{4}$	$9.11{\cdot}10^{4}$	$4.74{\cdot}10^{4}$	$5.17{\cdot}10^{4}$
150	$1.64{\cdot}10^{5}$	$1.74{\cdot}10^{5}$	$9.64{\cdot}10^{4}$	$1.05{\cdot}10^{5}$
165	$4.46{\cdot}10^{5}$	$4.73{\cdot}10^{5}$	$2.84{\cdot}10^{5}$	$3.08{\cdot}10^{5}$
180	$1.24{\cdot}10^{6}$	$1.31{\cdot}10^{6}$	$8.46{\cdot}10^{5}$	$9.08{\cdot}10^{5}$
200	$5.02{\cdot}10^{6}$	$5.24{\cdot}10^{6}$	$3.64{\cdot}10^{6}$	$3.86{\cdot}10^{6}$
300	$1.26{\cdot}10^{8}$	$1.12{\cdot}10^{8}$	$9.69{\cdot}10^{7}$	$8.69{\cdot}10^{7}$
333	$2.68{\cdot}10^{8}$	$2.30{\cdot}10^{8}$	$2.10{\cdot}10^{8}$	$1.81{\cdot}10^{8}$
375	$5.74{\cdot}10^{8}$	$4.76{\cdot}10^{8}$	$4.58{\cdot}10^{8}$	$3.82{\cdot}10^{8}$
429	$1.24{\cdot}10^{9}$	$9.94{\cdot}10^{8}$	$1.01{\cdot}10^{9}$	$8.13{\cdot}10^{8}$
500	$2.69{\cdot}10^{9}$	$2.09{\cdot}10^{9}$	$2.23{\cdot}10^{9}$	$1.75{\cdot}10^{9}$
600	$5.84{\cdot}10^{9}$	$4.41{\cdot}10^{9}$	$4.96{\cdot}10^{9}$	$3.78{\cdot}10^{9}$
750	$1.27{\cdot}10^{10}$	$9.37{\cdot}10^{9}$	$1.12{\cdot}10^{10}$	$8.27{\cdot}10^{9}$
1000	$2.80{\cdot}10^{10}$	$2.02{\cdot}10^{10}$	$2.55{\cdot}10^{10}$	$1.85{\cdot}10^{10}$

16 List of Figures

17 List of Tables

18 Bibliography

[1] Meisner, J.; Kästner, J. *Angew. Chem. Int. Ed.* **2016**, *55*, 5400–5413.

[2] Meisner, J.; Markmeyer, M. N.; Bohner, M. U.; Kästner, J. *Phys. Chem. Chem. Phys.* **2017**, *19*, 23085–23094.

[3] Born, M.; Oppenheimer, R. *Annalen der Physik* **1927**, *389*, 457–484.

[4] Fock, V. *Z. Phys.* **1932**, *75*, 622–647.

[5] Hund, F. *Z. Phys.* **1927**, *43*, 805–826.

[6] Gamow, G. *Z. Phys.* **1928**, *51*, 204.

[7] Gurney, R. W.; Condon, E. U. *Nature* **1928**, *122*, 439.

[8] Marcus, R. A.; Coltrin, M. E. *J. Chem. Phys.* **1977**, *67*, 2609.

[9] Pérez de Tudela, R.; Suleimanov, Y. V.; Richardson, J. O.; Rábanos, V. S.; Green, W. H.; Aoiz, F. J. *J. Phys. Chem. Lett.* **2014**, *5*, 4219–4224.

[10] Bell, R. P. *The tunnel effect in chemistry*, 1st ed.; Chapman and Hall (London), 1980.

[11] Kohen, A. *Prog. React. Kinet. Mech.* **2003**, *28*, 119–156.

[12] Miyazaki, T., Ed. *Atom Tunneling Phenomena in Physics, Chemistry and Biology*; Springer, Berlin, Germany, 2004.

[13] Kohen, A., Limbach, H.-H., Eds. *Isotope Effects in Chemistry and Biology*; CRC Press, Boca Raton, FL, USA, 2005.

[14] Allemann, R. K., Scrutton, N. S., Eds. *Quantum Tunnelling in Enzyme-Catalysed Reactions*; RSC Publishing, Cambridge, UK, 2009.

[15] Nagel, Z. D.; Klinman, J. P. *Chem. Rev.* **2006**, *106*, 3095–3118.

[16] Borden, W. T. *WIREs Comput. Mol. Sci.* **2016**, *6*, 20–46.

[17] Layfield, J. P.; Hammes-Schiffer, S. *Chem. Rev.* **2014**, *114*, 3466–3494.

[18] Johannissen, L. O.; Hay, S.; Scrutton, N. S. *Phys. Chem. Chem. Phys.* **2015**, *17*, 30775–30782.

[19] Vardi-Kilshtain, A.; Nitoker, N.; Major, D. T. *Arch. Biochem. Biophys.* **2015**, *582*, 18–27.

[20] Fernández-Ramos, A.; Miller, J. A.; Klippenstein, S. J.; Truhlar, D. G. *Chem. Rev.* **2006**, *106*, 4518–4584.

[21] Pu, J.; Gao, J.; Truhlar, D. G. *Chem. Rev.* **2006**, *106*, 3140–3169.

[22] Nyman, G. *Int. J. Quantum Chem.* **2014**, *114*, 1183–1198.

[23] Kästner, J. *WIREs Comput. Mol. Sci.* **2014**, *4*, 158–168.

[24] Homepage: Universität zu Köln, 1. Physikalisches Institut. http://www.astro.uni-koeln.de/cdms/molecules.

[25] van Dishoeck, E. F.; Herbst, E.; Neufeld, D. A. *Chem. Rev.* **2013**, *113*, 9043–9085.

[26] Herbst, E.; DeFrees, D. J.; Talbi, D.; Pauzat, F.; Koch, W.; McLean, A. D. *J. Chem. Phys.* **1991**, *94*, 7842.

[27] Shannon, R. J.; Blitz, M. A.; Goddard, A.; Heard, D. E. *Nat. Chem.* **2013**, *5*, 745–749.

[28] Tielens, A.; Hagen, W. *Astron. Astrophys.* **1982**, *114*, 245–260.

[29] Boogert, A. A.; Gerakines, P. A.; Whittet, D. C. *Annu. Rev. Astron. Astrophys.* **2015**, *53*, 541–581.

[30] Hiraoka, K.; Sato, T.; Sato, S.; Sogoshi, N.; Yokoyama, T.; Takashima, H.; Kitagawa, S. *Astrophys. J.* **2002**, *577*, 265.

[31] Hidaka, H.; Watanabe, M.; Kouchi, A.; Watanabe, N. *Astrophys. J.* **2009**, *702*, 291.

[32] Andersson, S.; Goumans, T. P. M.; Arnaldsson, A. *Chem. Phys. Lett.* **2011**, *513*, 31–36.

[33] Oehlers, C.; Wagner, H. G.; Ziemer, H.; Temps, F.; Dóbé, S. *J. Phys. Chem. A* **2000**, *104*, 10500–10510.

[34] Goumans, T. P. M. *Mon. Notices Royal Astron. Soc.* **2011**, *413*, 2615–2620.

[35] Parise, B.; Ceccarelli, C.; Tielens, A.; Herbst, E.; Lefloch, B.; Caux, E.; Castets, A.; Mukhopadhyay, I.; Pagani, L.; Loinard, L. *Astron. Astrophys.* **2002**, *L49*, 393.

[36] Parise, B.; Castets, A.; Herbst, E.; Caux, E.; Ceccarelli, C.; Mukhopadhyay, I.; Tielens, A. *Astron. Astrophys.* **2004**, *416*, 159.

[37] Caselli, P.; Ceccarelli, C. *Astron. Astrophys. Rev.* **2012**, *20*.

[38] Goumans, T. P. M.; Kästner, J. *J. Phys. Chem. A* **2011**, *115*, 10767.

[39] Cheung, A. C.; Rank, D. M.; Townes, C. H.; Thornton, D. D.; Welch, W. J. *Nature* **1969**, *221*, 626.

[40] van Dishoeck, E. F. *Ann. Rev. Astron. Astrophys.* **2004**, *42*, 119.

[41] Öberg, K. I.; Boogert, A. C. A.; Pontoppidan, K. M.; van den Broek, S.; van Dishoeck, E. F.; Bottinelli, S.; Blake, G. A.; Evans, N. J., II *Astrophys. J.* **2011**, *740*, 109.

[42] Hiraoka, K.; Miyagoshi, T.; Takayama, T.; Yamamoto, K.; Kihara, Y. *Astrophys. J.* **1998**, *498*, 710.

[43] Miyauchi, N.; Hidaka, H.; Chigai, T.; Nagaoka, A.; Watanabe, N.; Kouchi, A. *Chem. Phys. Lett.* **2008**, *456*, 27–30.

[44] Oba, Y.; Miyauchi, N.; Hidaka, H.; Chigai, T.; Watanabe, N.; Kouchi, A. *Astrophys. J.* **2009**, *701*, 464.

[45] Ioppolo, S.; Cuppen, H. M.; Romanzin, C.; van Dishoeck, E. F.; Linnartz, H. *Astrophys. J.* **2008**, *686*, 1474.

[46] Ioppolo, S.; Cuppen, H. M.; Romanzin, C.; van Dishoeck, E. F.; Linnartz, H. *Phys. Chem. Chem. Phys.* **2010**, *12*, 12065–12076.

[47] Cuppen, H. M.; Ioppolo, S.; Romanzin, C.; Linnartz, H. *Phys. Chem. Chem. Phys.* **2010**, *12*, 12077–12088.

[48] Romanzin, C.; Ioppolo, S.; Cuppen, H. M.; van Dishoeck, E. F.; Linnartz, H. *J. Chem. Phys.* **2011**, *134*, 084504.

[49] Oba, Y.; Osaka, K.; Watanabe, N.; Chigai, T.; Kouchi, A. *Faraday Discuss.* **2014**, *168*, 185–204.

[50] Lamberts, T.,; Cuppen, H. M.,; Fedoseev, G.,; Ioppolo, S.,; Chuang, K.-J.,; Linnartz, H., *Astron. Astrophys.* **2014**, *570*, A57.

[51] Lamberts, T.; Fedoseev, G.; Puletti, F.; Ioppolo, S.; Cuppen, H. M.; Linnartz, H. *Mon. Notices Royal Astron. Soc.* **2016**, *455*, 634–641.

[52] Hama, T.; Kouchi, A.; Watanabe, N. *Science* **2016**, *351*, 65–67.

[53] Cuppen, H. M.; Herbst, E. *Astrophys. J.* **2007**, *668*, 294.

[54] Chang, Q.; Cuppen, H. M.; Herbst, E. *Astron. Astrophys.* **2007**, *469*, 973–983.

[55] Cazaux, S.; Cobut, V.; Marseille, M.; Spaans, M.; Caselli, P. *Astron. Astrophys.* **2010**, *522*, A74.

[56] Garrod, R. T. *Astrophys. J.* **2013**, *765*, 60.

[57] Vasyunin, A. I.; Herbst, E. *Astrophys. J.* **2013**, *762*, 86.

[58] Lamberts, T.; de Vries, X.; Cuppen, H. M. *Faraday Discuss.* **2014**, *168*, 327–347.

[59] Furuya, K.; Aikawa, Y.; Nomura, H.; Hersant, F.; Wakelam, V. *Astrophys. J.* **2013**, *779*, 11.

[60] Taquet, V.,; Peters, P. S.,; Kahane, C.,; Ceccarelli, C.,; López-Sepulcre, A.,; Toubin, C.,; Duflot, D.,; Wiesenfeld, L., *Astron. Astrophys.* **2013**, *550*, A127.

[61] Furuya, K.,; Drozdovskaya, M. N.,; Visser, R.,; van Dishoeck, E. F.,; Walsh, C.,; Harsono, D.,; Hincelin, U.,; Taquet, V., *Astron. Astrophys.* **2017**, *599*, A40.

[62] Bukas, V. J.; Mitra, S.; Meyer, J.; Reuter, K. *J. Chem. Phys.* **2015**, *143*, 034705.

[63] Dulieu, F.; Amiaud, L.; Congiu, E.; Fillion, J.-H.; Matar, E.; Momeni, A.; Pirronello, V.; Lemaire, J. L. *Astron. Astrophys.* **2010**, *512*, A30.

[64] Jing, D.; He, J.; Brucato, J.; Sio, A. D.; Tozzetti, L.; Vidali, G. *Astrophys. J. Lett.* **2011**, *741*, L9.

[65] Oba, Y.; Watanabe, N.; Hama, T.; Kuwahata, K.; Hidaka, H.; Kouchi, A. *Astrophys. J.* **2012**, *749*, 67.

[66] Keyser, L. F. *J. Phys. Chem.* **1986**, *90*, 2994–3003.

[67] Mousavipour, S. H.; Fernández-Ramos, A.; Meana-Pañeda, R.; Martínez-Núñez, E.; Vázquez, S. A.; Ríos, M. A. *J. Phys. Chem. A* **2007**, *111*, 719–725.

[68] Lamberts, T.; Samanta, P. K.; Köhn, A.; Kästner, J. *Phys. Chem. Chem. Phys.* **2016**, *18*, 33021–33030.

[69] Talukdar, R. K.; Gierczak, T.; Goldfarb, L.; Rudich, Y.; Rao, B. S. M.; Ravishankara, A. R. *J. Phys. Chem.* **1996**, *100*, 3037–3043.

[70] Atkinson, R.; Baulch, D. L.; Cox, R. A.; Crowley, J. N.; Hampson, R. F.; Hynes, R. G.; Jenkin, M. E.; Rossi, M. J.; Troe, J. *Atmos. Chem. Phys.* **2004**, *4*, 1461–1738.

[71] Nguyen, T. L.; Stanton, J. F.; Barker, J. R. *J. Phys. Chem. A* **2011**, *115*, 5118–5126.

[72] Meisner, J.; Kästner, J. *J. Chem. Phys.* **2016**, *144*, 174303.

[73] Hama, T.; Watanabe, N. *Chem. Rev.* **2013**, *113*, 8783–8839.

[74] Hratchian, H. P.; Schlegel, H. B. *J.Chem. Phys.* **2004**, *120*, 9918.

[75] Kästner, J.; Carr, J. M.; Keal, T. W.; Thiel, W.; Wander, A.; Sherwood, P. *J. Phys. Chem. A* **2009**, *113*, 11856.

[76] Meisner, J.; Lamberts, T.; Kästner, J. *ACS Earth Space Chem.* **2017**, *1*, 399–410.

[77] Knowles, P.; Schütz, M.; Werner, H.-J. In *Winterschool, 21 – 25 February 2000, Proceedings, Second Edition*; Grotendorst, J., Ed.; Forschungszentrum Julich, Germany, 2000; pp 97–180.

[78] Shiozaki, T.; Werner, H.-J. *Mol. Phys.* **2013**, *111*, 607–630.

[79] Goerigk, L.; Grimme, S. *WIREs Comput. Mol. Sci.* **2014**, *4*, 576–600.

[80] Duster, A. W.; Wang, C.-H.; Garza, C. M.; Miller, D. E.; Lin, H. *WIREs Comput. Mol. Sci.* **2017**, *7*, ASAP.

[81] Fukui, K. *Acc. Chem. Res.* **1981**, *14*, 363–368.

[82] Ishida, K.; Morokuma, K.; Komornicki, A. *J. Chem. Phys.* **1977**, *66*, 2153–2156.

[83] Page, M.; McIver, J. W. *J. Chem. Phys.* **1988**, *88*, 922–935.

[84] Page, M.; Doubleday, C.; McIver, J. W. *J. Chem. Phys.* **1990**, *93*, 5634–5642.

[85] Gonzalez, C.; Schlegel, H. B. *J. Chem. Phys.* **1989**, *90*, 2154.

[86] Gonzalez, C.; Schlegel, H. B. *J. Phys. Chem.* **1990**, *94*, 5523.

[87] Hratchian, H. P.; Schlegel, H. B. *J. Phys. Chem. A* **2002**, *106*, 165–169.

[88] Jónsson, H.; Mills, G.; Jacobsen, K. W. *Classical and Quantum Dynamics in Condensed Phase Simulations*; World Scientific, 1998; Chapter Nudged Elastic Band Method for Finding Minimum Energy Paths of Transitions, p 385.

[89] Henkelman, G.; Jónsson, H. *J. Chem. Phys.* **2000**, *113*, 9978.

[90] Henkelman, G.; Uberuaga, B. P.; Jónsson, H. *J. Chem. Phys.* **2000**, *113*, 9901.

[91] E, W.; Ren, W.; Vanden-Eijnden, E. *Phys. Rev. B* **2002**, *66*, 052301.

[92] Peters, B.; Heyden, A.; Bell, A. T.; Chakraborty, A. *J. Chem. Phys.* **2004**, *120*, 7877.

[93] Maeda, S.; Harabuchi, Y.; Ono, Y.; Taketsugu, T.; Morokuma, K. *Int. J. Quantum Chem.* **2015**, *115*, 258–269.

[94] Press, W. *NumericalRecipes in Pascal: The Art of Scientific Computing*; Cambridge University Press, 1989.

[95] Hratchian, H. P.; Frisch, M. J.; Schlegel, H. B. *J. Chem. Phys.* **2010**, *133*, 224101.

[96] Hratchian, H. P.; Frisch, M. J. *J. Chem. Phys.* **2011**, *134*, 204103.

[97] Hratchian, H. P.; Schlegel, H. B. *J. Chem. Theory Comput.* **2005**, *1*, 61–69.

[98] Bulirsch, R.; Stoer, J. *Numer. Math.* **1964**, *6*, 413–427.

[99] Bulirsch, R.; Stoer, J. *Numer. Math.* **1966**, *8*, 93–104.

[100] Bulirsch, R.; Stoer, J. *Numer. Math.* **1966**, *8*, 1–13.

[101] Hratchian, H. P.; Kraka, E. *J. Chem. Theory Comput.* **2013**, *9*, 1481–1488.

[102] McElroy, D.,; Walsh, C.,; Markwick, A. J.,; Cordiner, M. A.,; Smith, K.,; Millar, T. J., *Astron. Astrophys.* **2013**, *550*, A36.

[103] Wakelam, V. et al. *Astrophys. J. Supplement Series* **2012**, *199*, 21.

[104] Haworth, T. J.; Ilee, J. D.; Forgan, D. H.; Facchini, S.; Price, D. J.; Boneberg, D. M.; Booth, R. A.; Clarke, C. J.; Gonzalez, J.-F.; Hutchison, M. A.; et al., *Publ. Astron. Soc. Aust.* **2016**, *33*.

[105] Semenov, D.,; Hersant, F.,; Wakelam, V.,; Dutrey, A.,; Chapillon, E.,; Guilloteau, St.,; Henning, Th.,; Launhardt, R.,; Piétu, V.,; Schreyer, K., *Astron. Astrophys.* **2010**, *522*, A42.

[106] D.Sc., J. J. H. *Philos. Mag.* **1885**, *20*, 323–328.

[107] Arrhenius, S. *Z. Phys. Chem. (Leipzig)* **1889**, *4*, 226.

[108] Zuev, P. S.; Sheridan, R. S.; Albu, T. V.; Truhlar, D. G.; Hrovat, D. A.; Borden, W. T. *Science* **2003**, *299*, 867–870.

[109] Goldanskii, V. I.; Frank-Kamenetskii, M. D.; Barkalov, I. M. *Science* **1973**, *182*, 1344–1345.

[110] Kooij, D. M., *Z. Phys. Chem.* **1893**, *1*, 155–161.

[111] Truhlar, D. G. *J. Chem. Educ.* **1978**, *55*, 309.

[112] Zheng, J.; Truhlar, D. G. *Phys. Chem. Chem. Phys.* **2010**, *12*, 7782–7793.

[113] Zheng, J.; Truhlar, D. G. *Faraday Discuss.* **2012**, *157*, 59–88.

[114] Zheng, J.; Seal, P.; Truhlar, D. G. *Chem. Sci.* **2013**, *4*, 200–212.

[115] Steinfeld, J. I.; Francisco, J. S.; Hase, W. L. *Chemical kinetics and dynamics*; Upper Saddle River, N.J: Prentice Hall, 1999.

[116] Groß, A. *Phys. Rev. Lett.* **2009**, *103*, 246101.

[117] Meyer, J.; Reuter, K. *Angew. Chem., Int. Ed.* **2014**, *53*, 4721–4724.

[118] Tielens, A. G. G. M. *The Physics and Chemistry of the Interstellar Medium, by A. G. G. M. Tielens, pp. . ISBN 0521826349. Cambridge, UK: Cambridge University Press, 2005.*; Cambridge University Press, 2005.

[119] Cuppen, H. M.; Walsh, C.; Lamberts, T.; Semenov, D.; Garrod, R. T.; Penteado, E. M.; Ioppolo, S. *Space Sci. Rev.* **2017**, 1–58.

[120] Rideal, E. K. *Math. Proc. Cambridge Philos. Soc.* **1939**, *35*, 130–132.

[121] Eley, D. *The Catalytic Activation of Hydrogen*; Advances in Catalysis; Academic Press, 1948; Vol. 1 Supplement C; pp 157 – 199.

[122] Langmuir, I. *Trans. Faraday Soc.* **1922**, *17*, 607–620.

[123] Hutchison, W. K.; Hinshelwood, C. N. *J. Chem. Soc.* **1926**, *129*, 1556–1559.

[124] Rice, O. K.; Ramsperger, H. C. *J. Am. Chem. Soc.* **1927**, *49*, 1617–1629.

[125] Kassel, L. S. *J. Phys. Chem.* **1928**, *32*, 225–242.

[126] Marcus, R. A. *J. Chem. Phys.* **1952**, *20*, 359–364.

[127] Miller, W. H. *J. Chem. Phys.* **1975**, *62*, 1899–1906.

[128] Richardson, J. O.; Pérez, C.; Lobsiger, S.; Reid, A. A.; Temelso, B.; Shields, G. C.; Kisiel, Z.; Wales, D. J.; Pate, B. H.; Althorpe, S. C. *Science* **2016**, *351*, 1310–1313.

[129] McConnell, S. R.; Löhle, A.; Kästner, J. *J. Chem. Phys.* **2017**, *146*, 074105.

[130] Eyring, H. *J. Chem. Phys.* **1935**, *3*, 107–115.

[131] Evans, M. G.; Polanyi, M. *Trans. Faraday Soc.* **1935**, *31*, 875.

[132] Lorquet, J. C.; Leyh-Nihant, B. *J. Phys. Chem.* **1988**, *92*, 4778–4783.

[133] Harvey, J. N. *Phys. Chem. Chem. Phys.* **2007**, *9*, 331–343.

[134] Lykhin, A. O.; Kaliakin, D. S.; dePolo, G. E.; Kuzubov, A. A.; Varganov, S. A. *Int. J. Quantum Chem.* **2016**, *116*, 750–761.

[135] Truhlar, D. G.; Garrett, B. C. *Ann. Rev. Phys. Chem.* **1984**, *35*, 159.

[136] Fernandez-Ramos, A.; Ellingson, B. A.; Garrett, B. C.; Truhlar, D. G. *Reviews in Computational Chemistry*; John Wiley & Sons, Inc., 2007; pp 125–232.

[137] Hänggi, P.; Talkner, P.; Borkovec, M. *Rev. Mod. Phys.* **1990**, *62*, 251.

[138] Truhlar, D. G.; Garrett, B. C.; Klippenstein, S. J. *J. Phys. Chem.* **1996**, *100*, 12771–12800.

[139] Pollak, E.; Talkner, P. *Chaos* **2005**, *15*, 026116.

[140] Demtröder, W. *Experimentalphysik 3*; Springer-Lehrbuch; Springer Berlin Heidelberg: Berlin, Heidelberg, 2010; pp Online–Ressource (XXII, 650S. 706 Abb.. Mit 9 Farbtafeln, online resource).

[141] Bowman, J. M. *J. Phys. Chem.* **1991**, *95*, 4960–4968.

[142] Bunker, P. R. *Molecular Symmetry and Spectroscopy*; PB - NRC Research Press, 1979.

[143] Fernández-Ramos, A.; Ellingson, B. A.; Meana-Pañeda, R.; Marques, J. M. C.; Truhlar, D. G. *Theor. Chem. Acc.* **2007**, *118*, 813–826.

[144] Dennison, D. M. *Proc. R. Soc. A* **1927**, *115*, 483–486.

[145] Isaacson, A. D. *J. Chem. Phys.* **2002**, *117*, 8778–8786.

[146] Hao, Y.; Pan, X.; Song, L.; Ding, Y.; Xia, W.; Wang, S.; Yu, H.; Kang, L.; Yao, L. *Canadian Journal of Chemistry* **2017**, *95*, 1064–1072.

[147] Garraway, B. M.; Suominen, K.-A. *Rep. Prog. Phys.* **1995**, *58*, 365.

[148] Manthe, U.; Meyer, H.-D.; Cederbaum, L. S. *J. Chem. Phys.* **1992**, *97*, 3199–3213.

[149] Meyer, H.-D.; Manthe, U.; Cederbaum, L. S. *Chem. Phys. Lett.* **1990**, *165*, 73 – 78.

[150] Padmanaban, R.; Nest, M. *Chem. Phys. Lett.* **2008**, *463*, 263–266.

[151] Hammer, T.; Coutinho-Neto, M. D.; Viel, A.; Manthe, U. *J. Chem. Phys.* **2009**, *131*, 224109.

[152] Hansen, N. F.; Andersen, H. C. *J. Phys. Chem.* **1996**, *199*, 1137–1143.

[153] Cheney, B. G.; Andersen, H. C. *J. Chem. Phys.* **2003**, *118*, 9542–9551.

[154] Bell, R. P. *Proc. Royal Soc. A* **1935**, *148*, 241–250.

[155] Eckart, C. *Phys. Rev.* **1930**, *35*, 1303–1309.

[156] Truhlar, D. G.; Kuppermann, A. *J. Am. Chem. Soc.* **1971**, *93*, 1840.

[157] Miller, W. H.; Handy, N. C.; Adams, J. E. *J. Chem. Phys.* **1980**, *72*, 99.

[158] Truhlar, D. G.; Garrett, B. C. *J. Phys. Chem. A* **2003**, *107*, 4006–4007.

[159] Skodje, R. T.; Truhlar, D. G.; Garrett, B. C. *J. Phys. Chem.* **1981**, *85*, 3019–3023.

[160] Garrett, B. C.; Truhlar, D. G.; Wagner, A. F.; Dunning Jr., T. H. *J. Chem. Phys.* **1983**, *78*, 4400.

[161] Garrett, B. C.; Abusalbi, N.; Kouri, D. J.; Truhlar, D. G. *J. Chem. Phys.* **1985**, *83*, 2252.

[162] Liu, Y. P.; Lu, D. H.; Gonzalez-Lafont, A.; Truhlar, D. G.; Garrett, B. C. *J. Am. Chem. Soc.* **1993**, *115*, 7806–7817.

[163] Truhlar, D. G. *J. Chem. Soc., Faraday Trans.* **1994**, *90*, 1740.

[164] Langer, J. S. *Ann. Phys. (N.Y.)* **1967**, *41*, 108–157.

[165] Coleman, S. *Phys. Rev. D* **1977**, *15*, 2929–2936.

[166] Callan Jr., C. G.; Coleman, S. *Phys. Rev. D* **1977**, *16*, 1762–1768.

[167] Gildener, E.; Patrascioiu, A. *Phys. Rev. D* **1977**, *16*, 423–430.

[168] Mills, G.; G. K. Schenter, D. M.; Jónsson, H. *Classical and Quantum Dynamics in Condensed Phase Simulations*; World Scientific, 1998; Chapter RAW Quantum Transition State Theory, p 405.

[169] Arnaldsson, A. Calculation of quantum mechanical rate constants directly from ab initio atomic forces. Ph.D. thesis, University of Washington, 2007.

[170] Andersson, S.; Nyman, G.; Arnaldsson, A.; Manthe, U.; Jónsson, H. *J. Phys. Chem. A* **2009**, *113*, 4468–4478.

[171] Mills, G.; Jónsson, H. *Phys. Rev. Lett.* **1994**, *72*, 1124–1127.

[172] Mills, G.; Schenter, G. K.; Makarov, D. E.; Jónsson, H. *Chem. Phys. Lett.* **1997**, *278*, 91–96.

[173] Goumans, T. P. M.; Kästner, J. *Angew. Chem. Int. Ed.* **2010**, *49*, 7350–7352.

[174] Jónsson, H. *Proc. Nat. Acad. Sci. U.S.A.* **2010**, *108*, 944–949.

[175] Goumans, T. P. M. *Mon. Notices Royal Astron. Soc.* **2011**, *415*, 3129–3134.

[176] Meisner, J.; Rommel, J. B.; Kästner, J. *J. Comput. Chem.* **2011**, *32*, 3456–3463.

[177] Álvarez-Barcia, S.; Flores, J. R.; Kästner, J. *J. Phys. Chem. A* **2014**, *118*, 78–82.

[178] Kryvohuz, M. *J. Phys. Chem. A* **2014**, *118*, 535–544.

[179] Beyer, A. N.; Richardson, J. O.; Knowles, P. J.; Rommel, J.; Althorpe, S. C. *J. Phys. Chem. Lett.* **2016**, *7*, 4374–4379.

[180] Song, L.; Kästner, J. *Phys. Chem. Chem. Phys.* **2016**, *18*, 29278–29285.

[181] Lamberts, T.; Fedoseev, G.; Kästner, J.; Ioppolo, S.; Linnartz, H. *Astron. Astrophys.* **2017**, *599*, A132.

[182] Lamberts, T.; Kästner, J. *Astrophys. J.* **2017**, *846*, 43.

[183] Affleck, I. *Phys. Rev. Lett.* **1981**, *46*, 388–391.

[184] Benderskii, V. A.; Makarov, D. E.; Wight, C. A. *Adv. Chem. Phys.* **1994**, *88*, 55.

[185] Richardson, J. O. Ring-Polymer Approaches to Instanton Theory. Ph.D. thesis, Pembroke College, University of Cambridge, 2012.

[186] Kästner, J. Habilitationsschrift: Tunneling Rates via Instanton Theory and Free-Energy Barriers using Umbrella Integration in QM/MM Simulations. Ph.D. thesis, University of Stuttgart, 2013.

[187] Feynman, R. P. *Rev. Mod. Phys.* **1948**, *20*, 367.

[188] Miller, W. H. *J. Chem. Phys.* **1971**, *55*, 3146–3149.

[189] Rommel, J. B.; Goumans, T. P. M.; Kästner, J. *J. Chem. Theory Comput.* **2011**, *7*, 690–698.

[190] Rommel, J. B.; Kästner, J. *J. Chem. Phys.* **2011**, *134*, 184107.

[191] Gillan, M. J. *J. Phys. C* **1987**, *20*, 3621.

[192] Coleman, S. *Nucl. Phys. B* **1988**, *298*, 178–186.

[193] Rommel, J. B. Improvements to the instanton method : tunneling rates in the enzyme glutamate mutase. Ph.D. thesis, University of Stuttgart, 2012.

[194] Pople, J. A.; Schlegel, H. B.; Krishnan, R.; Defrees, D. J.; Binkley, J. S.; Frisch, M. J.; Whiteside, R. A.; Hout, R. F.; Hehre, W. J. *Int. J. Quantum Chem.* **1981**, *20*, 269–278.

[195] Pflüger, K.; Paulus, M.; Jagiella, S.; Burkert, T.; Rauhut, G. *Theor. Chem. Acc.* **2005**, *114*, 327–332.

[196] Corchado, J. C.; Espinosa-García, J.; Roberto-Neto, O.; Chuang, Y.-Y.; Truhlar, D. G. *J. Phys. Chem. A* **1998**, *102*, 4899–4910.

[197] Sekušak, S.; Cory, M. G.; Bartlett, R. J.; Sabljić, A. *J. Phys. Chem. A* **1999**, *103*, 11394–11405.

[198] Huang, C.-H.; Tsai, L.-C.; Hu, W.-P. *J. Phys. Chem. A* **2001**, *105*, 9945–9953.

[199] Siebrand, W.; Smedarchina, Z.; Zgierski, M. Z.; Fernandez-RAMOS, A. *Int. Rev. Phys. Chem.* **1999**, *18*, 5–41.

[200] Smedarchina, Z.; Fernandez-Ramos, A.; Rios, M. A. *J. Chem. Phys.* **1997**, *106*, 3956–3964.

[201] Tautermann, C. S.; Voegele, A. F.; Loerting, T.; Liedl, K. R. *J. Chem. Phys.* **2002**, *117*, 1962–1966.

[202] Tautermann, C. S.; Voegele, A. F.; Loerting, T.; Liedl, K. R. *J. Chem. Phys.* **2002**, *117*, 1967–1974.

[203] Rommel, J. B.; Liu, Y.; Werner, H.-J.; Kästner, J. *J. Phys. Chem. B* **2012**, *116*, 13682–13689.

[204] Smedarchina, Z.; Siebrand, W.; Fernández-Ramos, A. *J. Chem. Phys.* **2012**, *137*, 224105.

[205] Sherwood, P. et al. *J. Mol. Struct. (THEOCHEM)* **2003**, *632*, 1–28.

[206] Metz, S.; Kästner, J.; Sokol, A. A.; Keal, T. W.; Sherwood, P. *WIREs Comput. Mol. Sci.* **2014**, *4*, 101–110.

[207] Adler, T. B.; Knizia, G.; Werner, H.-J. *J. Chem. Phys.* **2007**, *127*, 221106.

[208] Adler, T. B.; Werner, H.-J. *J. Chem. Phys.* **2009**, *130*, 241101.

[209] Werner, H.-J.; Knowles, P. J.; Knizia, G.; Manby, F. R.; Schütz, M. *WIREs Comput. Mol. Sci.* **2012**, *2*, 242–253.

[210] Peterson, K. A.; Adler, T. B.; Werner, H.-J. *J. Chem. Phys.* **2008**, *128*, 084102.

[211] TURBOMOLE V, a development of University of Karlsruhe and Forschungszentrum Karlsruhe GmbH, 1989-2007, TURBOMOLE GmbH, since 2007; available from `http://www.turbomole.com`.

[212] Eichkorn, K.; Weigend, F.; Treutler, O.; Ahlrichs, R. *Theor. Chem. Acc.* **1997**, *97*, 119–124.

[213] Anglada, J. M.; Bofill, J. M. *J. Comput. Chem.* **1997**, *18*, 992.

[214] Eckert, F.; Werner, H.-J. *Theor. Chem. Acc.* **1998**, *100*, 21–30.

[215] Halpern, A. M. *J. Chem. Educ.* **2006**, *83*, 69.

[216] Knizia, G.; Adler, T. B.; Werner, H.-J. *J. Chem. Phys.* **2009**, *130*, 054104.

[217] Dirac, P. *Proc. Royal Soc. (London) A* **1929**, *123*, 714–733.

[218] Slater, J. *Phys. Rev.* **1951**, *81*, 385–390.

[219] Vosko, S. H.; Wilk, L.; Nusair, M. *Can. J. Phys.* **1980**, *58*, 1200–1211.

[220] Becke, A. *Phys. Rev. A* **1988**, *38*, 3098–3100.

[221] Lee, C.; Yang, W.; Parr, R. G. *Phys. Rev. B* **1988**, *37*, 785–789.

[222] Becke, A. D. *J. Chem. Phys.* **1993**, *98*, 5648.

[223] Weigend, F.; Ahlrichs, R. *Phys. Chem. Chem. Phys.* **2005**, *7*, 3297–3305.

[224] Dormans, G. J. M.; Buck, H. M. *J. Am. Chem. Soc.* **1986**, *108*, 3253–3258.

[225] Liu, Y. P.; Lynch, G. C.; Truong, T. N.; Lu, D.; Truhlar, D. G.; Garrett, B. C. *J. Am. Chem. Soc.* **1993**, *115*, 2408–2415.

[226] Doering, W. v. E.; Zhao, X. *J. Am. Chem. Soc.* **2006**, *128*, 9080–9085.

[227] Doering, W. v. E.; Keliher, E. J. *J. Am. Chem. Soc.* **2007**, *129*, 2488–2495.

[228] Vaníček, J.; Miller, W. H. *J. Chem. Phys.* **2007**, *127*, 114309.

[229] Shelton, G. R.; Hrovat, D. A.; Borden, W. T. *J. Am. Chem. Soc.* **2007**, *129*, 164–168.

[230] Peles, D. N.; Thoburn, J. D. *J. Org. Chem.* **2008**, *73*, 3135–3144.

[231] Zimmermann, T.; Vaníček, J. *J. Mol. Model.* **2010**, *16*, 1779–1787.

[232] Kryvohuz, M.; Marcus, R. A. *J. Chem. Phys* **2012**, *137*, 134107.

[233] Perdew, J. P. *Phys. Rev. B* **1986**, *33*, 8822–8824.

[234] Becke, A. D. *J. Chem. Phys.* **1993**, *98*, 1372–1377.

[235] Hariharan, P. C.; Pople, J. A. *Theor. Chim. Acta* **1973**, *28*, 213–222.

[236] Rahn, T.; Eiler, J. M.; Boering, K. A.; Wennberg, P. O.; McCarthy, M. C.; Tyler, S.; Schauffler, S.; Donnelly, S.; Atlas, E. *Nature* **2003**, *424*, 918–921.

[237] Pieterse, G.; Krol, M. C.; Röckmann, T. *Atmos. Chem. Phys.* **2009**, *9*, 8503–8529.

[238] Gligorovski, S.; Strekowski, R.; Barbati, S.; Vione, D. *Chem. Rev.* **2015**, *115*, 13051–13092.

[239] Bhattacharya, S.; Panda, A. N.; Meyer, H.-D. *J. Chem. Phys.* **2010**, *132*, 214304.

[240] Bhattacharya, S.; Panda, A. N.; Meyer, H.-D. *J. Chem. Phys.* **2011**, *135*, 194302.

[241] Espinosa-Garcia, J.; Bonnet, L.; Corchado, J. C. *Phys. Chem. Chem. Phys.* **2010**, *12*, 3873–3877.

[242] Fu, B.; Kamarchik, E.; Bowman, J. M. *The Journal of Chemical Physics* **2010**, *133*, 164306.

[243] Fu, B.; Zhang, D. H. *The Journal of Chemical Physics* **2015**, *142*, 064314.

[244] Chan, J. M.; Bollinger, J. A.; Grewell, C. L.; Dooley, D. M. *J. Am. Chem. Soc.* **2004**, *126*, 3030.

[245] Manthe, U.; Matzkies, F. *J. Chem. Phys.* **2000**, *113*, 5725–5731.

[246] Ravishankara, A. R.; Nicovich, J. M.; Thompson, R. L.; Tully, F. P. *J. Phys. Chem.* **1981**, *85*, 2498–2503.

[247] Krasnoperov, L. N.; Michael, J. V. *J. Phys. Chem. A* **2004**, *108*, 5643–5648.

[248] Orkin, V. L.; Kozlov, S. N.; Poskrebyshev, G. A.; Kurylo, M. J. *J. Phys. Chem. A* **2006**, *110*, 6978–6985.

[249] Lam, K.-Y.; Davidson, D. F.; Hanson, R. K. *Int. J. Chem. Kinet.* **2013**, *45*, 363–373.

[250] Castillo, J. F. *ChemPhysChem* **2002**, *3*, 320–332.

[251] Smith, I. W. M.; Fleming Crim, F. *Phys. Chem. Chem. Phys.* **2002**, *4*, 3543–3551.

[252] Walch, S. P.; Dunning, T. H. *J. Chem. Phys.* **1980**, *72*, 1303–1311.

[253] Schatz, G. C.; Elgersma, H. *Chem. Phys. Lett.* **1980**, *73*, 21 – 25.

[254] Ochoa de Aspuru, G.; Clary, D. C. *J. Phys. Chem. A* **1998**, *102*, 9631–9637.

[255] Wu, G.-s.; Schatz, G. C.; Lendvay, G.; Fang, D.-C.; Harding, L. B. *J. Chem. Phys.* **2000**, *113*, 3150–3161.

[256] Bettens, R. P. A.; Collins, M. A.; Jordan, M. J. T.; Zhang, D. H. *J. Chem. Phys.* **2000**, *112*, 10162–10172.

[257] Yang, M.; Zhang, D. H.; Collins, M. A.; Lee, S. *J. Chem. Phys.* **2001**, *115*, 174.

[258] Chen, J.; Xu, X.; Xu, X.; Zhang, D. H. *J. Chem. Phys.* **2013**, *138*, 154301.

[259] Matzkies, F.; Manthe, U. *J. Chem. Phys.* **1998**, *108*, 4828–4836.

[260] Nguyen, T. L.; Stanton, J. F.; Barker, J. R. *Chem. Phys. Lett.* **2010**, *499*, 9–15.

[261] Garrett, B. C.; Truhlar, D. G.; Grev, R. S.; Magnuson, A. W. *J. Phys. Chem.* **1980**, *84*, 1730–1748.

[262] Truhlar, D.; Issacson, A.; Skodje, R.; Garrett, B. *J. Phys. Chem.* **1983**, *87*, 4554–4554.

[263] Fernandez-Ramos, A.; Truhlar, D. G. *J. Chem. Phys.* **2001**, *114*, 1491–1496.

[264] Wheeler, M. D.; Anderson, D. T.; Lester, M. I. *Int. Rev. Phys. Chem.* **2000**, *19*, 501–529.

[265] Miller, S.; Clary, D.; Kliesch, A.; Werner, H.-J. *Molecular Physics* **1994**, *83*, 405–428.

[266] Lu, D.; Truong, T. N.; Melissas, V. S.; Lynch, G. C.; Liu, Y.; Garrett, B. C.; Steckler, R.; Isaacson, A. D.; Rai, S. N.; Hancock, G. C.; Lauderdale, J. G.; Joseph, T.; Truhlar, D. G. *Comput. Phys. Commun.* **1992**, *71*, 235–262.

[267] Zheng, J. et al. POLYRATE-version 2010, University of Minnesota, Minneapolis, 2010. 2010.

[268] Brown, S. S.; Burkholder, J. B.; Talukdar, R. K.; Ravishankara, A. R. *J. Phys. Chem. A* **2001**, *105*, 1605–1614.

[269] Ree, J.; Kim, Y. H.; Shin, H. K. *J. Phys. Chem. A* **2015**, *119*, 3147–3160.

[270] Defazio, P.; Gray, S. K. *J. Phys. Chem. A* **2003**, *107*, 7132–7137.

[271] Pérez de Tudela, R.; Aoiz, F. J.; Suleimanov, Y. V.; Manolopoulos, D. E. *J. Phys. Chem. Lett.* **2012**, *3*, 493–497.

[272] Suleimanov, Y. V.; de Tudela, R. P.; Jambrina, P. G.; Castillo, J. F.; Sáez-Rábanos, V.; Manolopoulos, D. E.; Aoiz, F. J. *Phys. Chem. Chem. Phys.* **2013**, *15*, 3655–3665.

[273] Rappoport, D.; Furche, F. *J. Chem. Phys.* **2010**, *133*.

[274] Andersson, S.; Grüning, M. *J. Phys. Chem. A* **2004**, *108*, 7621–7636.

[275] Rimola, A.; Taquet, V.; Ugliengo, P.; Balucani, N.; Ceccarelli, C. *Astron. Astrophys.* **2014**, *572*, A70.

[276] Humphrey, W.; Dalke, A.; Schulten, K. *J. Mol. Graph.* **1996**, *14*, 33 – 38.

[277] Fletcher, N. H. *PhilosMagPartB* **1992**, *66*, 109–115.

[278] Jorgensen, W. L. *Acc. Chem. Res.* **1989**, *22*, 184.

[279] He, J.; Vidali, G. *Astrophys. J.* **2014**, *788*, 50.

[280] Dunning, T. H. *J. Chem. Phys.* **1989**, *90*, 1007–1023.

[281] Grimme, S. *J. Comput. Chem.* **2006**, *27*, 1787.

[282] Zhao, Y.; Truhlar, D. G. *Theor. Chem. Acc.* **2008**, *120*, 215–241.

[283] Perdew, J.; Wang, Y. *Phys. Rev. B* **1992**, *45*, 13244.

[284] Perdew, J. P.; Ernzerhof, M.; Burke, K. *J. Chem. Phys.* **1996**, *105*, 9982–9985.

[285] Grimme, S.; Brandenburg, J. G.; Bannwarth, C.; Hansen, A. *J. Chem. Phys.* **2015**, *143*, 054107.

[286] Tao, J.; Perdew, J. P.; Staroverov, V. N.; Scuseria, G. E. *Phys. Rev. Lett.* **2003**, *91*, 146401.

[287] Staroverov, V. N.; Scuseria, G. E.; Tao, J.; Perdew, J. P. *J. Chem. Phys.* **2003**, *119*, 12129–12137.

[288] Grimme, S.; Antony, J.; Ehrlich, S.; Krieg, H. *J. Chem. Phys.* **2010**, *132*, 154104.

Erklärung über die Eigenständigkeit der Dissertation

Ich versichere, dass ich die vorliegende Arbeit mit dem Titel *Theoretical Investigations of Atom Tunneling in the Interstellar Medium* selbständig verfasst und keine anderen als die angegebenen Quellen und Hilfsmittel benutzt habe; aus fremden Quellen entnommene Passagen und Gedanken sind als solche kenntlich gemacht.

Declaration of Authorship

I hereby certify that the dissertation entitled *Theoretical Investigations of Atom Tunneling in the Interstellar Medium* is entirely my own work except where otherwise indicated. Passages and ideas from other sources have been clearly indicated.

Name/Name: Jan Meisner

Unterschrift/Signed: ______________________

Datum/Date: April 26, 2018